

Resonance Effects in Laser Cluster Interactions

J. S. Zweiback
(Ph.D. Thesis)

June 1999



Lawrence
Livermore
National
Laboratory

DISCLAIMER

This document was prepared as an account of work sponsored by an agency of the United States Government. Neither the United States Government nor the University of California nor any of their employees, makes any warranty, express or implied, or assumes any legal liability or responsibility for the accuracy, completeness, or usefulness of any information, apparatus, product, or process disclosed, or represents that its use would not infringe privately owned rights. Reference herein to any specific commercial product, process, or service by trade name, trademark, manufacturer, or otherwise, does not necessarily constitute or imply its endorsement, recommendation, or favoring by the United States Government or the University of California. The views and opinions of authors expressed herein do not necessarily state or reflect those of the United States Government or the University of California, and shall not be used for advertising or product endorsement purposes.

This report has been reproduced
directly from the best available copy.

Available to DOE and DOE contractors from the
Office of Scientific and Technical Information
P.O. Box 62, Oak Ridge, TN 37831
Prices available from (615) 576-8401, FTS 626-8401

Available to the public from the
National Technical Information Service
U.S. Department of Commerce
5285 Port Royal Rd.,
Springfield, VA 22161

Resonance Effects in Laser Cluster Interactions

**J. S. Zweiback
(Ph.D. Thesis)**

June 1999

LAWRENCE LIVERMORE NATIONAL LABORATORY
University of California • Livermore, California • 94551

Resonance Effects in Laser Cluster Interactions

J. S. Zweiback
(Ph.D. Thesis)

June 1999



Lawrence
Livermore
National
Laboratory

DISCLAIMER

This document was prepared as an account of work sponsored by an agency of the United States Government. Neither the United States Government nor the University of California nor any of their employees, makes any warranty, express or implied, or assumes any legal liability or responsibility for the accuracy, completeness, or usefulness of any information, apparatus, product, or process disclosed, or represents that its use would not infringe privately owned rights. Reference herein to any specific commercial product, process, or service by trade name, trademark, manufacturer, or otherwise, does not necessarily constitute or imply its endorsement, recommendation, or favoring by the United States Government or the University of California. The views and opinions of authors expressed herein do not necessarily state or reflect those of the United States Government or the University of California, and shall not be used for advertising or product endorsement purposes.

This report has been reproduced
directly from the best available copy.

Available to DOE and DOE contractors from the
Office of Scientific and Technical Information
P.O. Box 62, Oak Ridge, TN 37831
Prices available from (615) 576-8401, FTS 626-8401

Available to the public from the
National Technical Information Service
U.S. Department of Commerce
5285 Port Royal Rd.,
Springfield, VA 22161

Resonance Effects in Laser Cluster Interactions

**J. S. Zweiback
(Ph.D. Thesis)**

June 1999

LAWRENCE LIVERMORE NATIONAL LABORATORY
University of California • Livermore, California • 94551

Resonance Effects in Laser Cluster Interactions

by

Jason Stuart Zweiback

B.S. (Cornell University) 1993

M.S. (University of California, Davis) 1996

DISSERTATION

Submitted in partial satisfaction of the requirements for the degree of

DOCTOR OF PHILOSOPHY

in

Engineering: Applied Science

in the

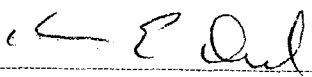
OFFICE OF GRADUATE STUDIES

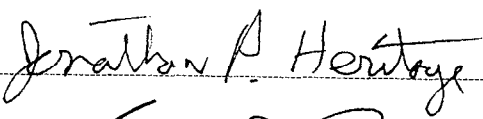
of the

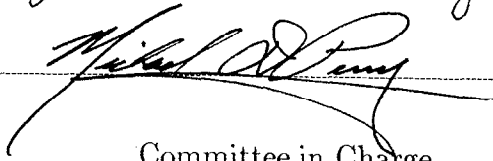
UNIVERSITY of CALIFORNIA

DAVIS

Approved:







Committee in Charge

1999

Resonance Effects in Laser Cluster Interactions

Copyright 1999

by

Jason Stuart Zweiback

Resonance Effects in Laser Cluster Interactions

Abstract

Time resolved dynamics of high intensity laser interactions with atomic clusters have been studied with both theoretical analysis and experiment. A short-pulse Ti:sapphire laser system, which could produce 50 mJ of energy in a 50 fs pulse, was built to perform these experiments. The laser used a novel single grating stretcher and was pumped, in part, by a custom Nd:YLF laser system, including 19 mm Nd:YLF amplifiers.

It was found that there is an optimal pulse width to maximize absorption for a given cluster size. This optimal pulse width ranged from 400 fs for 85 Å radius xenon clusters to 1.2 ps for 205 Å radius xenon clusters. Using a pump-probe configuration, the absorption of the probe radiation was observed to reach a maximum for a particular time delay between pump and probe, dependent on the cluster size. The delay for peak absorption was 800, 1400, and 2100 fs for 85 Å, 130 Å, and 170 Å radius xenon clusters respectively. Model calculations suggest that these effects are due to resonant heating of the spherical plasma in agreement with the hydrodynamic interpretation of cluster interactions. While this simple hydrodynamic code produces reasonable agreement with data, it does not include bulk plasma or non-linear propagation effects and is limited to the regime where resonant behavior dominates.

We also measured the scattered laser light from the laser-cluster interaction. Similar

to the absorption measurements, there is an optimal pulse width which maximizes the scattered signal. This pulse width is larger than the optimal pulse width for absorption. This disagrees with model calculations which show both pulse widths being similar. Further experiments measuring the scattered light in a pump-probe configuration should help to resolve this disagreement.

Acknowledgements

Over the past 4 years or so I have been asking myself why anyone (especially me) would put themselves through the pain and suffering of a graduate program. While I had the first inkling when the experiments described in the bulk of this thesis worked, it was really driven home when the neutron experiments mentioned in the conclusion were successful. The thrill of scientific discovery is unique and something few experience. Of course there is also the reason of being able to be paid to play with really expensive and cool toys, but I digress.

Many people have helped me get through this ordeal. I would first like to thank my advisor Mike Perry. He helped with both the scientific and political battles that had to be fought to get to the end of my work. He made me perhaps the best supplied graduate student in the country, providing all equipment I needed, and quite a bit more that I didn't. He also taught me quite a bit about the business of science. Todd Ditmire, on whose previous work much of this thesis is based, provided helpful advice and insight as only one who is the leader in a field can. Paul Banks, "the non-linear guy," did quite a bit to get me through the first year in the lab as I was trying to learn what I was doing. Though he will claim he didn't know what he was doing either, his "blind leading the blind" method helped me to understand how to build lasers. His willingness to converse about the varied topics I would bring up helped those long days go a little faster. On the theoretical side, Mike Feit, Bruce Shore, and Sasha Rubenchik were always willing to talk and give their advice when I would come to them to discuss my latest problems. Two other people I would like to acknowledge are Rick Cross and Brad Golick for mechanical and electrical support in the lab. Both of these people were willing to help a poor graduate student when

they had much more important things to do. Their efforts were instrumental to finishing my work in the lab within the time constraints imposed. I would also like to thank the Lawrence Livermore National Laboratory for financial support during my studies.

My friends Pat, Jon, and Desha are probably most responsible for helping me maintain my sanity through these years. Their efforts in this area are greatly appreciated. My sister, Bonnie, also helped get me through and has my eternal gratitude. And finally I would like to thank my parents for their continuous support throughout the years.

Contents

List of Figures	x
List of Tables	xiii
1 Introduction	1
2 Terawatt class Ti:sapphire laser system	7
2.1 Background	7
2.2 Ti:sapphire front end	10
2.2.1 Oscillator	11
2.2.2 Stretcher	12
2.2.3 Regenerative amplifier	14
2.2.4 4 pass amplifier	16
2.3 High power 4 pass Ti:sapphire amplifier	20
2.3.1 Nd:YLF pump laser system	22
2.3.2 High power 4 pass Ti:sapphire power amplifier	31
2.4 High power back end	34
2.5 Compressor	35
2.6 19 mm Nd:YLF amplifier development	38
2.6.1 19 mm amplifier design	38
2.6.2 19 mm amplifier performance	40
2.6.3 Second harmonic conversion of 19 mm amplifier	45
2.7 Conclusion	47
3 Theory of laser-cluster interactions	48
3.1 Ionization	48
3.1.1 Optical field ionization	49
3.1.2 Collisional ionization	50
3.2 Heating mechanisms	52
3.2.1 Above threshold ionization	52
3.2.2 Inverse bremsstrahlung heating	52
3.2.3 Resonance in cartesian geometry	54
3.2.4 Resonance in a spherical geometry	58
3.3 Mie scattering	60
3.3.1 Historical perspective	60

3.3.2	Cross-sections	61
3.4	Cluster expansion	62
3.5	Computer simulation	65
3.6	Conclusion	72
4	Absorption and Soft X-ray Experiments	75
4.1	Experimental design	75
4.2	Cluster formation and characterization	75
4.3	Variable pulse width experiments	80
4.3.1	Experimental setup	81
4.3.2	Absorption measurements	83
4.3.3	X-ray measurements	86
4.3.4	Variable energy	88
4.3.5	Modeling	93
4.4	Two-pulse experiments, single time delay	95
4.4.1	Experimental setup	95
4.4.2	Experimental results	98
4.5	Two-pulse experiments, variable time delay	99
4.5.1	Experimental setup	99
4.5.2	Experimental results	99
4.5.3	Modeling	104
4.6	Conclusions	105
5	Mie Scattering Experiments	107
5.1	Experimental setup	107
5.2	Emission pattern	108
5.3	Scattering data	109
5.3.1	Scattering in xenon	110
5.3.2	Scattering in argon	111
5.4	Scattering and absorption	111
5.5	Conclusions	117
6	Conclusion and future directions	118
6.1	Future directions	119
6.1.1	Computer modeling	119
6.1.2	Electron emission	119
6.1.3	Neutron generation	121
6.1.4	X-ray emission	121
6.2	Conclusions	123
A	Derivation of the Mie Solution	124
A.1	Maxwell's equations and the vector wave equation	124
A.2	Expansion of the fields in spherical harmonics	128
A.2.1	Incident field	128
A.2.2	Internal and scattered fields	135
A.3	Determination of coefficients	137
A.4	Amplitude functions and cross-sections	139
A.5	Conclusion	141

List of Figures

1.1	Suppression of Coulomb barrier by the laser field	2
2.1	Laser system block diagram	10
2.2	30 fs Ti:sapphire oscillator	11
2.3	Diagram of pulse stretcher	12
2.4	Stretched laser pulse	13
2.5	Layout of regenerative amplifier	16
2.6	Buildup of regenerative amplifier	17
2.7	Stability of regenerative amplifier	17
2.8	Layout of first 4 pass amplifier	18
2.9	Effect of gain guiding on beam profile	19
2.10	Profile of output from first four pass amplifier	19
2.11	Stability of first 4 pass amplifier	20
2.12	Flat top beam profile	21
2.13	Beam profile in second 4 pass amplifier	21
2.14	Layout of Nd:YLF pump system	24
2.15	Stability of 9.5 mm Nd:YLF amplifier	29
2.16	Output of 9.5 mm Nd:YLF amplifier	30
2.17	Profile of IR beam at the doubling crystal	30
2.18	Second harmonic conversion of 9.5 mm amplifier energy	32
2.19	Profile of second harmonic beam at Ti:sapphire crystal plane	32
2.20	Layout of second 4 pass amplifier	33
2.21	Stability of second 4 pass amplifier	33
2.22	Layout of pulse compressor	36
2.23	Second-order autocorrelation	36
2.24	Scanning third-order autocorrelator	37
2.25	Third-order autocorrelation	37
2.26	19 mm Nd:YLF amplifier	39
2.27	19 mm Nd:YLF amplifier head cutaway view	39
2.28	Small signal gain in 19 mm amplifier	41
2.29	Radial gain profile in 19 mm amplifier	42
2.30	19 mm amplifier beam profiles	43
2.31	Saturated gain in 19 mm amplifier	44
2.32	Energy stability of 19 mm amplifier	45
2.33	Second harmonic conversion of 19 mm amplifier	46

3.1	Thin semi-infinite plasma	54
3.2	Geometry of ideal spherical plasma	58
3.3	Collisional heating and density of 100 Å initial radius xenon cluster with a 450 fs pulse	66
3.4	Electron temperature of 100 Å initial radius xenon cluster with a 450 fs pulse	66
3.5	Expansion velocity and radius of 100 Å initial radius xenon cluster with a 450 fs pulse	67
3.6	Heating of 100 Å initial radius xenon cluster using the small sphere approximation and the full Mie solution	68
3.7	Collisional heating and density of 100 Å initial radius xenon cluster with a 50 fs pulse	69
3.8	Density of different sized xenon clusters with a 450 fs pulse	70
3.9	Free-streaming of electrons from different sized xenon clusters with a 450 fs pulse	71
3.10	Coulomb and hydrodynamic pressure on xenon clusters with a 450 fs pulse	73
4.1	Cluster size as a function of Hagena parameter	77
4.2	Setup for cluster size measurement	78
4.3	Rayleigh scatter measurement for Xe	79
4.4	Experimental concept for variable pulse width experiments	80
4.5	Setup for cluster experiments	81
4.6	Image of focal spot with f/3 paraboloid	82
4.7	Absorption measurement for variable pulse length experiments in Xe	83
4.8	Absorption measurement for variable pulse length experiments in Ar	84
4.9	Absorption measurement for both positive and negative chirp in Ar.	85
4.10	Argon spectra	87
4.11	Xenon spectra	89
4.12	Absorption and x-ray intensity from 300 psi Ar	90
4.13	Absorption as a function of intensity from 190 psi Xe, 50 fs pulse	91
4.14	Absorption as a function of intensity for 190 psi Xe, 1.2 ps pulse	92
4.15	Model calculations for variable pulse width data in Xe	93
4.16	Experimental concept for pump-probe experiments	96
4.17	Experimental setup for pump-probe experiments	97
4.18	Absorption measurements for pump-probe experiments in xenon	100
4.19	Absorption measurements for pump-probe experiments in argon	102
4.20	Expansion velocity for 2 pulse cluster irradiation	103
4.21	Computational model for xenon pump-probe data	104
5.1	Emission pattern for scattered laser light	108
5.2	Emission pattern for plasma light	109
5.3	Scattering in xenon	110
5.4	Scattering in argon	111
5.5	Scattering and absorption in xenon	112
5.6	Calculated scattering and absorption cross sections from Mie theory	113
5.7	Calculated dielectric constant for an expanding plasma sphere	114
5.8	Calculated cross-sections for an expanding plasma sphere	115
5.9	Calculated scattering and heating in xenon	116

6.1	Electrons seen on CCD camera	120
6.2	TOF data from neutron generation experiments	122

List of Tables

2.1	Laser parameters of various materials	22
4.1	Data from initial prepulse experiment	98

Chapter 1

Introduction

The interaction of electromagnetic radiation with matter is one of the fundamental areas in physics. These interactions form the basis for many different phenomena, from simple laser heating of materials to astrophysical events. With the first successful operation of a laser¹ a new experimental window was opened into this important realm of physics. There was now a source which could produce a coherent optical field, allowing very basic interaction theories to be experimentally tested.

Optical ionization of gases was observed soon after the invention of the laser.² Since the ionization potential of the gases used was greater than the energy of an optical photon, many photons need to be absorbed for ionization to occur. This multi-photon ionization had not previously been observed since it is a highly nonlinear process and the high incident photon density needed to observe it was not available before the invention of the laser. Theory was developed to explain multi-photon ionization and it was successfully described both quasi-classically³ and by perturbation theory.⁴

Keldysh³ also realized that in very large fields the ionization mechanism will change. Once the electric field of the laser is on the order of the nuclear Coulomb field, the laser can

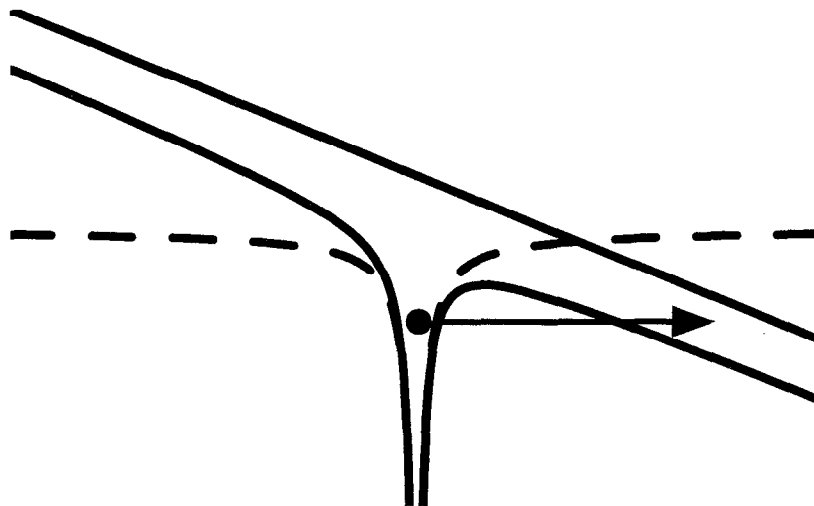


Figure 1.1: The Coulomb potential (dashed line) is altered in the presence of the laser potential (straight line). An electron in the potential well can now tunnel through the barrier (solid line).

suppress the atomic potential to the point where an electron can tunnel through the barrier (see Fig. 1.1). Many studies of the ionization of noble gases have been carried out.^{5,6} These have shown that as the intensity increases we move from multi-photon ionization to tunnel ionization.⁷

The field produced by early Q-switched lasers was large compared to what was previously available, but still small compared to the field produced by the nucleus ($\sim e/a_0^2$). Mode-locked lasers increased the available intensities, but these systems were limited to peak intensities of 1-10 GW/cm² in the amplifying medium. At this point, non-linear effects will cause the beam to self focus, causing catastrophic damage. The introduction of chirped pulse amplification⁸ (CPA) has made it possible to generate very large electric fields on the order of, and in some cases much larger than, the field from the nuclear Coulomb potential.⁹ CPA circumvents the self focusing problem by stretching the pulse in time before amplification. This reduces the peak intensity in the amplifiers, allowing safe amplification. After the amplifier chain, the pulse is recompressed to near its original pulse width, producing an

ultrahigh intensity laser pulse.

Electrons will be rapidly accelerated in this field. The kinetic energy of the electrons,

$$KE = \frac{e^2 \mathcal{E}_0^2}{2m_e \omega^2} \cos^2 \omega t, \quad (1.1)$$

where e is the elemental charge, \mathcal{E}_0 is the laser electric field, m_e is the electron mass, and ω is the laser frequency, can easily reach several MeV. It is important to note that this energy is oscillatory. Once the pulse has passed, if there have been no other interactions, the electron will not have gained any energy. In studying these interactions one looks for ways in which this energy can be transferred to the electrons.

Gas targets have often been studied in interaction experiments. Their low density allows one to study interactions with individual atoms. Along with their low density, however, comes low laser absorption (<1%). To increase absorption one can use solid targets. Very high absorption, up to 90%, has been seen in microstructured solid targets.¹⁰ In addition to the high absorption, high energy radiation and particles can be produced.¹¹ There is a price to be paid for using solid targets. Debris becomes an issue, as solid particles can coat and destroy expensive optics. Target management is more difficult since solid targets are generally destroyed when they are irradiated and have to be replaced. Additionally, the overall physics of the problem is more complicated. We have to take into account interatomic effects, which are negligible in a gas. Collisional heating and collisional ionization will play a major role in the interaction. These processes will increase absorption and plasma temperatures. However, since we only irradiate a portion of a solid target, the remaining cold material will conduct heat away from the interaction zone, causing rapid cooling.

Atomic cluster targets present a situation somewhere between gases and solids.¹² Clusters are small groups (tens to millions) of atoms held together with Van der Waals forces. These clusters can be formed by an adiabatic expansion of a gas into a vacuum. The

formation¹³ and electronic properties¹⁴ of clusters have been extensively investigated. Existing in a mesoscopic region, clusters can be studied to examine high density plasmas without the difficulties encountered when using true solids. The problems of target handling and debris are eliminated. Individual clusters have near solid density, allowing collisional processes to dominate the interaction. However, due to physical separation, each cluster behaves independently. This eliminates conductive cooling, allowing the plasma to remain hot for a long period of time.

The high field community's interest in clusters began in the early 90's. McPherson *et al.* used clusters to explain anomalous emission seen in experiments.¹⁵ The x-ray emission from an argon plasma showed much higher charge states than predicted by tunnel ionization. This observation was attributed to the presence of small clusters in the gas target.¹⁶ It was stated that the presence of these small clusters brings about inner-shell vacancies. This theory requires the production of prompt x-rays, since the recombination into these inner-shell vacancies will be very rapid.¹⁷ This built on earlier work by Rhodes *et al.*¹⁸ where he describes a process whereby inner shell electrons are excited by a coherent motion of the outer electron shell. There was debate in the literature as to the validity of this theory.^{19,20}

Rose-Petruck *et al.*²¹ created another model for these results. In this "ionization ignition model" the combined field of the laser and the closely spaced cluster ions cause a rapid ionization of the cluster, producing the observed high charge states. This model also included inner-shell vacancy production from electron-impact ionization. Because of the the computer intensive calculations required, this model was only run on small clusters up to 55 atoms.

Ditmire *et al.*²² showed, through Rayleigh scattering, that there are actually very large clusters in these gas targets, tens of thousands of atoms. He also demonstrated that the

radiation produced from the plasma is not prompt, but can actually last for nanoseconds. With this information, a hydrodynamic model of the laser cluster interaction was developed. This model was able to explain measured laser absorption²³ and energetic particles.²⁴

One important aspect of this model was the presence of resonant cluster heating. These clusters are much smaller than the wavelength of light. This allows us to treat the field outside of cluster as quasistatic. The field inside a small sphere (with complex dielectric constant) immersed in a uniform electric field is simply²⁵

$$E = \frac{3E_0}{|\epsilon + 2|} \quad (1.2)$$

Where E_0 is the external field and ϵ is the complex dielectric constant. Clearly, when $\epsilon \approx -2$ there is an enhancement of the field inside of the cluster. This leads to rapid heating of the cluster. This enhancement occurs because of a resonance when the cluster plasma is driven at its natural frequency. The dielectric constant is a function of the electron density in the plasma. In a bulk plasma the resonance will occur when the electron density equals the critical density, $n_e/n_{crit} = 1$ ($n_{crit} = m_e\omega^2/4\pi e^2$). In a spherical cluster plasma, as will be shown in chapter 3, the resonance condition will occur when $n_e/n_{crit} = 3$ due to the geometry of the problem.²² Once this resonance is reached the cluster heats greatly and undergoes rapid expansion. When this occurs, high energy electrons²⁶ and ions²⁷ are produced.

The goal of the research presented here was to observe direct evidence for the existence of resonant heating in cluster interactions. The initial experiment was to look at the effects of a variable pulse width on absorption. Once a cluster is ionized it will form an overdense plasma. It will take time, on the order of hundreds of femtoseconds, to expand and reach the resonance condition. A 50 fs laser pulse should be gone before the resonance is reached and hence absorption of such a pulse would be low. Making the pulse longer will allow

more time for the cluster to expand. The resonance condition will be reached during the laser pulse and absorption will increase. A very long laser pulse will mostly interact with a greatly expanded cluster. Cluster effects should play a small role in these interactions, and we expect to see low absorption similar to a pure gas.

There are two main sections to this dissertation. The first section is contained in Chapter 2 and will discuss the design and construction of the terawatt class Ti:sapphire CPA laser system used for these experiments. The front end of this system has been described previously,²⁸ and will be briefly reviewed; the final power amplifier, producing 175 mJ, will be discussed in more detail. There will also be a discussion of the characteristics of a 19 mm Nd:YLF amplifier developed to pump high power stages of a future laser.

The remaining chapters will discuss interactions between high intensity laser radiation and atomic clusters. The theory behind these interactions will be presented in Chapter 3. Of particular interest in this chapter is how the plasma resonance frequency is modified by the spherical geometry of a cluster plasma. Experimental results, measuring absorption and soft x-ray emission are the subject of Chapter 4. These experiments were carried out both in a pump-probe setup and using a variable pulse width. Chapter 5 will deal with Mie scattering of the laser pulse, and how pulse length affects the measured signal. Finally, conclusions and future work will be presented in Chapter 6.

Chapter 2

Terawatt class Ti:sapphire laser system

2.1 Background

In the past years, there has been a revolution in laser technology. Laser pulse widths have decreased and peak powers have increased. Pulse widths in the 10 fs regime are easily achievable^{29,30} and lasers with a peak power of 100 terawatts³¹ and even greater than a petawatt³² have been demonstrated. The enabling technologies that have made these changes possible are the introduction of Ti:sapphire³³, the introduction of chirped pulse amplification,⁸ and the development of high damage threshold, high efficiency diffraction gratings.³⁴

As mentioned in the introduction, at intensities of a few GW/cm² non-linear effects will cause damage to laser amplifiers. In order to get around this problem there are two choices: either use very large amplifiers and increase the beam area, or increase the pulse length in the amplifiers, reducing the peak power. For a 1 TW laser pulse, the area would have to be

1000 cm², or a beam diameter of 36 cm, to bring the intensity down to 1 GW/cm². This is certainly out of the range of a small table top laser system. The expense of obtaining optics and the laser medium, if it could even be produced, would limit this kind of system to very large laboratories.

Increasing the pulse width is a much more attractive solution. We need a device which will increase the pulse width and allow us to return it to its original state after amplification. In 1969 Treacy³⁵ showed that transmission through a pair of parallel diffraction gratings will produce negative dispersion in a laser pulse. This system creates a frequency dependent delay in the pulse, with the red side of the spectrum traveling a longer distance than the blue. A transform limited pulse will get longer after it passes through a grating pair, with the instantaneous frequency decreasing in time, called negative chirp. If a pulse is positively chirped before the grating pair, it will be compressed.

To introduce positive dispersion with a grating pair would require a negative grating spacing, a seeming impossibility. It had been proposed to use self-phase modulation (SPM) in the amplifiers to create a positive chirp.^{36,37} SPM in a fiber was used experimentally to create a positive chirp for amplification,⁸ but these systems were limited in their ability to stretch a pulse. Martinez³⁸ showed that by placing a one to one imaging telescope between the gratings, and placing the gratings within the focal length of the lenses, one can obtain the equivalent of a negative grating spacing. This idea was implemented³⁹ and has become the basis for modern CPA systems. Though they can be interchanged, usually the grating pair is used for the compressor and the system with a telescope is used as the stretcher. This minimizes non-linear effects and loss since the addition of the telescope adds optical elements which will either be transmissive, adding non-linear phase to the pulse, or reflective, adding loss.

The width of the final laser pulse is ultimately limited by the bandwidth which can be supported by the laser system. The uncertainty principle tells us that the time-bandwidth product $\Delta t \Delta \nu$ must be greater than .441 for a gaussian shaped pulse (using FWHM values). At 820 nm, in terms of wavelength, this becomes $\Delta t(fs) \Delta \lambda(\mu m) \geq .99$. This says that in order to obtain a 50 fs pulse we must pass 20 nm through the system. The laser system is limited by the initial bandwidth of the oscillator, the bandpass of the stretcher and compressor, the gain bandwidth of the lasing medium, and the frequency dependence of transmission and reflection of the laser optics.

The largest concern in the system is the gain medium. The stimulated emission cross-section is a function of wavelength and the initial laser spectrum will narrow as it is amplified. The cross section of Ti:sapphire has a FWHM ~ 225 nm peaking at 795 nm.³³ In an oscillator, this material would be able to support pulses below 3 fs. However, as we amplify the pulse, gain narrowing will limit the pulse width. A flat input spectrum, amplified by 10^7 , will narrow to around 50 nm, or a pulse length of 20 fs. For the most part, this is the practical limit of a terawatt level Ti:sapphire CPA system. Previous work has shown that the bandwidth can be increased by balancing the frequency dependent loss with the frequency dependent gain in a regenerative amplifier.⁴⁰ This has recently been accomplished by the introduction of an etalon into the cavity.⁴¹ The etalon is designed such that the convolution of the gain of Ti:sapphire and the etalon transmission function is constant over the laser bandwidth. This does increase the bandwidth which passes through the system and reduces the width of the final laser pulse. The price to be paid is modulation on the spectrum due to the etalon, which will degrade pulse quality in the time domain.

In this chapter, we will discuss the design and performance of a terawatt class Ti:sapphire CPA laser system. A block diagram of the laser is shown in Fig. 2.1. The short upperstate

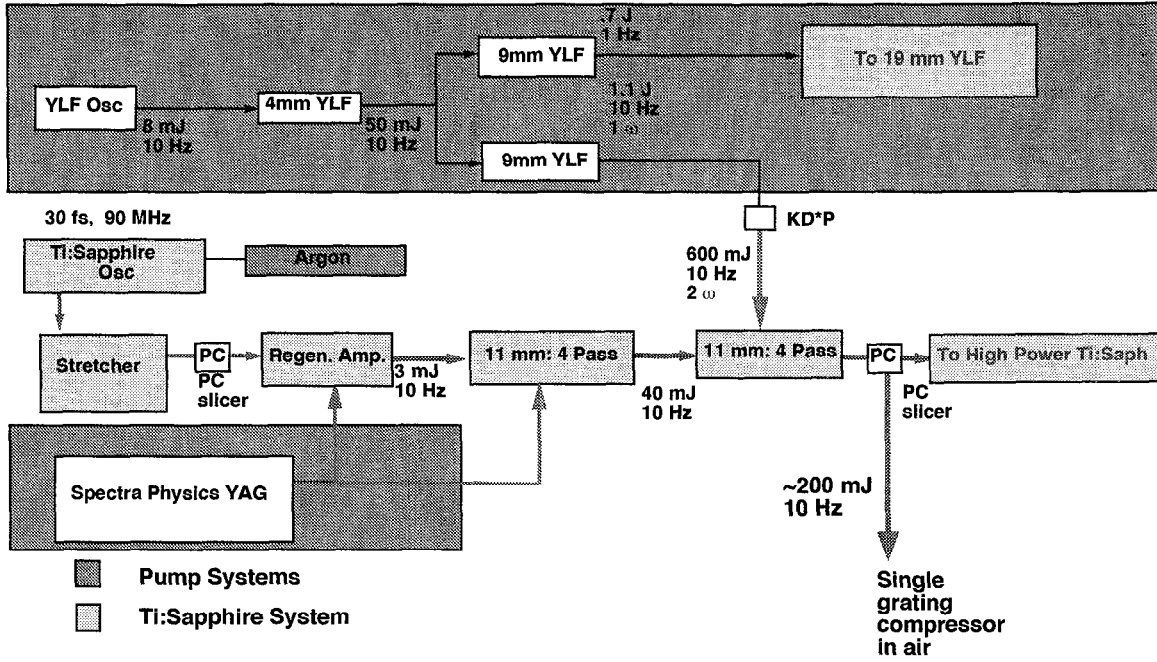


Figure 2.1: Block diagram of terawatt class Ti:sapphire CPA laser system.

lifetime of Ti:sapphire ($\sim 2\mu\text{s}$) necessitates laser pumping. Therefore, the system actually consists of two lasers: the Ti:sapphire system, and a pump system consisting of a commercial Nd:YAG laser and a custom Nd:YLF laser. Much of this system has been discussed before, and hence will only be briefly reviewed. Readers who want more details about the laser front end are referred to Fochs⁴² and Banks.²⁸

2.2 Ti:sapphire front end

The front end of this laser system will be defined as the components up through the amplifiers pumped with the commercial Nd:YAG laser. This consists of the oscillator, stretcher, regenerative amplifier, and first 4 pass power amplifier. Most of the gain ($\sim 10^7$) is produced in this part of the laser system. The high gain means it will produce most of the gain narrowing.

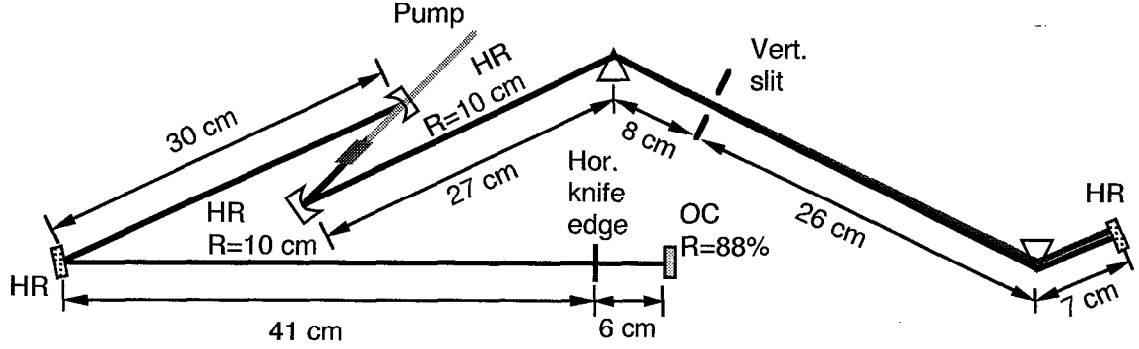


Figure 2.2: Schematic of 30 fs Ti:sapphire oscillator.

2.2.1 Oscillator

The Ti:sapphire oscillator is shown in Fig. 2.2. It is a standard Kerr-lens mode locked system⁴³ and was built as part of a master's thesis.⁴² It uses a 10 mm long Ti:sapphire rod with .1% doping. Dispersion compensation is done with a pair of LAKL21 prisms. It is pumped with about 7 W of power from a Coherent Innova 310 argon-ion laser running on all lines. This high pump power was used since it was necessary to run the argon laser above 45 amps to maintain proper tube pressurization. To compensate for the high pump power, an output coupler with 12% transmission was used. This lowered the intracavity power to the point where the oscillator was stable. Other features of this cavity are an adjustable slit between the prism pair, which could be used to tune the spectrum of the laser; and a horizontal knife edge on the lower part of beam near the output coupler, which was found to improve cavity stability.

The oscillator produced a 92 MHz pulse train of 30 fs pulses. The modelocked output power was 500 mW. The laser would maintain modelocking for many hours at a time. However, the cavity would revert to CW operation at least once a day. At this time the pointing of the pump laser had to be adjusted. It is believed that changes in the cooling

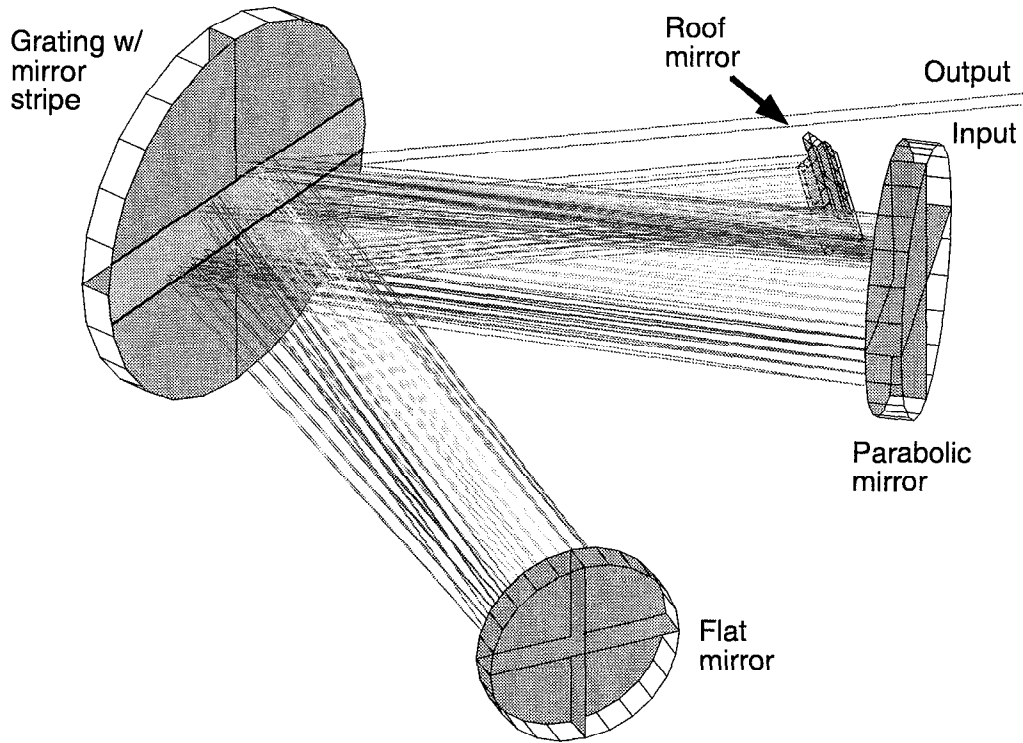


Figure 2.3: Diagram of the pulse stretcher.

water temperature (rise of up to 5° C over the day) were responsible for the argon laser pointing drift.

2.2.2 Stretcher

Figure 2.3 shows the design of the pulse stretcher in this laser.⁴⁴ The stretcher is unique in that it has the grating pair and a fold mirror all on a single optic. Therefore, these components are always aligned. We were able to manufacture this optic with our large scale, holographic grating fabrication facility. The optic is a 12" grating with an opaque mask placed over it during exposure so that the grating pattern is not printed on a 2" stripe centered vertically on the optic. The entire stretcher consists of only 4 individual optics,

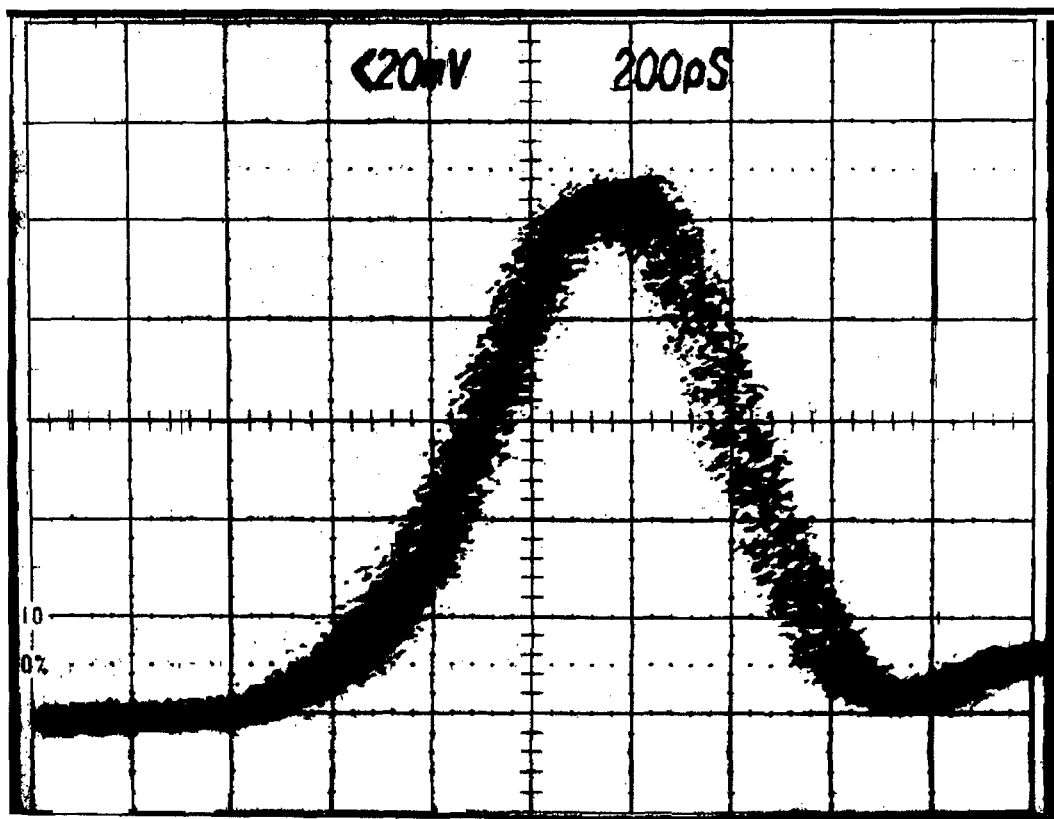


Figure 2.4: Sampling scope trace of the stretched laser pulse.

making the system very easy to align and maintain. The line spacing on the grating is 1480 l/mm.

The beam from the oscillator comes into the upper grating and is diffracted at the HeNe Litrow angle (27.92°) to the spherical mirror ($f=113$ cm). This angle was chosen so that a HeNe laser (632.8 nm) could be used to align the system. The pulse then goes to the mirror stripe on the grating optic, the flat mirror, back to the mirror stripe, the curved mirror, and the lower grating. At this point the dispersed beam goes to the roof mirror and is sent back through the system a second time. The pulse is stretched approximately 20,000 times. The final pulse (shown in Fig. 2.4) is 600 ps long. The energy is down to 20% of the original due to the loss from many reflections off of gold surfaces and the diffraction

efficiency of the grating. This stretcher design can pass 60 nm of bandwidth, limited by the size of the optics.

Originally, instead of a spherical mirror, we had used a parabolic mirror. It was thought that aberrations could be eliminated with a parabola. However, this is only true when the grating is in the focal plane of the parabolic mirror, at which point the stretching ratio is 1. When the grating is in the proper location there are very large aberrations which cause broadening of the pulse on recompression.²⁸ This caused us to use a spherical mirror. The spherical mirror in the telescope does impart aberrations on the laser pulse. However, in this case the aberrations can be used to help compensate for higher order dispersion.⁴⁵ For this configuration, the spherical aberration helps to eliminate uncompensated 4th order dispersion, allowing for a near transformed limited pulse to be produced after compression.

After the stretcher output, the pulse train is chopped to 10 Hz using a Lasermetrics half-wave Pockels cell driver. The pulse is now ready to seed the 10 Hz front end amplifiers.

2.2.3 Regenerative amplifier

The first amplification stage in these lasers is generally referred to as a preamplifier. The purpose of the preamplifier is to bring the small nanojoule energy level pulses which come out of the stretcher up to the millijoule level. The gain will be several million, which is significantly larger than in the other amplifiers. This large amount of gain will narrow the spectrum of the pulse due to the finite bandwidth of the gain medium and cavity optics. Care must be taken to pass as much bandwidth as possible through this amplifier.

One can use a multipass or a regenerative amplifier in this stage. Multipass amplifiers have the advantage that the only transmissive element is the gain medium. This reduces material dispersion making it easier to compensate for the total pulse dispersion after the

amplifiers. We originally used an 8 pass amplifier. The amplifier consisted of two sets of eight 1" mirrors in a circular configuration. The two sets of mirrors were 1 m apart with a 5×24 mm brewster-cut Ti:sapphire rod between them. The alignment of this amplifier was very difficult and time consuming. With 100 mJ of 532 nm pump light, the amplifier only produced 1 mJ of energy. The stability was poor, with the output energy varying by 10%.

Since the multipass amplifier worked poorly, we decided to build a regenerative amplifier. This kind of amplifier uses a resonant cavity. The seed pulse is switched into the cavity electro-optically. Once trapped in the cavity, the pulse will gain energy every pass through the gain medium. Once the peak energy is achieved, the pulse is switched out. All elements inside of the cavity are passed through many times. This means the effect of any one element will be multiplied 20-40 fold. The material dispersion is the equivalent of about 1 m of KD*P from the Pockels cell and 1 m of Ti:sapphire. This will have to be compensated for in the compressor. The polarizers which we used reflected nearly all s-polarized (electric field perpendicular to the plane of incidence) light, but only transmitted 96% of the p-polarized (electric field parallel to the plane of incidence) light. Additionally, the spectrum would be narrowed about 8% after transmission through the polarizer. This necessitated using the polarizer in reflection to maximize the bandwidth of the output of the regenerative amplifier.

The layout of the regenerative amplifier is seen in Fig. 2.5. The cavity is of a confocal design using 2 m radius of curvature mirrors separated by 2 m. The cavity is folded due to space considerations. The laser rod is centered between the mirrors and the seed beam is introduced to the cavity off the brewster face to the Ti:sapphire rod. The beam is s-polarized at this point and is passed though the Pockels cell, reflecting off the polarizer. Half-wave

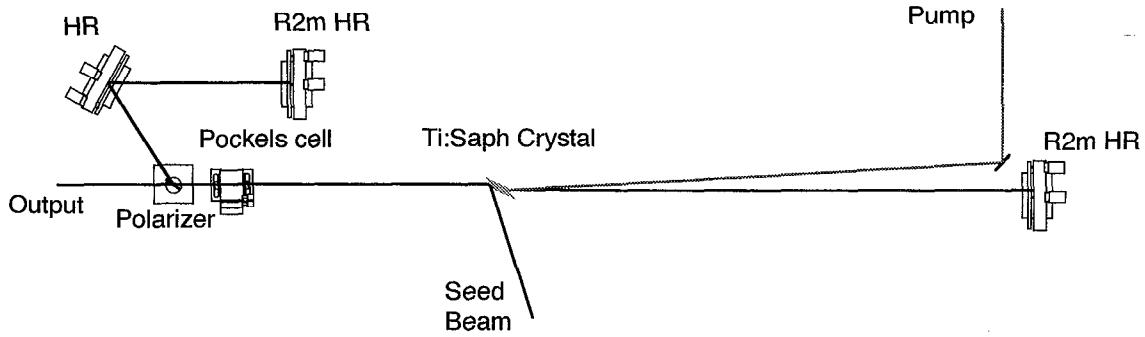


Figure 2.5: Layout of the regenerative amplifier. The polarizer is used in reflection to maximize bandwidth.

voltage (≈ 7200 V) is now applied across the Pockels cell. This rotates the polarization 90° whenever the pulse passes through the Pockels cell. Hence, the pulse will be s-polarized to the left of the Pockels cell and p-polarized to the right. This traps the pulse inside the cavity. Once the pulse has reached its full energy, the Pockels cell is switched off while the pulse is in the right side of the cavity. The pulse remains p-polarized and transmits through the polarizer, exiting the amplifier.

This amplifier performed much better than the original 8-pass. Using only 20 mJ of pump energy from the Spectra Physics GCR-190, almost 3 mJ of output could be achieved. The build up is shown in Fig. 2.6. Generally, we switched out the pulse one round trip after the peak. This produced the most stable output. A stability test is shown in Fig. 2.7. The stability is better than $\pm 2\%$ RMS. The pump beam would walk over the day and had to be adjusted periodically. This pointing drift was due to temperature changes in the laboratory.

2.2.4 4 pass amplifier

After the preamplifier, the pulse goes to the first of the power amplifiers. While the gain will be low for the power amplifiers (10-20), the increase of energy will be much greater than

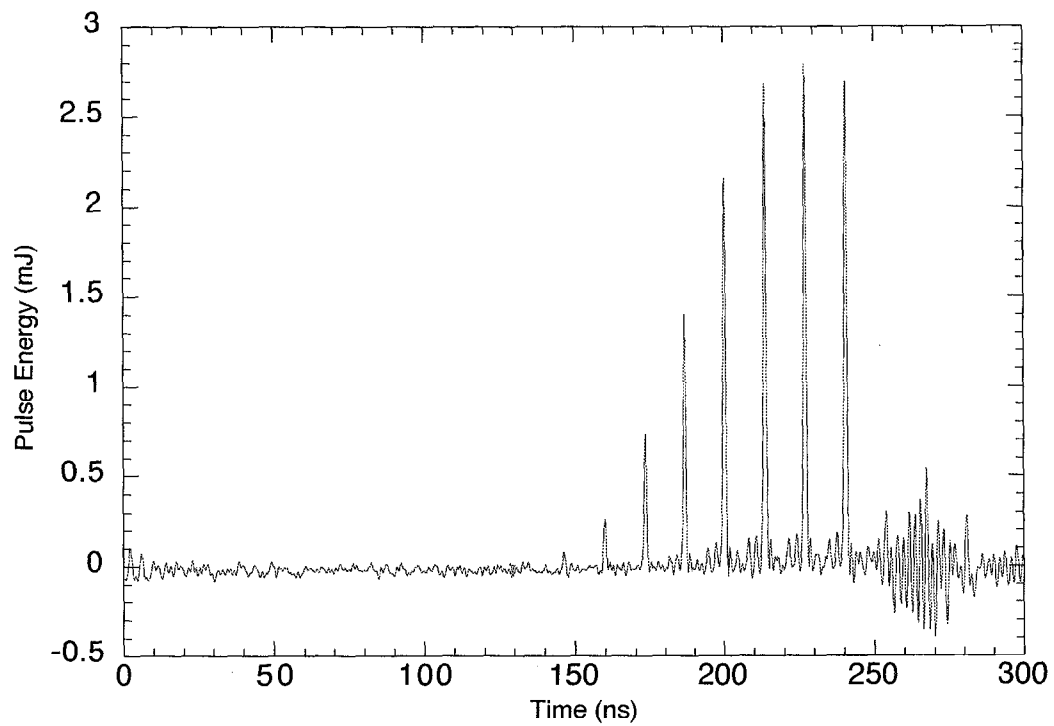


Figure 2.6: Energy buildup of regenerative amplifier. The oscillations after switchout are noise from the Pockels cell driver.

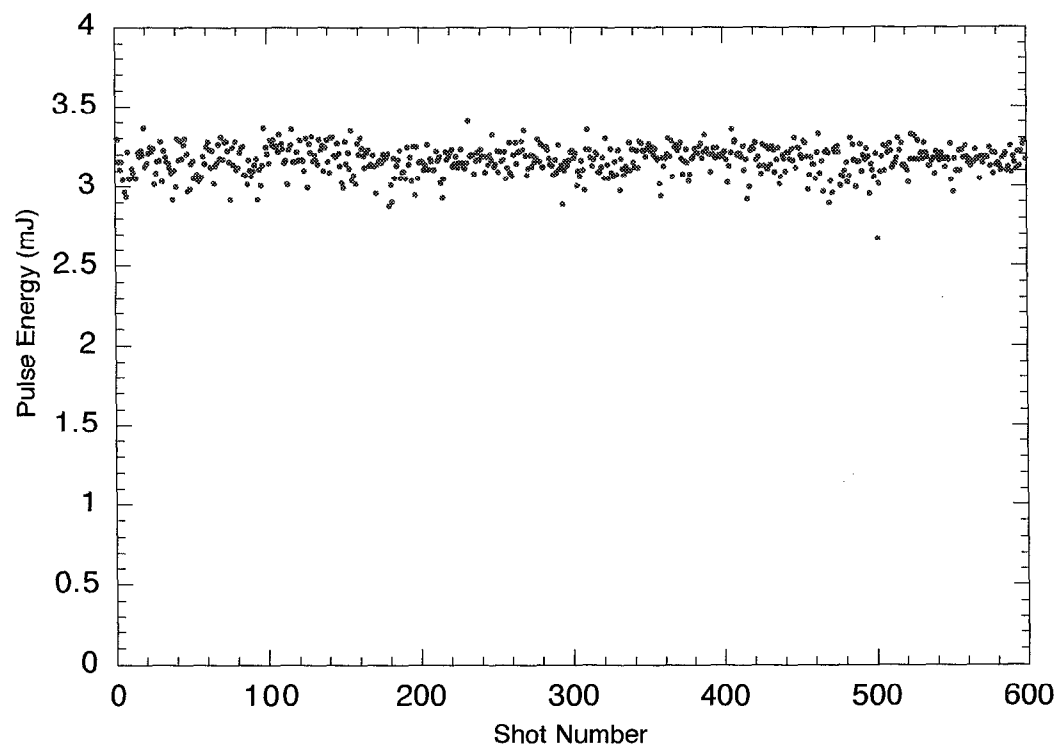


Figure 2.7: Stability of regenerative amplifier. Over 600 shots the stability is better than $\pm 2\%$ RMS.

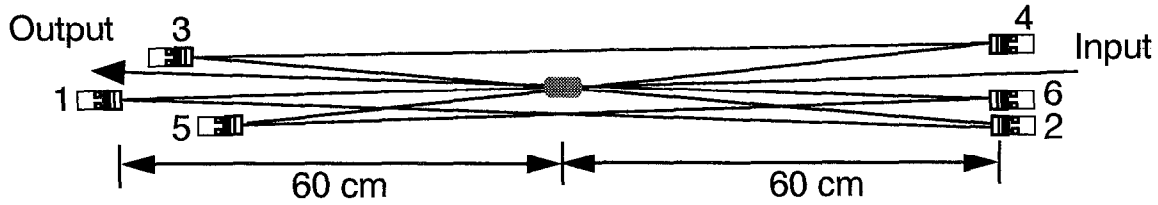


Figure 2.8: Layout of the first 4 pass amplifier.

in the pre-amplifier. Hence, much more pump energy is needed than in the regenerative amplifier. For efficient energy extraction we will run these amplifiers into the saturated regime and this will be reflected in our design.

This amplifier consists of six 1" dielectric mirrors and an 11×25 mm brewster-cut Ti:sapphire rod. The layout is shown in Fig. 2.8. The amplifier is pumped with approximately 250 mJ from the GCR-190. Since the GCR-190 pumps both the regenerative amplifier and the 4 pass amplifier, there is a delay of about 300 ns from when the pump beam excites the gain medium to when the seed beam arrives. This is a significant fraction of the $2 \mu\text{s}$ upperstate lifetime of Ti:sapphire. Hence, about 20% of the inversion is lost to spontaneous emission.

The seed beam waist is approximately 1 mm ($1/e^2$) when it enters the amplifier. Since this beam is propagating freely throughout this amplifier, the waist will increase due to diffraction. The effects of diffraction will be counteracted by the effects of the radial distribution of the gain in the rod. The pump beam can be approximated as a gaussian with a 2.8 mm waist. The amplified pulse will be the convolution of the gain profile and the seed beam, with the center of the seed being amplified more than the edges (Fig. 2.9). The formalism for calculating this can be found in the literature.⁴⁶ In order to maximize energy extraction, the path lengths must be chosen such that the combined effect of these two phenomena cause the mode volume to be properly filled on each pass.

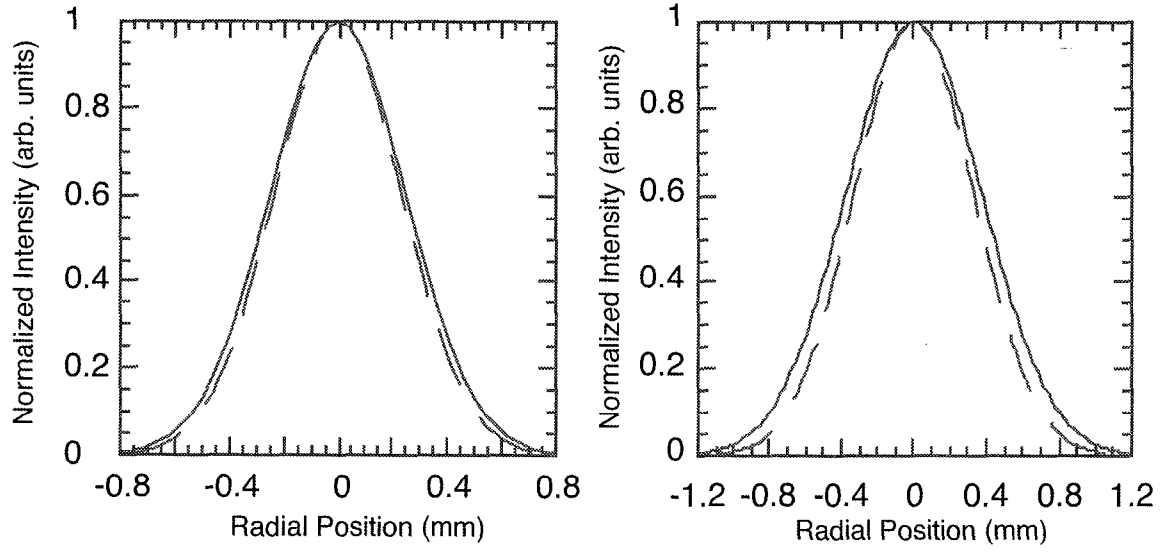


Figure 2.9: The effect of gain guiding is shown. The solid lines are the original pulse and the dashed lines are the amplified pulse. The radial gain profile used is a 2.8 mm ($1/e^2$) gaussian. The plot on the left shows the effect on a 1 mm gaussian beam. It narrows about 6% after being amplified. The larger the beam, the larger the gain guiding effect. The plot on the right shows the effect on a 1.5 mm gaussian beam. Now the beam narrows by 12%.

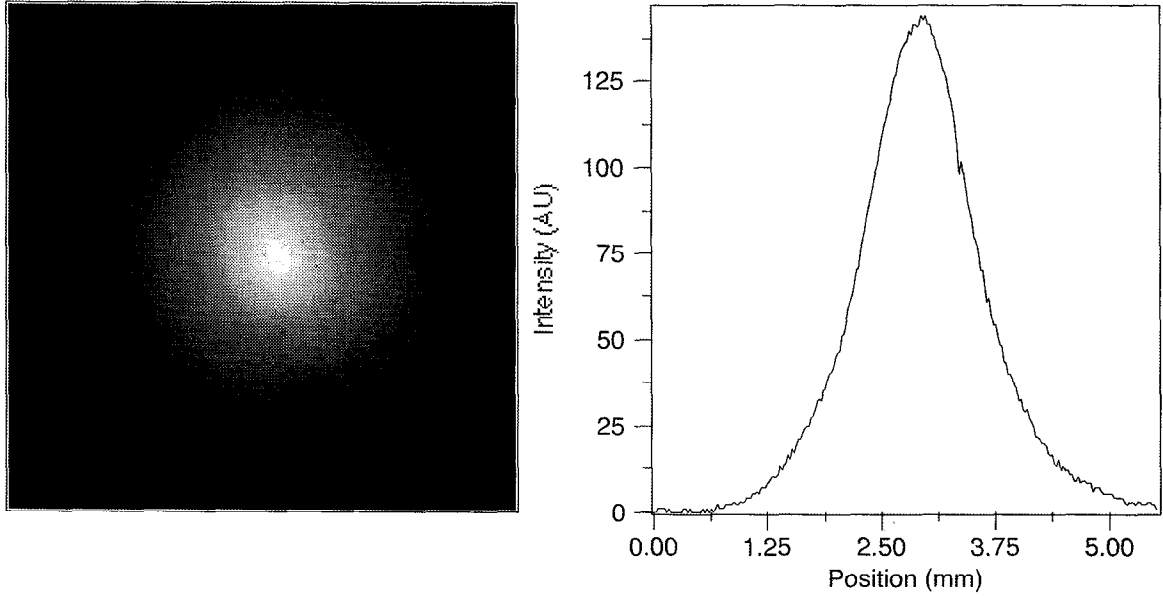


Figure 2.10: Profile of output from the first four pass amplifier.

This amplifier produced between 40 and 50 mJ of energy, depending on the condition of the pump laser. The beam profile is gaussian (Fig. 2.10) and is expanding slightly when

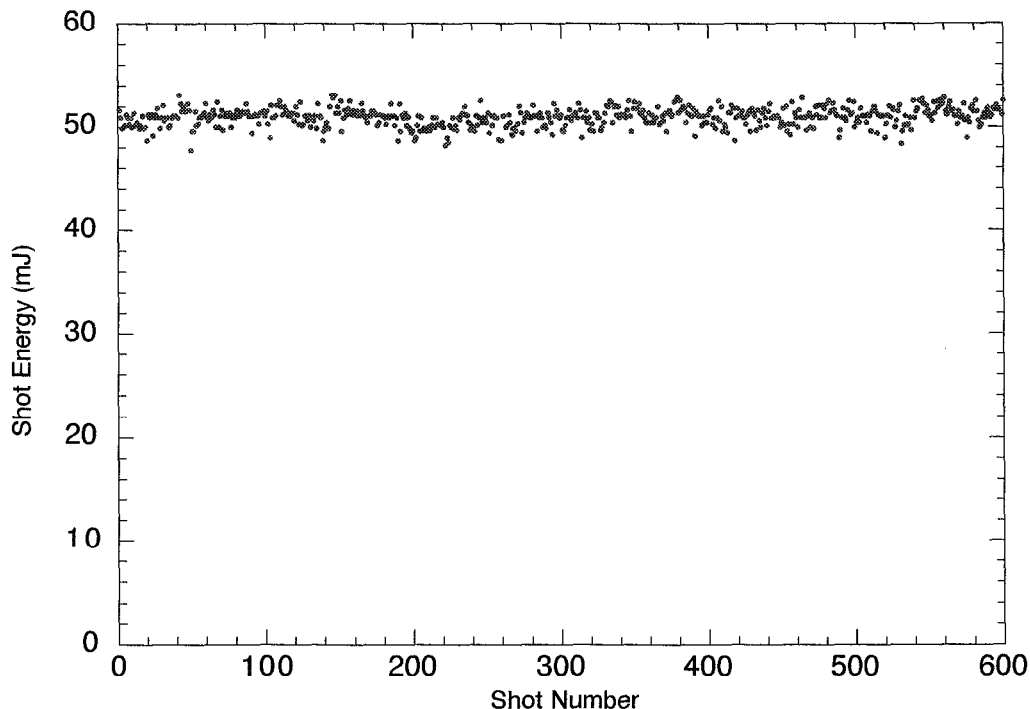


Figure 2.11: Stability of the first 4 pass amplifier.

it exits. The stability was better than $\pm 2\%$ RMS as seen in Fig. 2.11.

2.3 High power 4 pass Ti:sapphire amplifier

After the laser front end the beam is still gaussian. In order to maximize extraction in the high power amplifiers we want to have a flat top beam profile. To obtain this we clip the beam with a serrated aperture to obtain a near flat top profile.⁴⁷ Slightly more than half of the energy from the beam is lost in this process. After the serrated aperture, we spatially filter the beam to remove the higher spatial frequencies which correspond to the serrated teeth in the profile. This produces a reasonable flat top profile as seen in Fig. 2.12.

A flat top beam will diffract as it propagates and must be imaged throughout the rest of the system. This is done with the use of standard telescopes. These are evacuated to

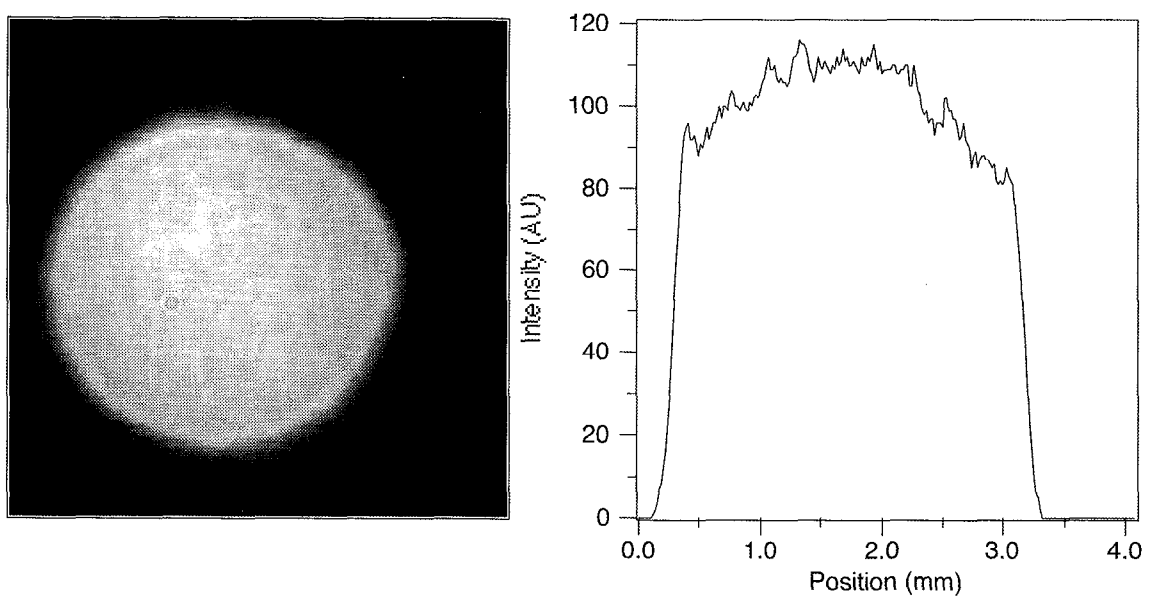


Figure 2.12: Beam profile after serrated aperture and spatial filter. The profile is taken at the image plane.

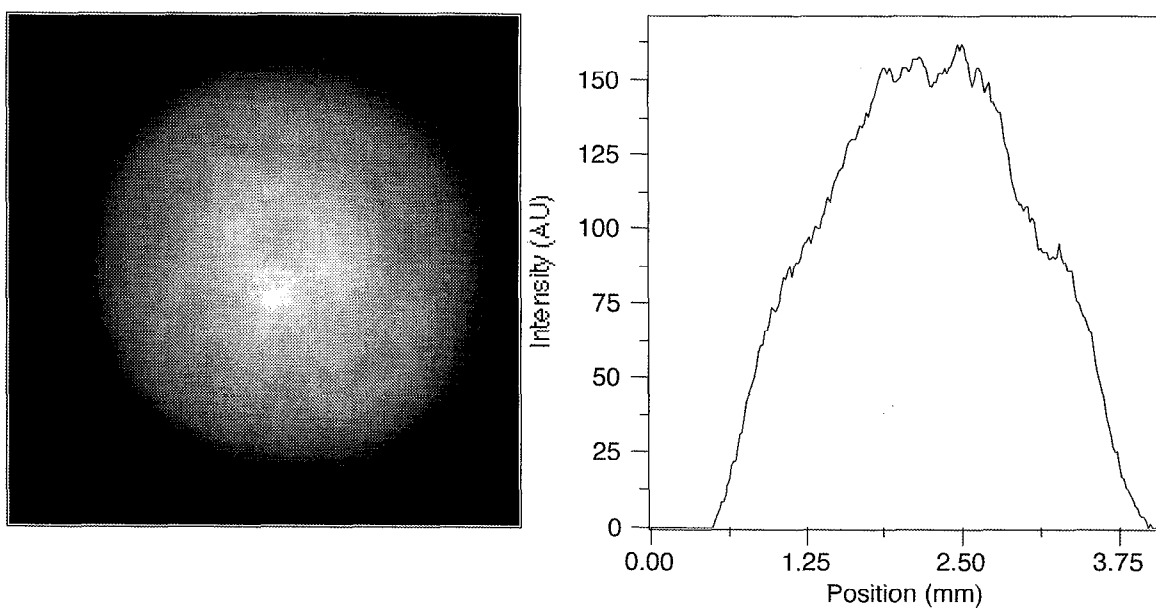


Figure 2.13: Beam profile inside of the second 4 pass amplifier. The change from Fig. 2.12 is due to clipping in a 1 cm Pockels cell and subsequent diffraction.

Table 2.1: Parameters of various laser materials for pump laser

Material	Nd:YAG	Nd:YLF	Nd:Glass
Peak Lasing wavelength [nm]	1064	1053 (σ) 1047 (π)	1054
Stimulated emission cross-section [cm ²]	2.8×10^{-19}	$1.2 \times 10^{-19}(\sigma)$ $1.8 \times 10^{-19}(\pi)$	4.3×10^{-20}
Upper state lifetime [μ s]	230	480	330
Lower state lifetime [ns]	.200	10.5	.228
Thermal conductivity [W/cm-K]	.14	.06	.0067

prevent breakdown at the focus. After an amplifier, we place a pinhole at the telescope focus to remove high spatial frequencies, improving beam quality. Between the telescope and the image plane the beam profile will change drastically as it propagates, often with energy moving far out into the wings of the profile. All limiting apertures can effect the image. Figure 2.13 shows the beam profile at the image plane inside of the the second 4 pass amplifier. The beam has now passed through a 1 cm Pockels cell. The low energy wings are clipped going through this aperture, removing some of the higher spatial frequencies. When the beam reaches the image plane, the steep sides are gone and we see a less uniform beam profile.

2.3.1 Nd:YLF pump laser system

As the requirement for pulse energy increases, it becomes necessary to have larger pump lasers to obtain the necessary gain. Though pump lasers up to the Joule level are commercially available, due to cost consideration, we decided to build our own pump laser system. The majority of this system would be scavenged from old laser systems so the cost was minimal.

Many design parameters must be taken into account in choosing the laser material for this pump system. The parameters for three different gain media are shown in Table 2.1.^{48,49}

The original design for the laser required the pump laser to produce three separate beams with the following energies: 1 J, 8 J, and 40 J. Nd:Glass amplifiers can produce these energy levels, but the poor thermal properties of Nd:Glass would make it difficult to run the laser at 10 Hz repetition rate. Nd:YAG is often used in commercial laser systems at the Joule level. However, it cannot be grown in large sizes necessary for the high energy amplifiers. Nd:YLF is comparable with Nd:YAG. It too cannot be grown in large enough sizes for the highest energies needed. However, the lasing wavelength of Nd:YLF is close enough to the peak wavelength for Nd:Glass that an effective hybrid system can be built. Nd:YLF is used in the early amplifiers to keep the repetition rate high and Nd:Glass is used in the latter amplifiers to achieve the high energies at the expense of repetition rate. Up to the Joule level we can easily run the Nd:YLF system at 10 Hz. A pump system up to this level was constructed and used to pump the Ti:sapphire system. In the higher power amplifiers the repetition rate would have to be reduced due to fracture concerns. The high power back end of the pump system was to consist of two 19 mm Nd:YLF amplifiers operating in parallel, running at 1 Hz; these would be frequency doubled to produce a total of 4 J of 2ω (527 nm). The remaining fundamental light would then be sent into 19 mm and 45 mm glass rod amplifiers to produce 40 J of 1053 nm radiation. The repetition rate would be one shot every 8 minutes due to the thermal properties of glass. Although this back end turned out to be unnecessary for the experiments performed in this thesis, the 19 mm Nd:YLF amplifiers have been tested and will be discussed at the end of this chapter.

The Nd:YLF pump laser is a standard master oscillator, power amplifier (MOPA) system. The layout of the front end can be seen in Fig. 2.14. The system begins with a simple ring oscillator, followed by two stages of amplification. The system has approximately a $2' \times 4'$ footprint.

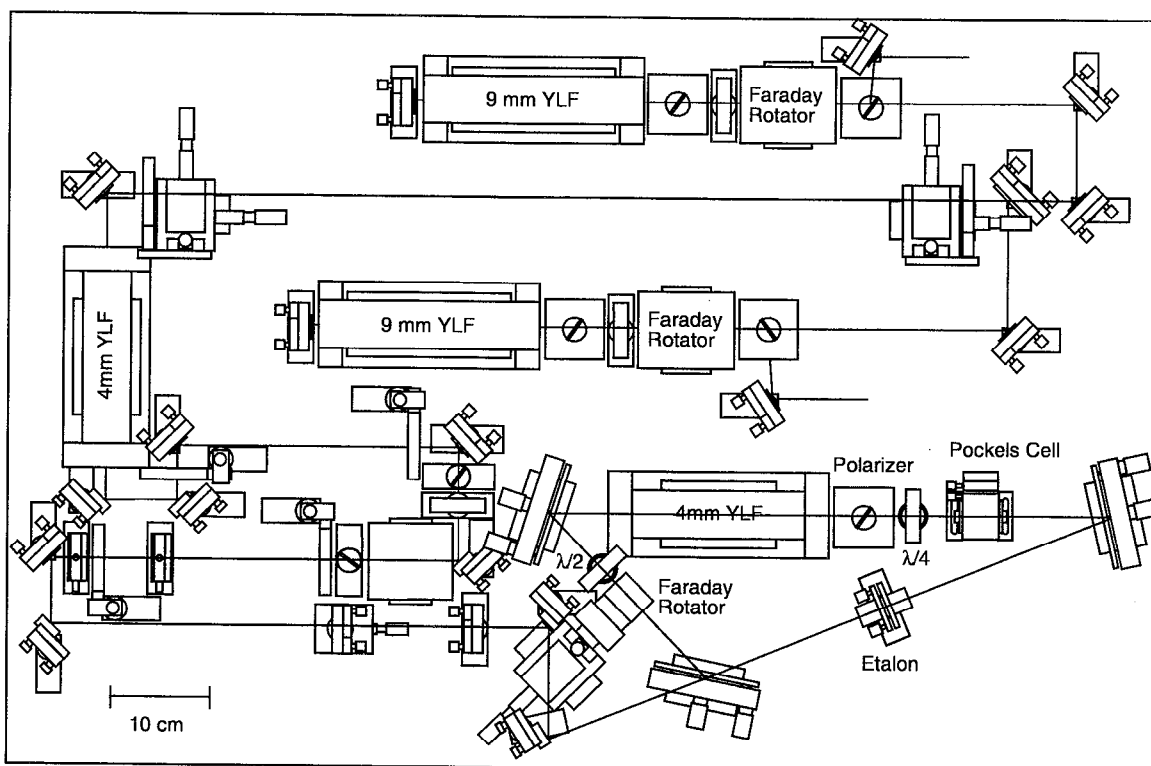


Figure 2.14: Layout of the Nd:YLF pump system.

Oscillator

A ring oscillator was chosen because of its energy stability and better longitudinal mode control than a linear oscillator. We used a design developed at LLNL for high energy phase conjugate lasers.⁵⁰ This cavity is formed by a 4 mm flashlamp pumped Nd:YLF amplifier head, two high reflectors (one 5 m radius of curvature), and a polarizer used as the output coupler. There is an internal polarizer to prevent oscillation of the higher gain 1047 nm wavelength. A small Faraday rotator and a half waveplate ensure unidirectional operation. An aperture is placed in the cavity and sized to produce TEM₀₀ output. A quarter wave plate allow us to control the output coupling of the laser. A 30 mm etalon for longitudinal model control and a quarter wave Pockels cell for Q-switching are also in the cavity.

This oscillator is designed to be run with a single-longitudinal mode output. To accomplish this, a photodiode is set up to observe lasing inside of the cavity. The onset of lasing is detected by a discriminator, triggering the Q-switch. When lasing starts, the gain is just over the loss in the cavity so only one longitudinal mode has enough gain to oscillate. This single mode seeds the Q-switched pulse. Since this one mode has such a large initial population when the Q-switch is turned on, it dominates and the final output is single-longitudinal mode.

As a practical matter, there must be several hundred nanoseconds between the detection of lasing and the triggering of the Q-switch. The fast timing system of the laser must be triggered from this detection. Many other devices, delayed from the fast timing system, need to trigger before the Q-switch of the pump laser. This means a small foot, several hundred nanoseconds long, will be formed in front of the main Q-switched pulse. In a phase conjugate system this is not a problem. At low intensities the reflection of a phase conjugate mirror is negligible and this foot is effectively cut off. This is not true in our laser system.

This small foot will see a gain of several thousand. At the output of the system this foot will contain about one quarter of the energy of the pulse. Since the intensity is low, the foot will not convert well to the second harmonic and the energy will be lost.

Losing a quarter of the energy is unacceptable so we modified the operation of the oscillator. We removed the diode and operated the oscillator in a normal Q-switched mode, where the triggering of the Pockels cell is timed directly to the firing of the flashlamps. The oscillator no longer operated in single longitudinal mode; mode beating was observed from two modes in the cavity. The etalon helped with mode selection. Modulation was in the 5-10% range.

The oscillator ran very well once set up. Energy output was 10 mJ with $\pm 1\%$ RMS variations. We generally ran the system with a pulse width of 20 ns. With a new amplifier head and flashlamps, we could get the pulse width down to 15 ns, though this proved difficult to maintain for a long period of time due to degradation of the lamps and reflector inside of the pump head.

Amplifiers

After the oscillator, the beam is expanded slightly and clipped with a serrated aperture to produce a flat top beam. The beam is then relayed through a 4 mm Nd:YLF amplifier producing 60 mJ of energy. From here the beam is expanded to 8 mm. The beam is then split using an 80%/20% beam splitter. Each beam goes to a separate 9.5 mm Nd:YLF double pass amplifier. The lower energy leg was designed for seeding the 19 mm Nd:YLF amplifier to be discussed later. The high energy leg was used to pump the second 4 pass Ti:sapphire amplifier.

To further examine this amplifier, we constructed a saturated gain model. As the

energy is extracted from the rod the pulse energy saturates. The theory of saturated gain is governed by the well know Frantz Nodvick equations.⁵¹ Assuming a flat top beam profile, the energy gain can be expressed as

$$G_E = \frac{\int_0^\infty \phi(L, t) dt}{\int_0^\infty \phi(0, t) dt}, \quad (2.1)$$

where $\phi(x, t)$ is the photon flux as a function of location in the gain medium and time in the pulse, and L is the gain length. To find $\phi(x, t)$ we need the solutions to the coupled population rate equations

$$\frac{\partial \phi(x, t)}{\partial t} + v_g \frac{\partial \phi(x, t)}{\partial x} = \phi(x, t) v_g \sigma \Delta(x, t), \quad (2.2)$$

$$\frac{\partial \Delta(x, t)}{\partial t} = -\phi(x, t) v_g 2^* \sigma \Delta(x, t), \quad (2.3)$$

where $\Delta(x, t)$ is the difference in upper and lower state populations, v_g is the group velocity of light in the medium, and σ is the stimulated emission cross-section. The enigmatic factor 2^* is from Siegman.⁵² This factor takes into account bottlenecking that occurs in the lower level of the laser transition. For an ideal 4 level laser system, where the lowerstate lifetime is zero, $2^* = 1$. For a 3 level system, $2^* = 2$. For cases where the lower state of the laser transition has a finite lifetime, 2^* will fall somewhere between these two values. This parameter is important for Nd:YLF which has about a 10 ns lower state lifetime.⁴⁸ This is on the same order as the pulse width (20 ns), so we would expect bottlenecking to play a significant role in energy extraction.

The solutions⁵¹ to these equations are

$$\phi(x, t) = \frac{\phi(0, t - x/v_g)}{1 - (1 - \exp[-\sigma \int_0^x \Delta(x', -\infty) dx']) \exp[-2^* \sigma \int_{-\infty}^{t-x/v_g} \phi(0, t') dt']}, \quad (2.4)$$

$$\Delta(x, t) = \frac{\Delta(x, -\infty) \exp[-\sigma \int_0^x \Delta(x', -\infty) dx']}{\exp[-\sigma \int_0^x \Delta(x', -\infty) dx'] + \exp[2^* \sigma \int_{-\infty}^{t-x/v_g} \phi(0, t') dt'] - 1}. \quad (2.5)$$

Using these equations we can perform the integrals in Eq. 2.1, yielding

$$G_E = \frac{F_{sat}}{F_{in}} \log \left\{ 1 + G_0 \left[\exp \left(\frac{F_{in}}{F_{sat}} \right) - 1 \right] \right\}, \quad (2.6)$$

where F_{in} is the input fluence

$$F_{in} \equiv h\nu \int_{-\infty}^{\infty} \phi(0, t) dt, \quad (2.7)$$

h is Planck's constant, and ν is the laser frequency. G_0 is the small signal gain

$$G_0 \equiv \exp \left[\int_0^L \Delta(x, -\infty) dx \right], \quad (2.8)$$

and F_{sat} is the saturation fluence

$$F_{sat} \equiv \frac{h\nu}{2\sigma}. \quad (2.9)$$

Calculating single pass gain can be done by simply using Eq. 2.6 with the proper parameter values. However, for a double pass amplifier the problem is complicated by the fact that the pulse overlaps itself inside of the gain medium. We have a 20 ns pulse, which is 6 m long, FWHM. Once the front of the pulse passes through, it will be reflected by the mirror and pass back through the amplifier. The forward and backward going pulses will overlap inside of the gain medium, making the fluence seen in the amplifier the sum of these two pulses.

In order to calculate this effect, we discretized the laser pulse into rod length segments. The forward and backward going segments which were inside of the amplifier were summed together, and this number was used for F_{in} in Eq. 2.6. The energy of the segments was then adjusted for the calculated gain. Next, the pulse was advanced one segment and the algorithm was repeated.

The output of the 9.5 mm amplifier was 1.2 J when pumped with 200 J of electrical energy. The small signal gain was 20. Energy extraction was approximately 50%. This

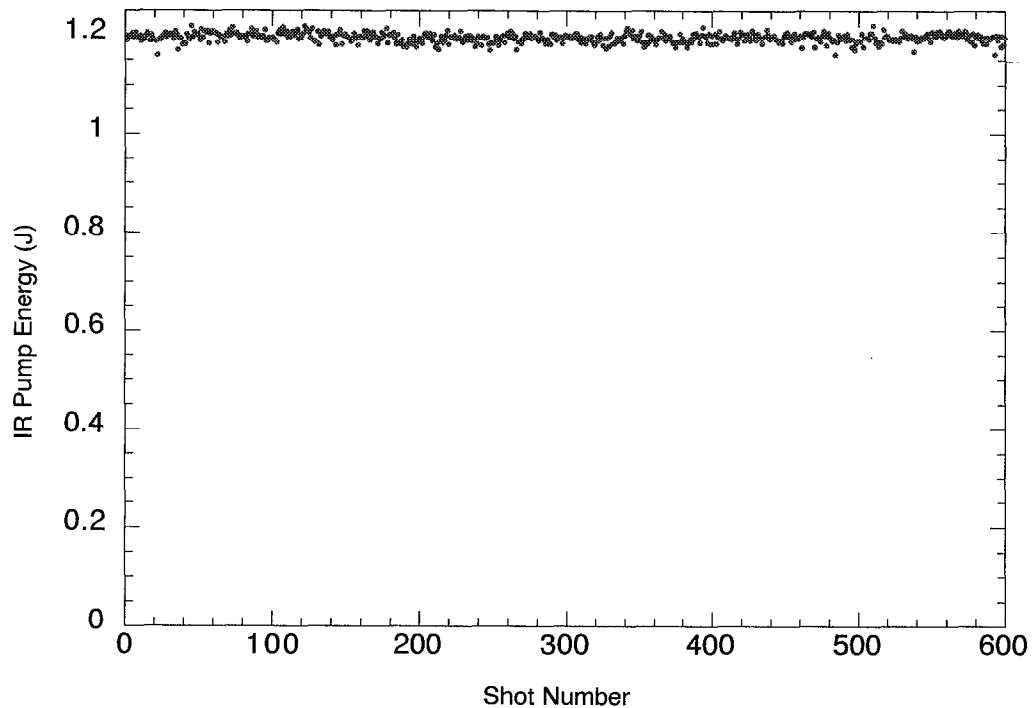


Figure 2.15: Stability of the 9.5 mm Nd:YLF amplifier.

amplifier is highly saturated, which acts to stabilize the energy output. This can be seen in Fig. 2.15. The stability is better than $\pm 1\%$ RMS.

The results of the model can be seen in Fig. 2.16. The output energy is plotted as a function of input energy. The model is in excellent agreement with the measured values. The parameter 2^* was adjusted to 1.5, which produced the best fit.

Second Harmonic Generation

To obtain the proper frequency to pump Ti:sapphire the infrared light must be frequency doubled. This was accomplished using a 12 mm \times 30 mm piece of KD*P cut for Type II doubling. The crystal, from Cleveland Crystals, is mounted in a hermetically sealed, temperature controlled housing to prevent both crystal degradation due to water absorption and any detuning of the phase matching angle due to changes in temperature.

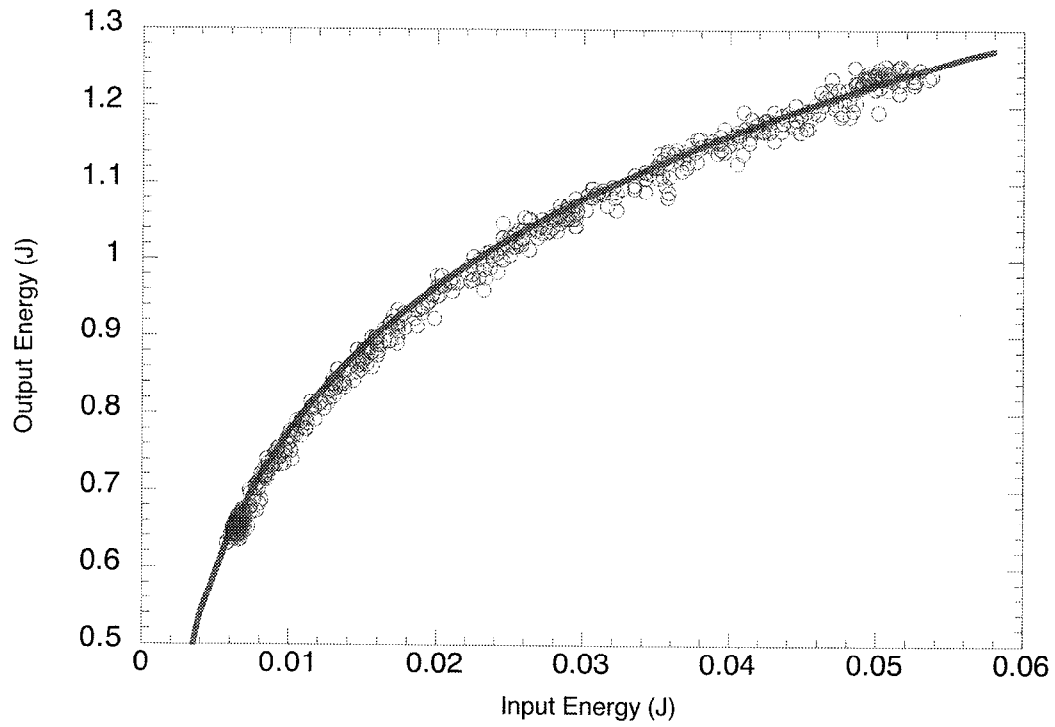


Figure 2.16: Output of the 9.5 mm Nd:YLF amplifier. The solid line is the results of a calculation.

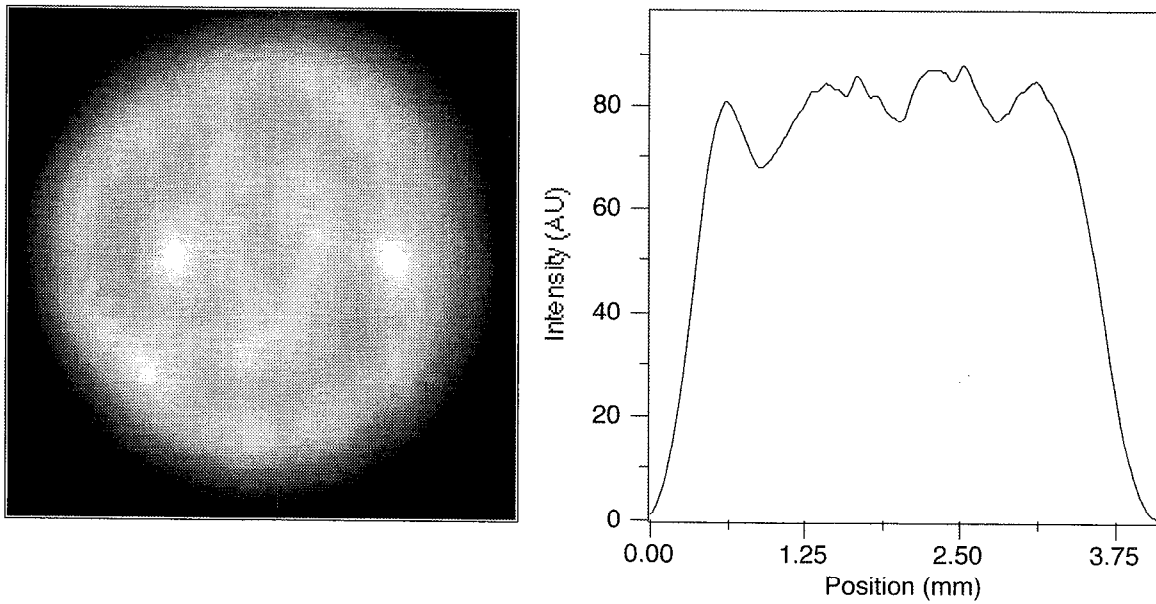


Figure 2.17: Profile of IR beam at the doubling crystal.

Before the crystal, the beam is passed through a telescope to decrease the beam size, increasing the intensity. The IR beam at the crystal face is shown in Fig. 2.17. The beam profile is a flat top with 10% modulation.

The conversion of the fundamental to second harmonic light is shown in Fig. 2.18. At maximum energy we produce 650 mJ of second harmonic light. The maximum conversion efficiency is approximately 55%. The solid line represents a model calculation from Banks.²⁸ This code numerically solves the coupled wave equations describing this process in all four dimensions (3 spatial plus time). At low energy the model agrees well with these data. At higher energies the code overestimates the second harmonic output. This may be due to phase modulation on the pulse.²⁸ The profile of the second harmonic beam at the plane of the second 4 pass amplifier Ti:sapphire crystal is shown in Fig. 2.19.

2.3.2 High power 4 pass Ti:sapphire power amplifier

The layout of the second 4 pass amplifier is shown in Fig. 2.20. This amplifier uses a bowtie design where the beam is passed through the crystal twice, and then reflected over the same path for the third and fourth pass. There is a Pockels cell at the entrance of the amplifier which switches the pulse into the amplifier. Whenever possible, the polarizers are used in reflection which maximized bandwidth for these polarizers.

This bowtie design was chosen to minimize the path length in the amplifier. The path length in this amplifier is significantly less than in the first 4 pass. The beam now has a flat top spatial profile which must be relayed through the system. The long image and object distances lead to long focal length telescopes. Due to limited space, one wants to keep the telescopes, and therefore the amplifiers, as short as possible. This amplifier has a path length of 3.2 m compared to over 8 m for the first 4 pass.

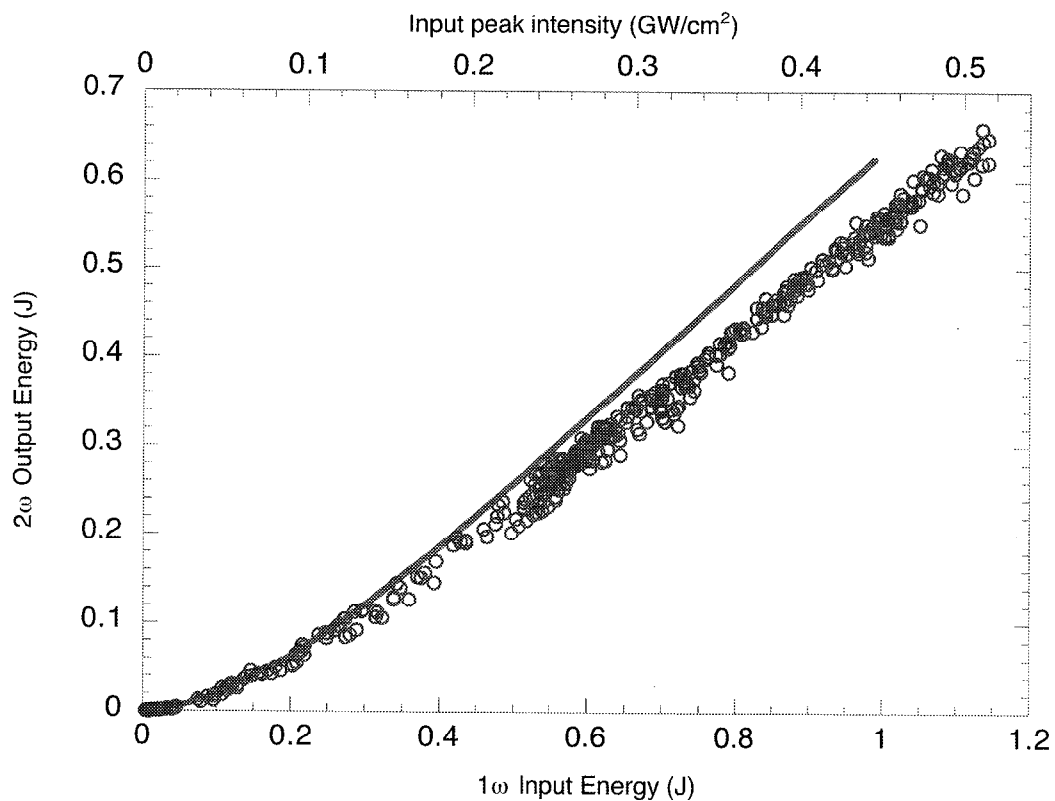


Figure 2.18: Second harmonic conversion of the 9.5 mm amplifier energy. The solid line is from a model calculation

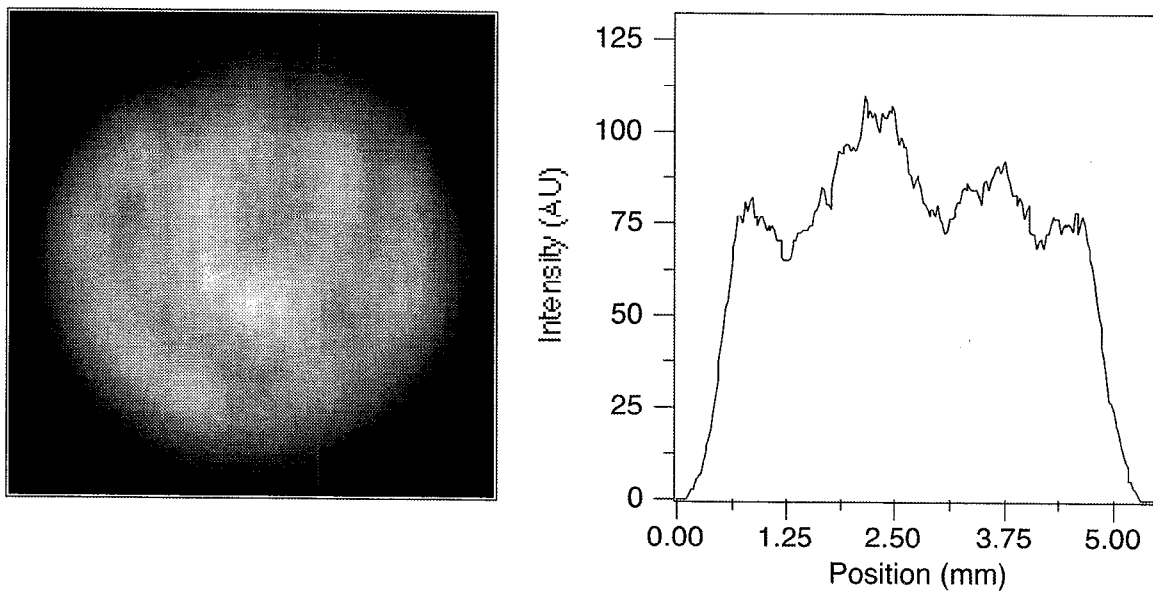


Figure 2.19: Profile of the second harmonic beam. The profile is taken at the plane of the amplifier crystal.

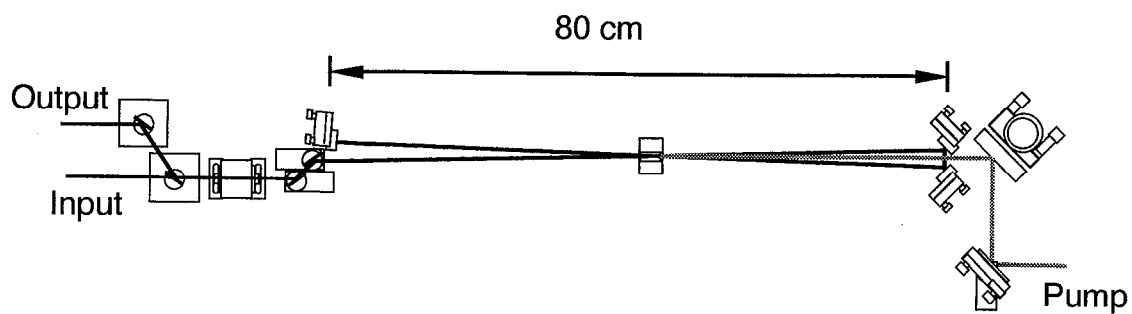


Figure 2.20: Layout of second 4 pass amplifier.

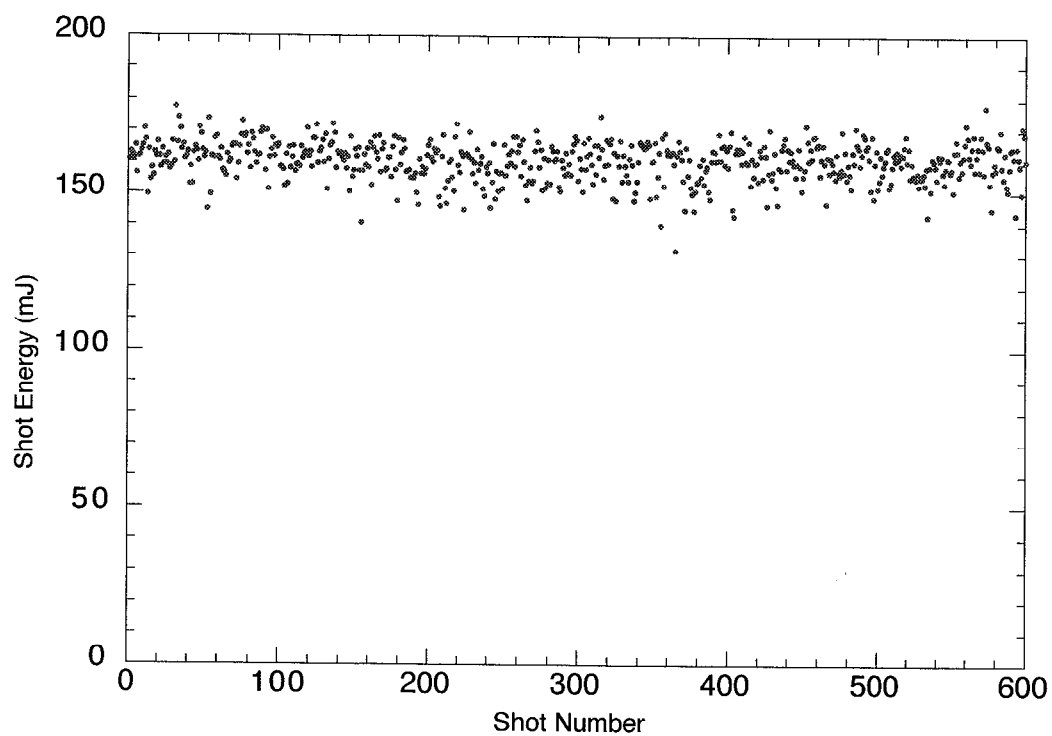


Figure 2.21: Stability of second 4 pass amplifier.

The maximum output of the amplifier was 175 mJ. This was achieved running the first 4 pass at 50 mJ. This damaged some of the transport optics between the two amplifiers and the first 4 pass had to be turned down to 40 mJ. The results of a stability measurement is shown in Fig. 2.21. This shows an average energy of 160 mJ and an RMS deviation of $\pm 4\%$.

2.4 High power back end

Originally this laser system was designed to produce over 5 J of energy. This would require two more stages of amplification in Ti:sapphire. After the second 4 pass amplifier, there would have been a Pockels cell which would have switched a pulse at a 1 Hz repetition rate to these back end amplifiers. This reduced repetition rate was due to the capabilities of the pump system associated with the back end. This also would have allowed simultaneous experiments to be done. Nine pulses in every ten would go to a small pulse compressor in air which can handle up to 200 mJ, with the other pulse being amplified further in the laser back end before going to a vacuum pulse compressor.

The pump system for the back end was mentioned in section 2.3.1. The Ti:sapphire amplifiers were to consist of a 20 mm diameter, 3 pass amplifier and a 30 mm diameter, 2 pass amplifier. The first of these was designed to produce 1.5 J at 1 Hz, and the second would produce over 5 J every 8 min. After this, the beam would be transported to a pulse compressor inside a large vacuum chamber. At these high intensities (5 J at 50 fs would be 100 TW), it is necessary to compress the pulse in vacuum to prevent a massive accumulation of non-linear phase on the pulse.

This back end is being constructed (with minor modifications) as part of the new FALCON (Femtosecond Accelerator Concept) short pulse laser at LLNL.

2.5 Compressor

From the second 4 pass amplifier, the beam is expanded to 2.1 cm and relayed into a pulse compressor. We used a single grating design⁵³ seen in Fig. 2.22. The grating was 12" in diameter and 1480 l/mm. This compressor is easy to align since the grating pair is formed from a single grating and a retro-reflecting fold mirror, making grating misalignment impossible. Another advantage is that by changing only the position of the fold mirror, the length of the pulse can be adjusted.

The maximum output energy measured after the compressor was 50 mJ. This low compressor throughput is due to the many gold surfaces which the beam reflects off of inside of the compressor, many of which were in poor condition. Also, some clipping occurs on the optics, further diminishing throughput.

The single shot second-order autocorrelation of the compressed pulse is shown in Fig. 2.23. The crystal used was KD*P, 500 μm thick. The FWHM of the autocorrelation trace was 72 fs, which deconvolves to 50 fs. There are some low energy wings at the 5% level.

By scanning the delay leg in the second order autocorrelator we found some small pulses far from the main pulse. This autocorrelator is inherently symmetric. A third-order autocorrelation had to be performed in order to determine if these pulses came before or after the main pulse. We used a scanning third-order autocorrelation shown in Fig. 2.24. The first KD*P crystal is cut for second harmonic generation. The two frequencies are then split with a dichroic mirror. The second harmonic is sent down a variable delay leg before being recombined with the fundamental. These beams then pass through the second KD*P crystal, cut for sum frequency generation. The third harmonic is then separated using a fused silica prism. The beam is passed through a bandpass filter to remove scattered light and finally measured using a silicon based energy meter.

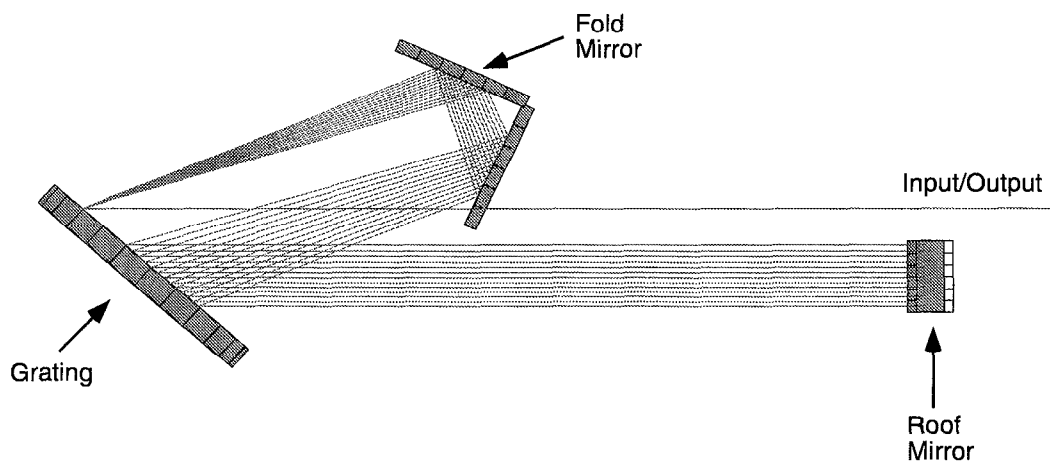


Figure 2.22: Layout of the single grating pulse compressor.

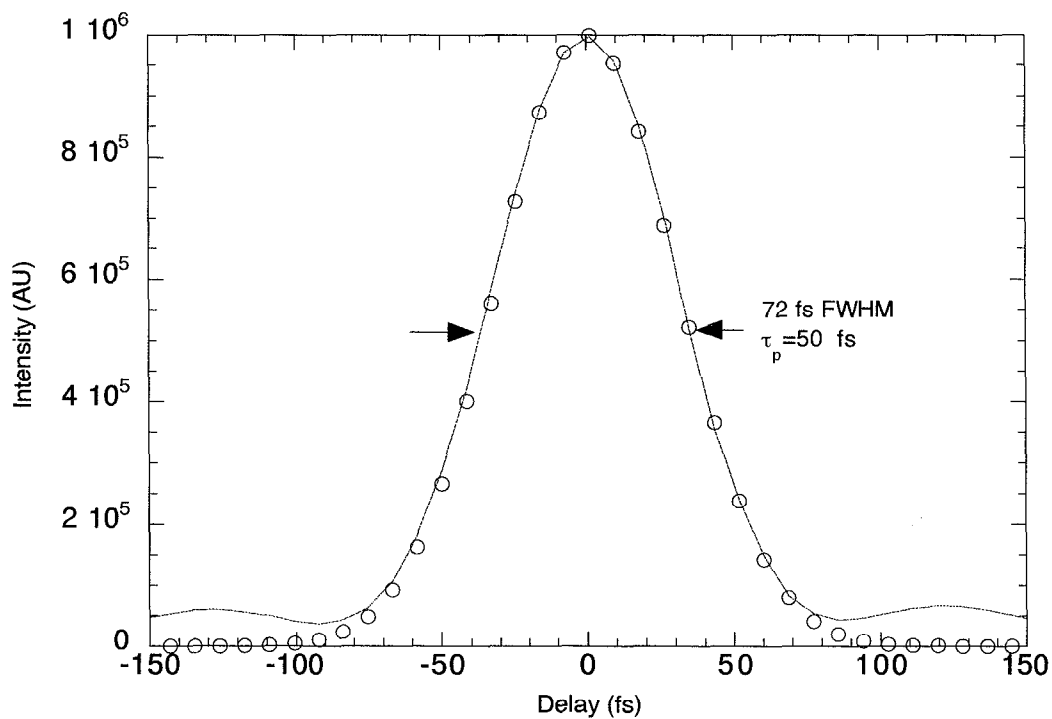


Figure 2.23: Second-order autocorrelation. The open circles are the calculated values for a 50fs gaussian pulse.

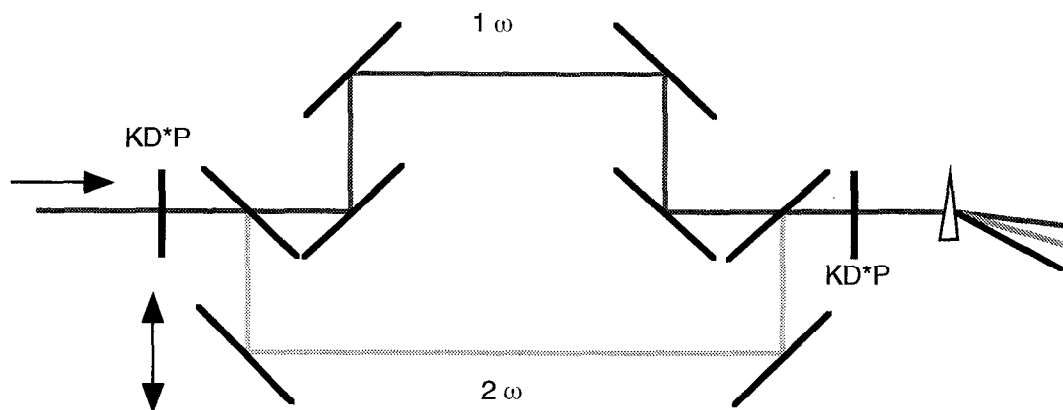


Figure 2.24: Scanning third-order autocorrelator.

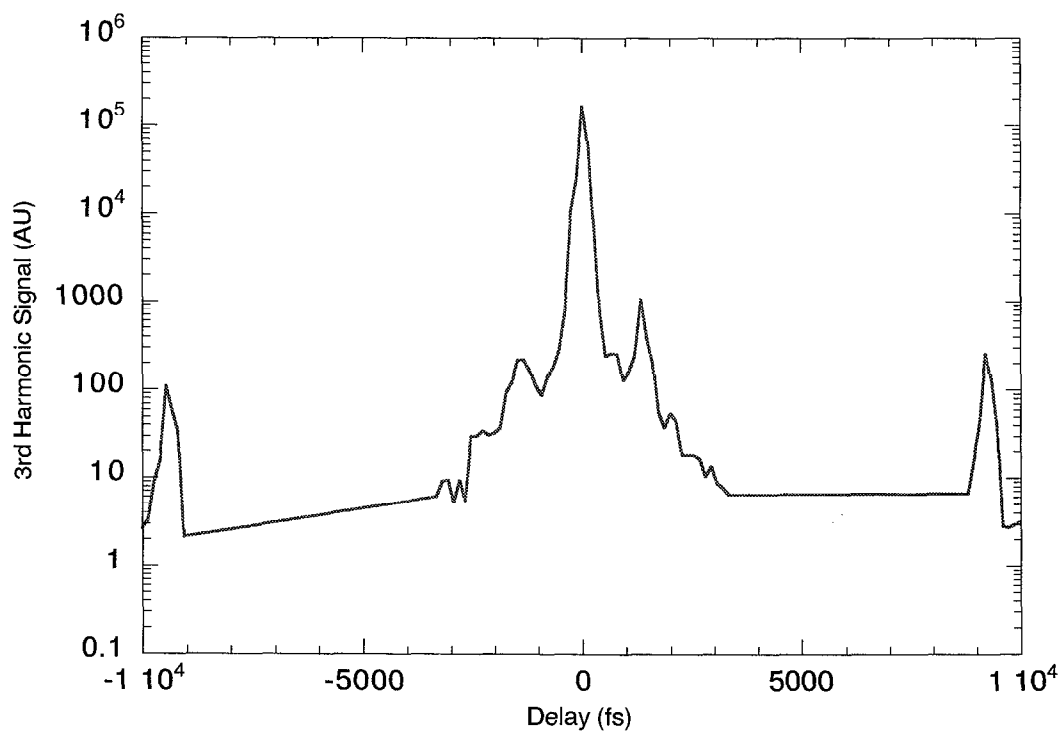


Figure 2.25: Third-order autocorrelation. Asymmetry of satellite pulses indicates that they are post-pulses.

Since this is a scanning method, it does not measure a single pulse, but rather the average of many pulses. The delay leg, which is the second harmonic in this case, is swept across the fundamental; the energy of the third harmonic is measured every $20\text{ }\mu\text{m}$. For our purpose negative delay is defined when the delay leg has less delay than the fundamental, and positive delay is defined when it has more.

Extra pulses will still produce features for both positive and negative delay in this autocorrelator. However, unlike a second order device, the features will be asymmetric. In our case, if the larger feature is for positive delay it indicates a post-pulse; if it is larger for negative delay it indicates a pre-pulse. The third order autocorrelation is shown in Fig. 2.25. The satellite features are larger for positive delay, showing that these are post-pulses, and therefore should not interfere with our experiments. Their origin is most likely reflections somewhere in the laser system.

2.6 19 mm Nd:YLF amplifier development

The 19 mm Nd:YLF amplifiers were supposed to provide energy to pump a 20 mm Ti:sapphire amplifier, and provide seed energy for a set of Nd:Glass amplifiers. Although this section of the laser was not built as part of this thesis, the 19 mm Nd:YLF amplifiers were designed, built, and tested. They are currently installed in the FALCON short pulse laser system at LLNL.

2.6.1 19 mm amplifier design

The design of these amplifiers drew heavily from a 45 mm Nd:Glass amplifier developed at LLNL for the petawatt laser.³² The amplifier is shown in Fig. 2.26. The main housing is made of stainless steel. The laser rod rests on two stainless steel plates (one on each

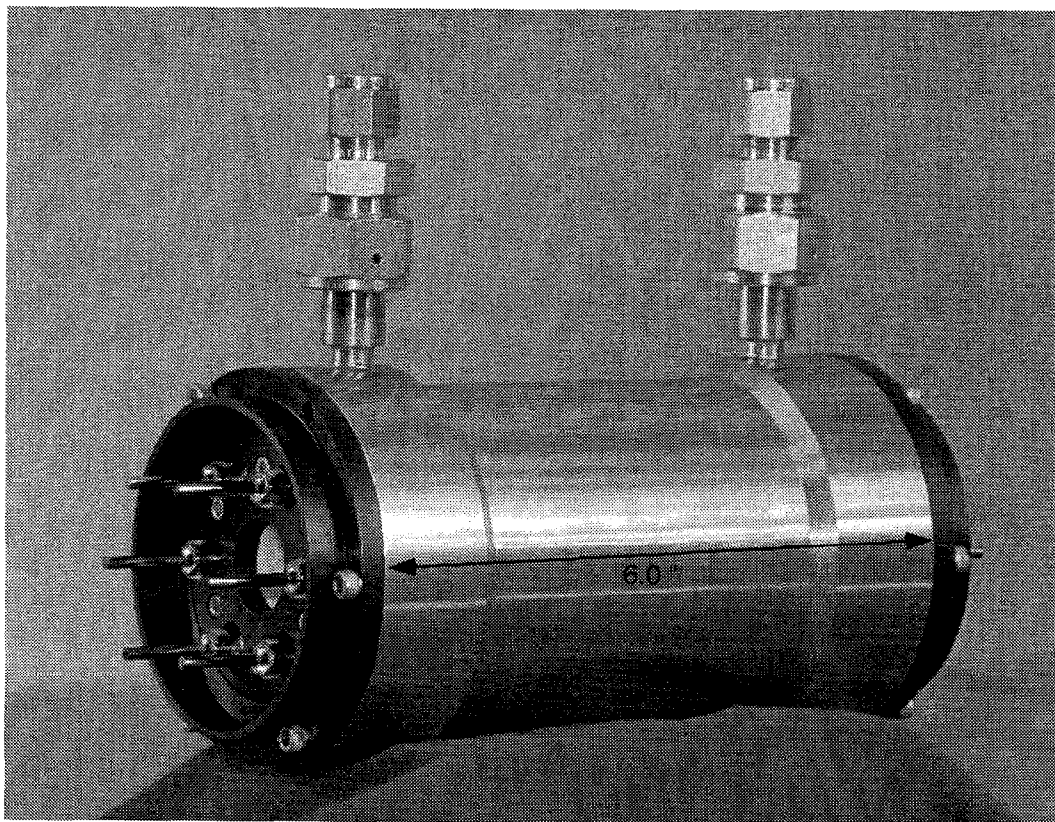


Figure 2.26: 19 mm Nd:YLF amplifier.

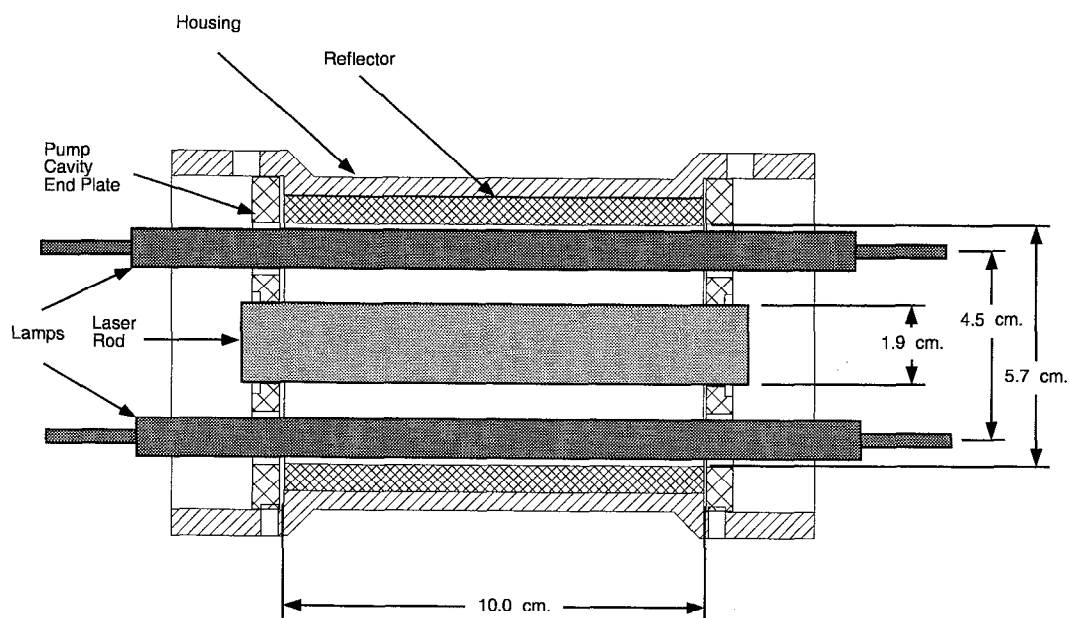


Figure 2.27: 19 mm Nd:YLF amplifier head cutaway view.

side) which slide into the housing. The endcaps are made out of the thermoplastic, Ultem. Thin ceramic sleeves are inserted into the aperture to protect the plastic from the flashlamp light. A cutaway view of the inside of the head can be seen in Fig. 2.27. There is a diffuse cylindrical reflector inside of the housing made out of Spectralon. This material, made by Labsphere, is a thermoplastic resin which can be easily machined. At the flashlamp wavelengths, the reflectance is almost 99%. This material will damage before a ceramic reflector would, but we are operating below its damage threshold. The xenon flashlamps have a 10 cm arc length and 7 mm bore. The rod is 19 mm in diameter and 12 cm in length (10 cm inside of the pump cavity). Water is flowed through the entire central housing for cooling; the surfaces of the rod, lamps, and reflector are all “wet”.

Based on our gain measurements of the 9.5 mm Nd:YLF amplifiers, we found that we needed near 1 kJ of energy for the flashlamps to achieve the required gain. With an array of 6 lamps, each lamp would run at about 12% explosion fraction. This should give a lifetime of well over 30 million shots (at 1 Hz this would be over 4 years). These lamps are run well below their explosion energy and conceivably only 4 lamps are needed. The 6 lamp design, however, offers better pumping uniformity and leaves room to boost the pump energy if we were to build a larger pulse-forming network (PFN).

We also developed a new PFN for this amplifier. It uses 210 μF of capacitance which can be charged up to 3 kV. The lamps are broken down by a 12 kV trigger pulse, after which the main capacitor bank discharges. The pulse width is 280 μs .

2.6.2 19 mm amplifier performance

The amplifier was tested using the seed from the front end of the Nd:YLF pump system described in section 2.3.1. Pyroelectric energy meters were used to make all the measure-

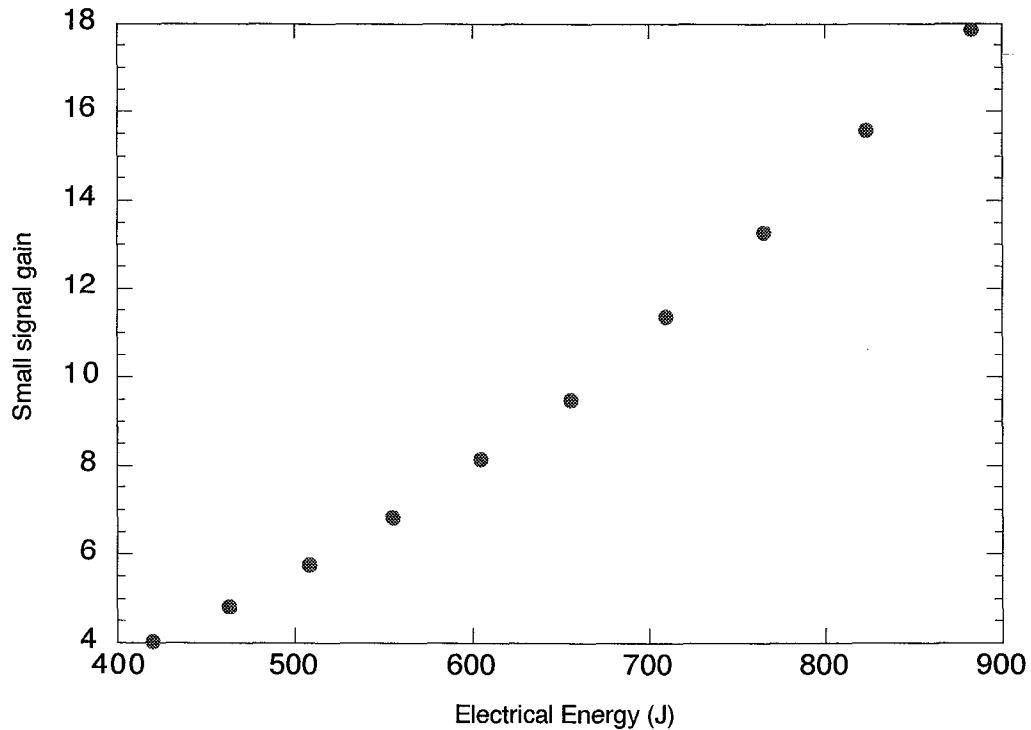


Figure 2.28: Small signal gain in the 19 mm amplifier.

ments. The input beam into the amplifier was reflected off a beam splitter. The transmitted energy was measured as a reference, and calibrated to the input energy. A LabView data acquisition system collected both input and output energy from the amplifier over many shots.

Using a 16 mm beam with about 1 mJ of energy the small signal gain can be measured. The results are shown in Fig. 2.28. Even at the highest electrical energies we see increasing gain, indicating we are not saturating the inversion and could continue to increase the small signal gain beyond 20 if we had more electrical energy.

When we measure the small signal gain of the amplifier, we are taking an average of the gain across the rod. The pump energy will be depleted as it propagates inward from the outside of the rod.⁵⁴ This will cause the inversion to be larger on the edges of the rod

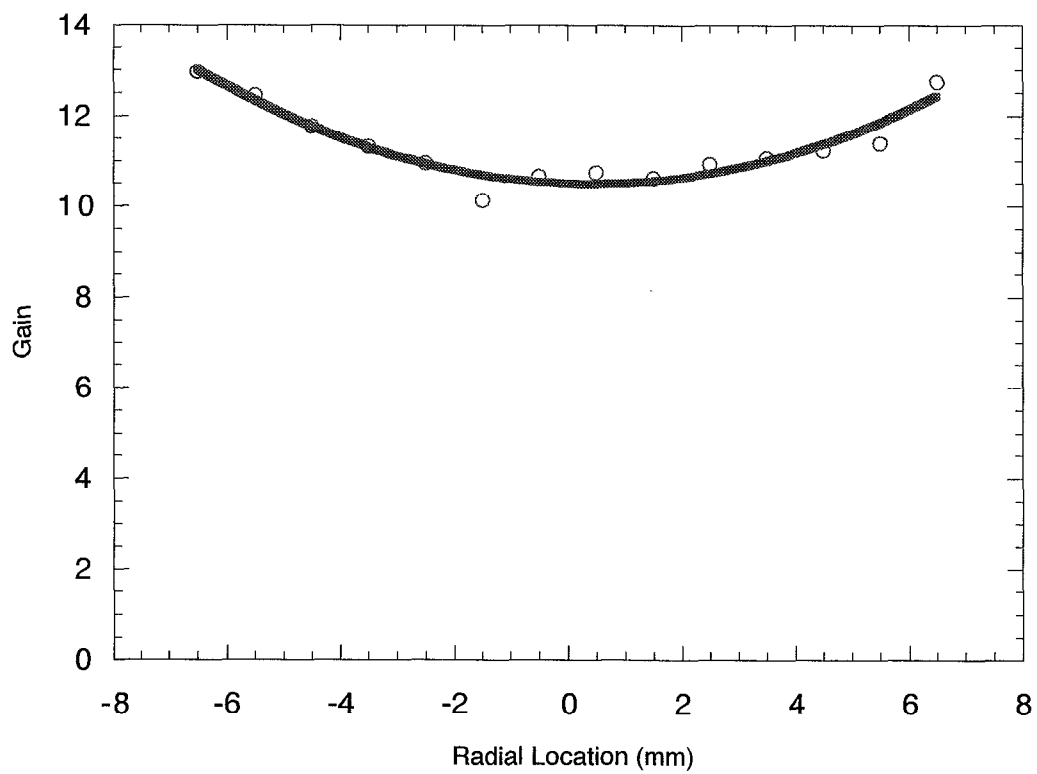


Figure 2.29: Radial gain profile in the 19 mm amplifier. The line is a parabolic fit to the data.

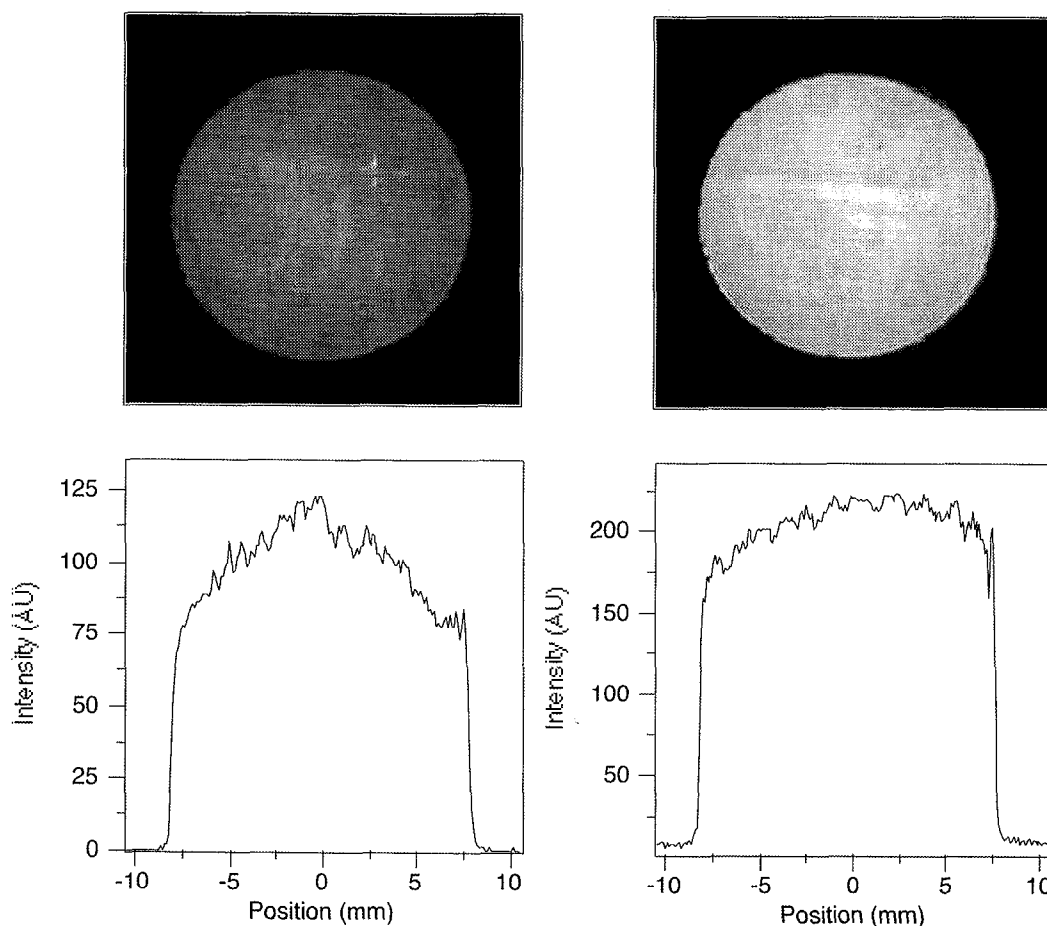


Figure 2.30: 19 mm amplifier beam profiles. The left image shows the unamplified seed and the right image is after amplification. The scales on the two lineouts are different.

compared to the middle. To mitigate this problem we had the Nd:YLF rods doped at the .5% level as opposed to the standard 1%. The radial gain profile is shown in Fig.2.29. This was taken with 710 J of electrical energy, which gave an average small signal gain of 12. The gain is reasonably uniform across the rod.

This dependence of gain on radius will help up to achieve a flat top profile for the output beam. The input beam, shown in Fig. 2.30 is a clipped gaussian beam. The output will be the convolution of the input profile and the gain profile. When you compare the two beams in Fig. 2.30, one can see that the output beam is much closer to a true flat top than the input. Something else to note in these images is the horizontal lines just slightly above

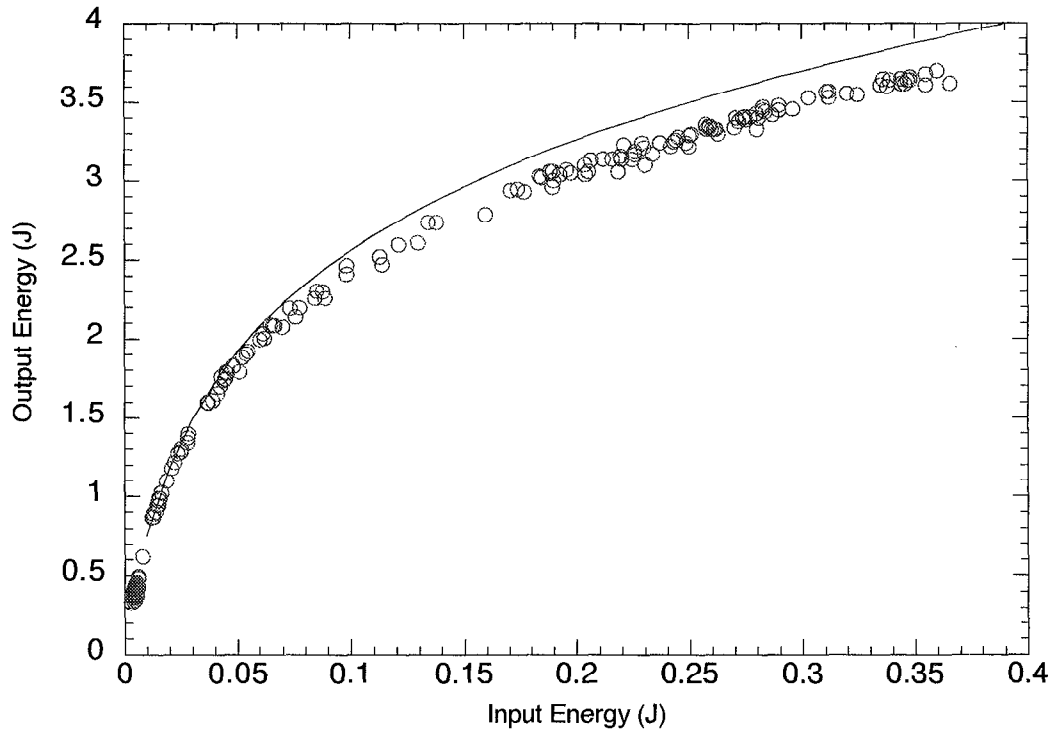


Figure 2.31: Saturated gain in the 19 mm amplifier. The line represents a Frantz-Nodvick model.

the center of the rod. These are from aberrations in the rod itself. The modulation is low, but it shows the difficulty of producing high quality, large aperture Nd:YLF rods.

With this preliminary data we can investigate the saturated gain performance of the amplifier. The same setup was used here as was used to measure the small signal gain, except a high damage threshold pyroelectric detector was used to measure the output energy. The results are shown in Fig. 2.31. These data were taken using 710 J of electrical energy. The model, described earlier, predicts the energy for small input energies accurately. At higher energies it over-predicts the output energy by about 5%. This is most likely due to deviations of the actual beam profile from an ideal flat top.

This amplifier is heavy saturated and that leads to good energy stability. The output stability is shown in Fig. 2.32. Overall the stability is better than $\pm 4\%$ RMS. There are several data points which are well below the average energy. These are not from instabilities

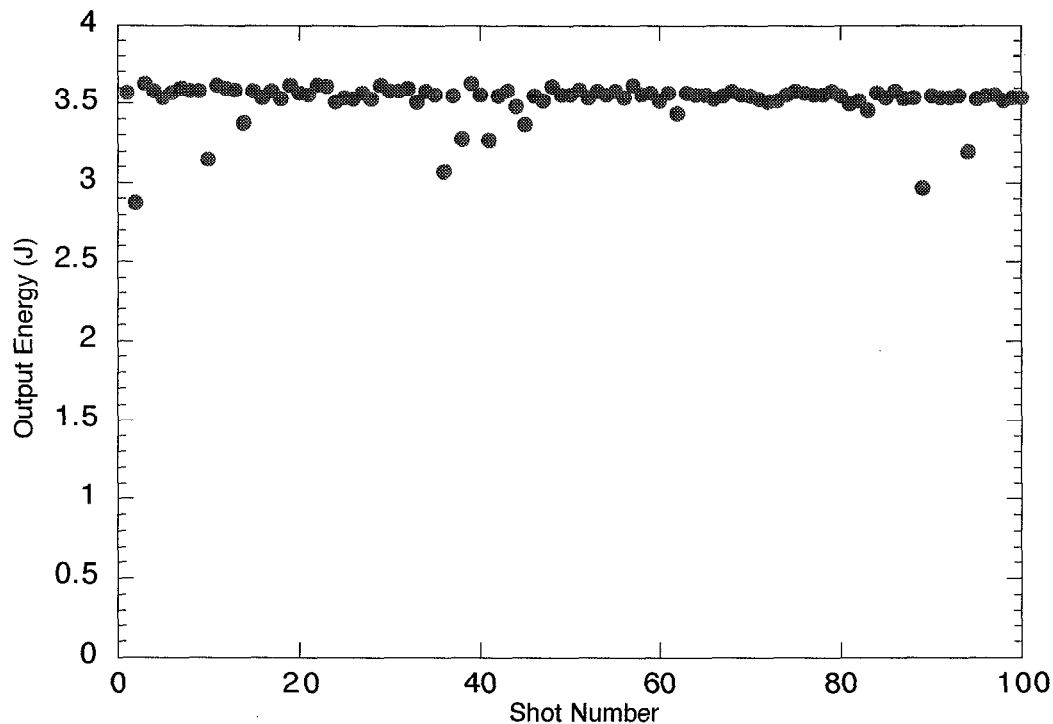


Figure 2.32: Energy stability of the 19 mm amplifier.

of the 19 mm amplifier, but rather from changes in the seed energy. In these shots the seed energy is down by as much as 40%. These shots are accompanied by a loud snapping noise as either dust gets into the beam, or pointing instabilities lead to the beam missing a pinhole. If we remove these points, the stability is better than $\pm 2\%$ RMS.

2.6.3 Second harmonic conversion of 19 mm amplifier

Second harmonic generation in the 19 mm amplifiers is done with a 4 cm long piece of KD*P cut for Type I phase matching. The crystal is from Cleveland Crystals and is mounted in a hermetically sealed housing with sol-gel coated windows. The beam diameter is reduced from 16 mm to 8 mm before the crystal. This increases the peak intensity to about .4 GW/cm², improving conversion efficiency.

The conversion efficiency is shown in Fig. 2.33. We have a conversion efficiency slightly

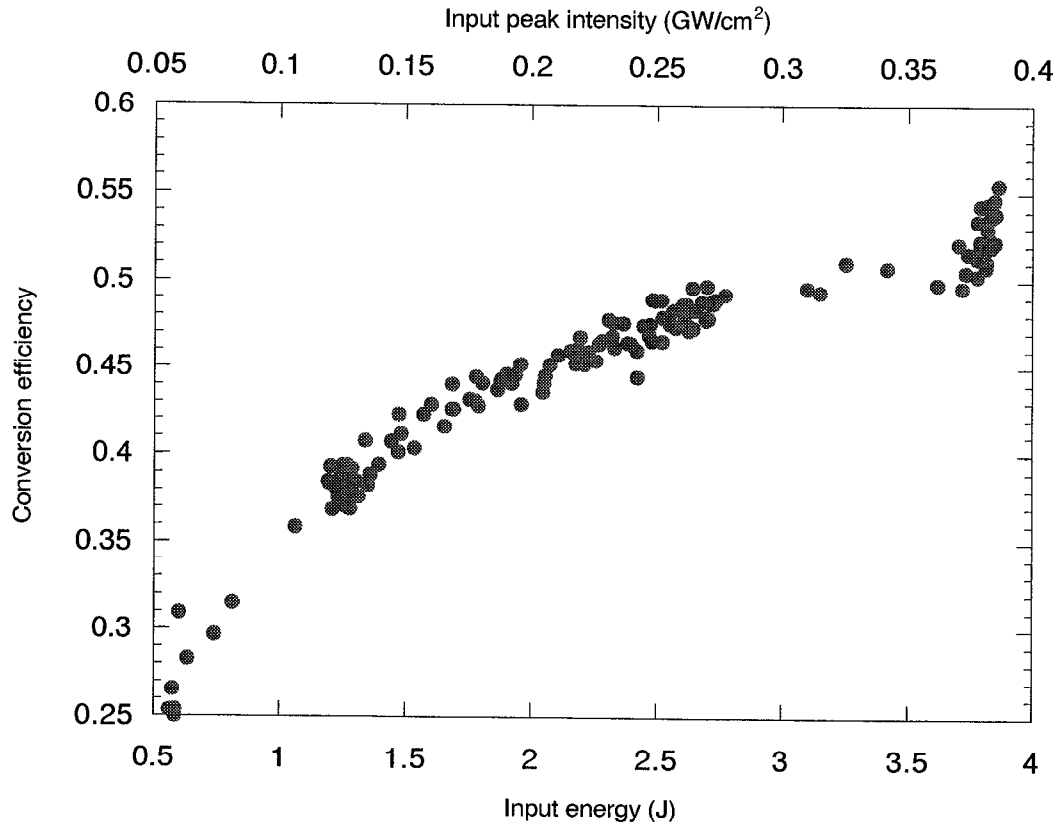


Figure 2.33: Second harmonic conversion of the 19 mm amplifier. The large spread at the maximum energy is caused by thermal detuning.

over 50% at the maximum energy. This corresponds to about 2 J of second harmonic energy. There is no temperature control in these crystals, so as energy is absorbed by the crystal there is some thermal detuning. This accounts for the large spread in conversion efficiency at the maximum energy.

2.7 Conclusion

In this chapter we have examined the design of a terawatt class, 50 fs Ti:sapphire laser system. While designed to produce 100 TW of peak power, the system was only constructed up to the 1 TW level. This will provide a source with more than enough intensity to performed the experiments in this thesis. The designs for the high power amplifiers, while not used in this laser, have been incorporated into the new FALCON laser system at LLNL.

Chapter 3

Theory of laser-cluster interactions

As discussed in the introduction, the high field community did not start looking into interactions with atomic clusters until the early 1990's. Several theories were discussed in the introduction, and there has been a great deal of disagreement over the correct interpretation. The plasma model of Ditmire *et al.*²² has met with some success in modeling many experimental results.²⁴ However, there have not been any time-resolved measurements on the femtosecond scale to support the predicted dynamics. The purpose of the experiments to be discussed in the chapters 4 and 5 was to get experimental evidence for this theory. In this chapter, this model is introduced and expanded.

3.1 Ionization

The first process which we consider is ionization. The laser field will ionize the cluster atoms, creating the initial free electrons. Once free, these electrons will go on to create further ionization through collisions. This collisional process will dominate the ionization and produce much higher charge states than optical ionization alone; this is a major difference between clusters and a pure gas.

3.1.1 Optical field ionization

Optical field ionization (OFI) is generally divided into two regimes: the tunneling regime and the multiphoton regime. The Keldysh³ parameter, γ , is used to quantitatively differentiate between these regimes. γ is defined as

$$\gamma = \left(\frac{I_p}{2U_p} \right)^{1/2}, \quad (3.1)$$

where I_p is the ionization potential of the atom and U_p , the pondermotive potential of the laser, can be written

$$U_p(eV) = \frac{e^2 \mathcal{E}_0^2}{4m_e \omega^2} = 9.33 \times 10^{-14} I(W/cm^2) \lambda^2(\mu m). \quad (3.2)$$

$\gamma > 1$ indicates the multiphoton regimes, while $\gamma < 1$ for the tunneling regime. For the first ionization stage of xenon ($I_p = 12.13eV$), $\gamma = 1$ when the intensity is 9.6×10^{13} . For the tenth ionization stage ($I_p = 206eV$), $\gamma = 1$ when the intensity is 1.6×10^{15} . So for our experiments, which take place in the $10^{16} - 10^{17}$ range, we can expect the ionization to be dominated by tunnel ionization.

Tunneling rates are generally calculated using the rate equation of Ammosov, Delone, and Krařnov⁵⁵. This so called ADK rate, W_{tun} , is

$$W_{tun} = \omega_a \frac{(2l+1)(l+|m|)!}{2^{|m|}|m|!(l-|m|)!} \left(\frac{2e}{n^*} \right)^{2n^*} \frac{1}{2\pi n^*} I_p \left(\frac{2\mathcal{E}}{\pi(2I_p)^{3/2}} \right)^{1/2} \\ \times \left[\frac{2}{\mathcal{E}} (2I_p)^{3/2} \right]^{2n^*-|m|-1} \exp \left[-\frac{2}{3\mathcal{E}} (2I_p)^{3/2} \right], \quad (3.3)$$

where ω_a is the atomic unit of frequency ($= 4.134 \times 10^{16} s^{-1}$), \mathcal{E} is the laser electric field in atomic units, l and m are the angular momentum and magnetic quantum numbers (the rate is averaged over m for a given l), n^* is the effective principle quantum number ($n^* = \sqrt{27.2Z[2I_p(eV)]^{-1/2}}$), and e is the base of the natural logarithm.

3.1.2 Collisional ionization

OFI will occur in both clusters and a pure gas. In a gas the density is low and OFI fully describes the ionization process. The high density inside of a cluster allows the free electrons to further ionize other ions through collisions, greatly increasing the level of ionization in the plasma. Both thermal electrons and electrons driven by the pondermotive force will contribute to collisional ionization.

To calculate the collisional ionization rates we will be using the empirical ionization cross-section of Lotz⁵⁶

$$\sigma_i = a_i q_i \frac{\ln(K_e/I_p)}{K_e I_p}, \quad (3.4)$$

where a_i is an experimentally determined constant, $4.5 \times 10^{-14} \text{ cm}^2(\text{eV})^2$, q_i is the number of electrons in the outer shell, and K_e is the kinetic energy of the electron. The rate of ionization averaged over all collision energies will simply be

$$W = n_e \bar{\sigma}_i \bar{v} \quad (3.5)$$

For ionization by thermal electrons we start with a Maxwellian distribution

$$\frac{dn}{n} = \frac{2}{kT} \left(\frac{K_e}{\pi kT} \right)^{1/2} \exp(-K_e/kT) dK_e, \quad (3.6)$$

where T is the plasma temperature and k is Boltzmann's constant. Using Eq. 3.4 and the distribution, Eq. 3.5 becomes

$$W_{kT} = n_e \int_{I_p}^{\infty} \frac{2}{kT} \left(\frac{K_e}{\pi kT} \right)^{1/2} \exp(-K_e/kT) dK_e a_i q_i \frac{\ln(K_e/I_p)}{K_e I_p} \left(\frac{2K_e}{m} \right)^{1/2} \quad (3.7)$$

The lower limit of integration is the ionization potential since there will not be an ionization event if the energy is below this level. Performing the integration⁵⁷ we get the thermal electron collisional ionization rate per ion (s^{-1}),

$$W_{kT} = n_e 6.7 \times 10^{-7} \frac{a_i q_i}{(kT)^{1/2} I_p} \int_{I_p/kT}^{\infty} \frac{e^{-x}}{x} dx \quad (3.8)$$

where a_i is given in $10^{-14} \text{ cm}^2(\text{eV})^2$ and I_p and kT are in eV. The integral here is the standard exponential integral and can be easily calculated.

The other contribution to collisional ionization will come from collisions with electrons driven by the electric field of the the laser. These electrons have a characteristic energy equal to the pondermotive energy, U_p (Eq. 3.2).

We will again use the cross-section of Lotz (Eq. 3.4) but now we will average over the kinetic energy of the electron in the laser field. The velocity of the electron can be written as

$$v = \frac{e\mathcal{E}_0}{m_e\omega} |\sin \omega t| \quad (3.9)$$

This makes the cycle averaged ionization rate

$$W_{las} = \frac{2n_e}{\pi} \int_{\phi_{min}}^{\frac{\pi}{2}} \sigma_i \frac{e\mathcal{E}_0}{m_e\omega} \sin \phi d\phi \quad (3.10)$$

where ϕ_{min} is the phase where the kinetic energy of the electron is equal to the ionization potential of the ion. Noting that $K_e = 2U_p \sin^2 \phi$ we can write

$$\sin \phi d\phi = \frac{dK_e}{4U_p \sqrt{1 - K_e/2U_p}} \quad (3.11)$$

Substituting this into Eq. 3.10 and using Eq. 3.4 yields the ionization rate

$$W_{las} = n_e \frac{a_i q_i}{\pi I_p} \left(\frac{1}{m_e U_p} \right)^{1/2} \int_{I_p}^{2U_p} \frac{\ln(K_e/I_p)}{2K_e} \frac{1}{\sqrt{1 - K_e/2U_p}} dK_e. \quad (3.12)$$

This integral would have to be evaluated numerically. We know that the ionization rates will be largest when the electron energy is near the ionization potential. Hence, if we only look at kinetic energies around I_p , we can expand the logarithm in Eq. 3.12 about $1 - I_p/K_e$ and obtain

$$W_{las} \approx \frac{a_i n_e q}{2\pi m_e^{1/2} I_p U_p^{1/2}} \left[\left(3 - \frac{I_p}{U_p} + \frac{3}{32} \left(\frac{I_p}{U_p} \right)^2 \right) \ln \left| \frac{1 + \sqrt{1 - I_p/2U_p}}{1 - \sqrt{1 - I_p/2U_p}} \right| - \left(\frac{7}{2} - \frac{3}{8} \frac{I_p}{U_p} \right) \sqrt{1 - I_p/2U_p} \right]. \quad (3.13)$$

Note that this corrects a sign error in previous publications.²²

The total ionization rate will be determined by the summation of Eqs. 3.3, 3.8, and 3.13.

3.2 Heating mechanisms

3.2.1 Above threshold ionization

As the electrons are ionized by the optical field they will gain energy from the laser. This process, called above threshold ionization (ATI)⁵⁸ occurs in both gases and clusters. First observed by Agostini *et al.*⁵⁹ ATI allows density independent heating of the plasma.

Quasi-classically,⁶⁰ we can think of ATI as a result of ionization occurring when the electric field is not at a maximum. An electron is ionized at essentially zero velocity. Once free, the electron will oscillate in the electric field. If it was ionized at the peak, where the probability for ionization is highest, the velocity will still be zero after the laser passes. However, if it is ionized at a phase, $\delta\phi$, from the field maximum, the electron will have a residual velocity after the laser pulse. The energy associated with this, per electron, is⁶⁰

$$K_e = 2U_p \sin \delta\phi. \quad (3.14)$$

This will be small for the majority of electrons. The total energy transferred to the plasma is small and an ATI heated plasma will have a temperature in the tens of eV.

3.2.2 Inverse bremsstrahlung heating

Although the pondermotive energy of an electron in the laser field is large, this energy cannot directly be transferred to the electron. A third body, usually an ion, is needed since momentum and energy cannot both be conserved in a photon-electron interaction. This process is known as inverse bremsstrahlung (IB).

Pure gas targets have low densities and low collision rates. Hence, we expect IB to play little role in heating. In solid targets, on the other hand, IB plays a major role in plasma heating. Clusters, having solid density, will see IB dominate the heating.

A simple way to bring IB heating into the calculation is through the use of a Drude model for the complex dielectric constant,

$$\epsilon = 1 - \frac{\omega_p^2}{\omega(\omega + i\nu)}. \quad (3.15)$$

where ν is the electron-ion collisional frequency and w_p is the plasma frequency ($w_p^2 = 4\pi n_e e^2 / m_e$). This treats the cluster as a small plasma. The collisional frequency is responsible for the imaginary part of the dielectric constant (and therefore the absorption). Its exact value is difficult to measure experimentally and we will estimate it with the formulas of Silin⁶¹

$$\nu = \frac{4}{9} \left(\frac{2\pi}{3} \right)^{1/2} \frac{Z^2 e^4 n_i}{m_e^{1/2} (kT_e)^{3/2}} \ln \Lambda, \quad v_{osc} < v_{kT} \quad (3.16)$$

$$\nu = \frac{16Z^2 e n_i m_e \omega^3}{E_0^3} \left(\ln \left[\frac{eE_0}{2\omega(3m_e kT_e)^{1/2}} \right] + 1 \right) \ln \Lambda, \quad v_{osc} > v_{kT} \quad (3.17)$$

where v_{osc} is the oscillatory velocity of the electron from the laser field, v_{kT} is the average electron thermal velocity, and $\ln \Lambda$ is the standard Coulomb logarithm.

We can calculate the heating inside of a cluster by looking at the cycle averaged energy deposited by the field.⁶² The time rate of change of the electromagnetic energy inside of the cluster is the divergence of the Poynting vector

$$\frac{\partial U}{\partial t} = \nabla \cdot \mathbf{S} = \frac{c}{4\pi} \nabla \cdot (\mathbf{E} \times \mathbf{H}). \quad (3.18)$$

Using Maxwell's equations

$$\nabla \times \mathbf{E} = -\frac{1}{c} \frac{d\mathbf{B}}{dt}, \quad (3.19)$$

$$\nabla \times \mathbf{H} = \frac{c}{4\pi} \frac{d\mathbf{E}}{dt}, \quad (3.20)$$

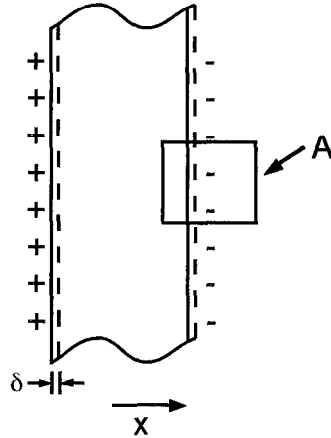


Figure 3.1: Idealized thin semi-infinite plasma used to calculate the natural frequency.

where ϵ is the complex dielectric constant, we can write

$$-\frac{\partial U}{\partial t} = \frac{1}{4\pi} \left(\epsilon \mathbf{E} \cdot \frac{d\mathbf{E}}{dt} + \mathbf{H} \cdot \frac{d\mathbf{B}}{dt} \right) \quad (3.21)$$

Taking the fields in the form $\mathbf{E} = \frac{1}{2}(\mathbf{E}e^{-i\omega t} + \mathbf{E}^*e^{i\omega t})$, and assuming a non-magnetic material ($\mu = 1$), the heating rate, per unit volume, can be written as,

$$\frac{\partial U}{\partial t} = \frac{\omega}{8\pi} \text{Im}[\epsilon] |E|^2, \quad (3.22)$$

where E is the peak amplitude of the laser field inside of the cluster. We see here that is it only the imaginary part of the dielectric constant that leads to absorption of this nature. Also important is the fact that the electric field will be modified inside of the cluster, or any material for that matter. As we will shall see, the field inside can actually become many times larger than the field on the outside.

3.2.3 Resonance in cartesian geometry

A plasma will have a natural frequency at which it will oscillate. When we drive the plasma at this frequency we will excite a resonance. For a bounded plasma, the dipole created

from the offset of the electron and ion fluid can couple to the driving field, enhancing the internal electric field. The frequency will be dependent on the plasma parameters as well as the boundary conditions of the plasma. We will first look at the case for a very thin, semi-infinite plasma.

Due to its large mass, we consider the ion fluid a stationary background of positive charge. We imagine pulling on the electron fluid in our plasma a small distance δ . This will offset the charge as seen in Fig. 3.1. When we release the electron fluid there will be a force acting to restore the plasma to its original state.

We calculate the field inside of the plasma with Gauss's law,

$$\oint_S \mathbf{E} \cdot d\mathbf{a} = 4\pi \int_V \rho dv. \quad (3.23)$$

Integrating over the closed surface (perimeter of area A) as shown in Fig. 3.1, we obtain

$$\mathbf{E} = 4\pi n_e e \delta \hat{\mathbf{x}}, \quad (3.24)$$

where n_e is the electron density. The force exerted on the plasma will be

$$\mathbf{F} = q\mathbf{E} = -4\pi e^2 n_e \delta \hat{\mathbf{x}}. \quad (3.25)$$

The equation of motion in the $\hat{\mathbf{x}}$ direction is

$$\frac{d^2 \delta}{dt^2} m_e = F = -m_e \omega_p^2 \delta, \quad \omega_p^2 \equiv \frac{4\pi n_e e^2}{m_e}. \quad (3.26)$$

This leads to the differential equation

$$\frac{d^2 \delta}{dt^2} + \omega_p^2 \delta = 0. \quad (3.27)$$

This is the equation of a simple harmonic oscillator with frequency

$$\omega = \omega_p. \quad (3.28)$$

ω_p is the well known plasma frequency, which can be defined as the resonant frequency of a plasma of this nature.

Now we can look at how an external electric field interacts with this resonance. We can drive the resonance when the field is perpendicular to the surface of the plasma. This case can occur when the electric field of the incident wave is in the plane of incidence, termed p-polarized. Since the plasma is thin, we can consider the external field E_0 (note the external fields will be denoted with a subscript while the internal fields will not) to be uniform. From the boundary conditions, we know that the perpendicular \mathbf{D} field must be continuous across the boundary. This leads to,

$$\mathbf{D}_0 = \mathbf{D} = \mathbf{E}_0 = \epsilon \mathbf{E}, \quad \mathbf{E} = \frac{\mathbf{E}_0}{|\epsilon|}. \quad (3.29)$$

Clearly, when ϵ is near zero the field inside of the plasma can become greatly enhanced.

This is from the coupling of the plasma dipole to the driving field. Eq. 3.22 becomes

$$\frac{\partial U}{\partial t} = \frac{\omega}{8\pi} \frac{Im[\epsilon]}{|\epsilon|^2} |E_0|^2. \quad (3.30)$$

If we put in the Drude model (Eq. 3.15) for ϵ , we find the maximum heating per electron occurs when the plasma frequency equals the laser frequency, just as we expect. Defining the critical density, n_{crit} , as

$$n_{crit} \equiv \frac{m_e \omega^2}{4\pi e^2}, \quad (3.31)$$

we can say this resonance will occur when the electron density equals the critical density. If we started with a solid density thin film ($n_e > n_{crit}$) the field will be initially shielded. As it expands, it will pass through the resonance ($n_e = n_{crit}$) and there will be an enhancement of the heating. This effect can greatly increase the amount of energy transferred to the plasma.

Relationship to resonance absorption

Resonance absorption⁶³ is a well known process in laser interactions with plasma.⁶⁴ An obliquely incident p-polarized electromagnetic wave ($\mathbf{E} = E_x \hat{\mathbf{x}} + E_y \hat{\mathbf{y}}$) must satisfy Poisson's equation

$$\nabla \cdot (\epsilon \mathbf{E}) = 0. \quad (3.32)$$

If there is a density gradient where $\epsilon = \epsilon(x)$, using the identity $\nabla \cdot (\epsilon \mathbf{E}) = \epsilon \nabla \cdot \mathbf{E} + \nabla \epsilon \cdot \mathbf{E}$ we find that

$$\nabla \cdot \mathbf{E} = -\frac{1}{\epsilon} \frac{\partial \epsilon}{\partial x} E_x. \quad (3.33)$$

This says that the incident wave has developed an electrostatic component. As the electric field oscillates along the direction of the density gradient, charge oscillations are produced. This produces the electrostatic field. At the critical surface ($\epsilon = 0$) the incident electric field is resonantly enhanced and a large amount of energy can be transferred to this electrostatic oscillation or electron plasma wave. This wave is damped, through either collisional or collisionless processes, and the energy is transferred to the random motion of the electrons.⁶⁵

In our previous calculation, we assume a uniform density throughout the plasma. For this abrupt vacuum-plasma interface, we must match the appropriate boundary conditions across the interface, rather than looking at propagation through a continuous density gradient. The plasma is much smaller than the wavelength of light, so the electric field is constant over the scale of the plasma. All elements of the plasma will see the same field (Eq. 3.29). Hence, the electrostatic oscillations (Fig. 3.1) will lead to a surface charge oscillation (front surface to back surface) rather than an electron plasma wave. So while the process we discussed is similar to resonance absorption, the small size and sharp boundary makes this phenomena unique.

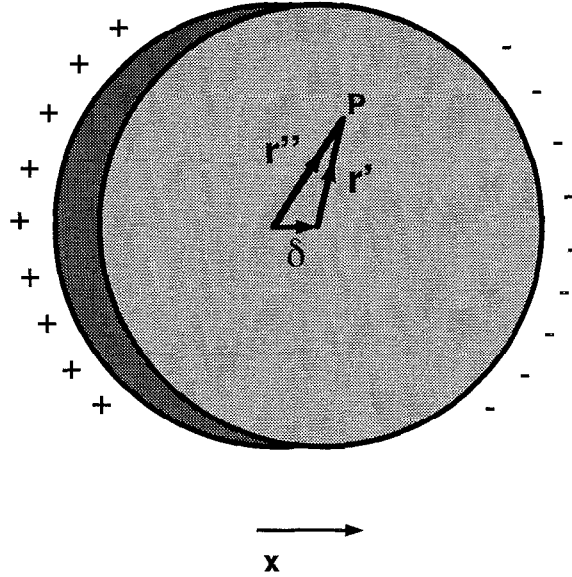


Figure 3.2: Geometry of an ideal spherical plasma.

3.2.4 Resonance in a spherical geometry

The natural frequency of a bounded spherical plasma is going to be different than our semi-infinite plasma calculated in section 3.2.3. The geometry makes this more complicated, but we can calculate the natural frequency of the spherical plasma by calculating the electric field inside of a sphere of ions and a sphere of electrons and then using the principle of superposition.⁶⁶

To calculate the field inside of a single sphere we use Gauss's law (Eq. 3.23) once again.

We find that,

$$\mathbf{E}(4\pi r^2) = 4\pi ne\left(\frac{4}{3}\pi r^3\right)\hat{\mathbf{r}}. \quad (3.34)$$

Which simplifies to

$$\mathbf{E} = \frac{4}{3}\pi en\mathbf{r}. \quad (3.35)$$

We need to look at the field inside of two spheres, oppositely charged, offset from each other slightly. The situation is shown in Fig. 3.2. The electric field inside the negative and

positively charged spheres, respectively, will be

$$\mathbf{E}' = -\frac{4}{3}\pi en\mathbf{r}', \quad \mathbf{E}'' = \frac{4}{3}\pi en\mathbf{r}''. \quad (3.36)$$

By the principle of superposition the electric field inside will be

$$\mathbf{E} = \mathbf{E}' + \mathbf{E}'' = \frac{4}{3}\pi en(\mathbf{r}'' - \mathbf{r}') = \frac{4}{3}\pi en\delta\hat{\mathbf{x}} \quad (3.37)$$

We calculate the force trying to pull the spheres together after they are separated

$$\mathbf{F} = q\mathbf{E} = -\frac{4}{3}\pi e^2 n\delta\hat{\mathbf{x}} = -m_e \frac{\omega_p^2}{3} \delta\hat{\mathbf{x}} \quad (3.38)$$

As before, to find the resonance frequency we look at the equation of motion. When the electron sphere is displaced a distance δ we have

$$\frac{d^2\delta}{dt^2} m_e = F = -m_e \frac{\omega_p^2}{3} \delta. \quad (3.39)$$

This leads to the differential equation

$$\frac{d^2\delta}{dt^2} + \frac{\omega_p^2}{3} \delta = 0. \quad (3.40)$$

As in section 3.2.3 we have the equation of an harmonic oscillator, but now the frequency is

$$\omega = \frac{\omega_p}{\sqrt{3}}. \quad (3.41)$$

This is similar to what we saw before, except for the factor of $\sqrt{3}$. This corresponds to the electron density being 3 times the usual critical density.

The incident wave will drive the cluster in an analogous manner as the thin slab. The major difference will be the field inside of the cluster. For a sphere (small compared to the wavelength) the internal field will be²⁵

$$E = \frac{3}{|\epsilon + 2|} E_0. \quad (3.42)$$

Plugging this into Eq. 3.22 we get

$$\frac{\partial U}{\partial t} = \frac{9\omega}{8\pi} \frac{\text{Im}[\epsilon]}{|\epsilon + 2|^2} |E_0|^2. \quad (3.43)$$

The maximum heating will now occur when $n_e/n_{crit} = 3$. We still see a large enhancement of the electric field and the laser heating, but it occurs at a higher density than for the thin slab.

3.3 Mie scattering

As mentioned before, section 3.2.4 assumes the cluster is very small compared to the wavelength of light. This is true in the beginning of the interaction. But once the resonance is reached the cluster expands rapidly becoming comparable to the wavelength. To get a more accurate picture of what is going on during the total interaction, we need to look at the solution of Maxwell's equations for an electromagnetic wave incident on a spherical object.

3.3.1 Historical perspective

The problem of a sphere in an electromagnetic field has been solved and is generally referred to as the Mie solution. History does a disservice to many people here since Mie⁶⁷ was not the first to develop this solution.⁶⁸ As far back as 1863, Clebsch⁶⁹ published a work on scattering from spheres. He published the exact solutions to the scalar wave equations. Lord Rayleigh published many works on scattering,⁷⁰ though he never fully solved the electromagnetic problem. Most germane to our discussion here is his 1881 publication,⁷¹ where he develops the equations for scattering from small objects which bear his name today. What we call the Mie solution was first published by Lorenz in 1890.⁷² Many others published these results,^{73,74} developed independently, around the turn of the century.

Mie published his work in 1908.⁶⁷ His theoretical development does not differ in any significant way with these previous works. What Mie did, however, was to apply this theory to an actual scattering problem. He presented calculations of scattering from colloidally dispersed metal particles. His methods presented a template for other researchers who wanted to do scattering calculations. These results were widely used by others and hence the entire solution came to bear Mie's name.

With all due respect for those who first developed the theory, in this thesis the solution will be referred to as the Mie solution. The derivation is involved and is presented in appendix A for the interested reader. Those further interested in this topic are referred to one of the excellent books published on the topic of scattering from spheres.^{75–77}

3.3.2 Cross-sections

For our calculations we only need the final results of appendix A. We can calculate the absorbed energy by computing the Mie extinction and scattering cross-sections,

$$\sigma_{ext} = \frac{2\pi}{k^2} \sum_{n=1}^{\infty} (2n+1) \text{Re}(a_n + b_n), \quad (3.44)$$

and

$$\sigma_{sca} = \frac{2\pi}{k^2} \sum_{n=1}^{\infty} (2n+1) \{|a_n|^2 + |b_n|^2\}, \quad (3.45)$$

where

$$a_n = \frac{m\psi_n(y)\psi'_n(x) - \psi_n(x)\psi'_n(y)}{m\psi_n(y)\xi'_n(x) - \xi_n(x)\psi'_n(y)}, \quad (3.46)$$

$$b_n = \frac{\psi_n(y)\psi'_n(x) - m\psi_n(x)\psi'_n(y)}{\psi_n(y)\xi'_n(x) - m\xi_n(x)\psi'_n(y)}, \quad (3.47)$$

m is the complex index of refraction of the sphere and $\psi_n(z), \xi_n(z)$ are the Riccati-Bessel functions, which are related to the spherical Bessel and Hankel functions

$$\psi_n(z) = z j_n(z), \quad (3.48)$$

$$\xi_n(z) = z h_n^{(1)}(z). \quad (3.49)$$

From conservation of energy we have

$$\sigma_{abs} = \sigma_{ext} - \sigma_{sca} \quad (3.50)$$

This is the absorption cross-section for a single cluster. Our target will consist of a large ensemble of spheres. For a medium containing N spheres per unit volume, over a distance l , the intensity of the incident beam will decrease by

$$e^{-Nl\sigma_{ext}}. \quad (3.51)$$

This contains all the information we need about IB heating. Using a Drude model to calculate the index of refraction we can calculate σ_{ext} and σ_{sca} and find the energy transferred to the clusters by collisional heating.

3.4 Cluster expansion

If we assume the cluster maintains a uniform density throughout its volume as it expands we can write⁷⁸

$$P4\pi r^2 \frac{\partial r}{\partial t} = \frac{\partial K_e}{\partial t}, \quad (3.52)$$

where P is the pressure inside of the cluster. From this we can compute the acceleration of the cluster expansion

$$\frac{\partial^2 r}{\partial t^2} = \frac{3P}{n_i m_i r}. \quad (3.53)$$

The pressure inside of the cluster is controlled by two processes. First, rapid ionization and free-streaming of electrons will cause charge to build up on the cluster; the excess charge on the cluster represents potential energy which is trying to push the cluster apart in a Coulomb explosion. The pressure from this effect is²⁵

$$P_{Coul} = \frac{Q^2 e^2}{8\pi r^4}, \quad (3.54)$$

where Qe is the accumulated charge on the cluster.

Additionally, the hot plasma formed will have an electron temperature which will create a pressure forcing a hydrodynamic expansion. The pressure from this will be

$$P_e = n_e k T_e \quad (3.55)$$

where T_e is the plasma electron temperature.

It is difficult to get an intuitive feel for the difference in magnitude of the two pressures. It would seem as if the $1/r^4$ scaling of the Coulomb pressure will cause it to rapidly decrease as we interact with larger and larger clusters. However, a larger cluster will have more ionization and more electrons will leave the cluster leading to a larger Q . Both n_e and T_e will be effected by cluster size, thus effecting the hydrodynamic pressure.

To examine this we are going to need to look at the free-streaming of the electrons. Initially the electrons will be able to leave the cluster easily when they are ionized. As charge builds up on the cluster an electron must have enough kinetic energy to overcome the Coulomb attraction in order to leave the cluster volume. Ditmire *et al.*²² estimated the free-streaming rate by looking at the cluster geometry and calculating the number of electrons with enough energy to escape the cluster which are within one mean free path (λ_e) of the cluster surface. This rate is

$$W_{FS} = \int \int_S v f(v) dS dv, \quad (3.56)$$

where $f(v)$ is a Maxwellian velocity distribution

$$f(v) = 4\pi n_e \left(\frac{m_e}{2\pi k T_e} \right)^{3/2} v^2 \exp \left[\frac{-m_e v^2}{2k T_e} \right]. \quad (3.57)$$

Because only a fraction of the electrons can reach the surface, dS is not simply dA . Accounting for the fraction which reach the surface we can write

$$dS = \frac{3\rho^2}{4\pi r^3} d(\cos \psi) d\phi d\rho dA, \quad (3.58)$$

where ρ is a distance from the origin along the vertical axis, ψ is the angle an electron's velocity makes with the vertical axis (defined as zero when the electron is moving downward along the axis), and ϕ is the azimuthal angle. From the geometry, we can form the constraints

$$\cos \psi_{max} = -1, \quad (3.59)$$

$$\cos \psi_{min} = \frac{\rho^2 + \lambda_e^2 - r^2}{2\rho\lambda_e}, \quad (3.60)$$

$$\rho_{min} = r - \lambda_e. \quad (3.61)$$

Hence, Eq. 3.56 can be written

$$W_{FS} = 4\pi r^2 \int_{v_{esc}}^{\infty} \int_{\rho_{min}}^r \int_0^{2\pi} \int_{\cos \psi_{max}}^{\cos \psi_{min}} v f(v) \frac{3\rho^2}{4\pi r^3} d(\cos \psi) d\phi d\rho dv. \quad (3.62)$$

Performing the integral we obtain

$$W_{FS} = n_e \frac{2\sqrt{2\pi}}{m_e^{1/2} (kT_e)^{1/2}} \exp \left[-\frac{K_{esc}}{kT_2} \right] \times \left\{ \begin{array}{ll} \frac{\lambda_e}{4r} (12r^2 - \lambda_e^2) & \lambda_e < 2r \\ 4r^2 & \lambda_e > 2r \end{array} \right\}. \quad (3.63)$$

where λ_e is given by⁷⁹

$$\lambda_e = \frac{(kT_e)^2}{4\pi n_e (Z+1) e^4 \ln \Lambda}, \quad (3.64)$$

and $\ln \Lambda$ is the standard Coulomb logarithm. We also need to estimate the minimum energy an electron needs to escape from the cluster, K_{esc} . We can use the potential energy of the Coulomb attraction at the surface of the sphere,

$$K_{esc} = \frac{(Q+1)e^2}{r} \quad (3.65)$$

3.5 Computer simulation

The model presented here is similar to the one used in previous publications.²² The largest difference is the inclusion of a Mie scattering code⁸⁰ which will be used to calculate the collisional heating in the cluster. This gives a more accurate answer for the case of longer pulse lengths, where the cluster expands to a size on the order of the wavelength. The code uses a second order Runge-Kutta method⁸¹ to perform the numerical integration. The ionization, free streaming, cluster heating, and cluster expansion are calculated from the equations in the previous sections. Corrections are made to the electron temperature to account for ATI, energy loss from free streaming, and energy absorbed during collisional ionization. These corrections are small but are included for completeness.

The first thing we will look at is the heating of the cluster. Figure. 3.3 shows the heating and electron density of an individual cluster. As the laser irradiates the cluster the atoms are rapidly ionized and an overdense plasma is formed. As the intensity increases the cluster expands while electrons continue to be ionized; ionization still dominates and the electron density increases. Eventually the rate of expansion overcomes the rate of ionization and the electron density begins to drop. At $n_e/n_{crit} = 3$ the cluster undergoes rapid heating because of the enhancement of the internal electric field due to the resonance condition. The energy absorbed increases an order of magnitude at this point. This heating causes a rapid

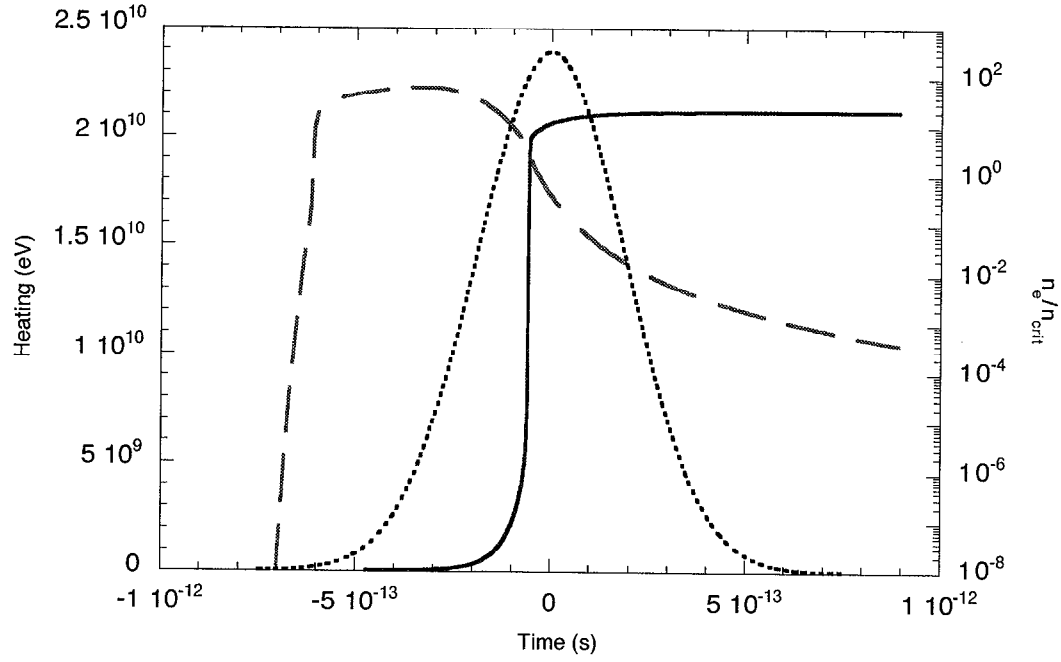


Figure 3.3: Heating and density of a 100 Å initial radius xenon cluster. The laser conditions are 450 fs and an intensity of 1.1×10^{16} W/cm². The graph shows the total energy absorbed by collisional heating per cluster (solid), the electron density compared to the critical density (dashed) and the relative intensity of the laser pulse (dotted).

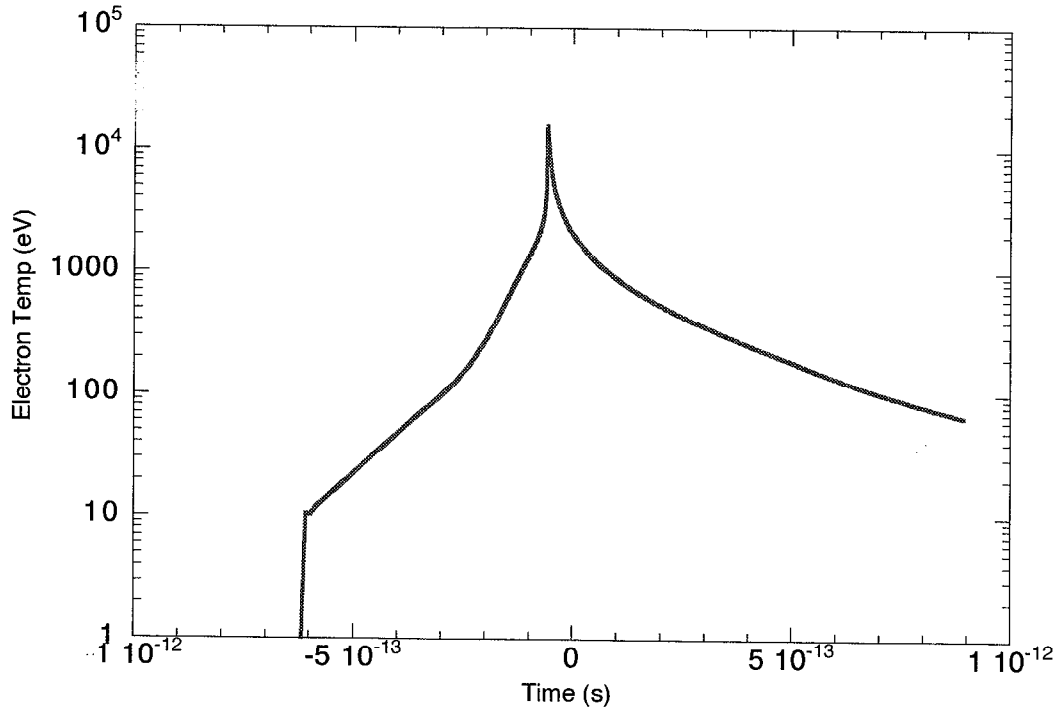


Figure 3.4: Electron temperature of a 100 Å initial radius xenon cluster. The laser conditions are 450 fs and an intensity of 1.16×10^{16} W/cm².

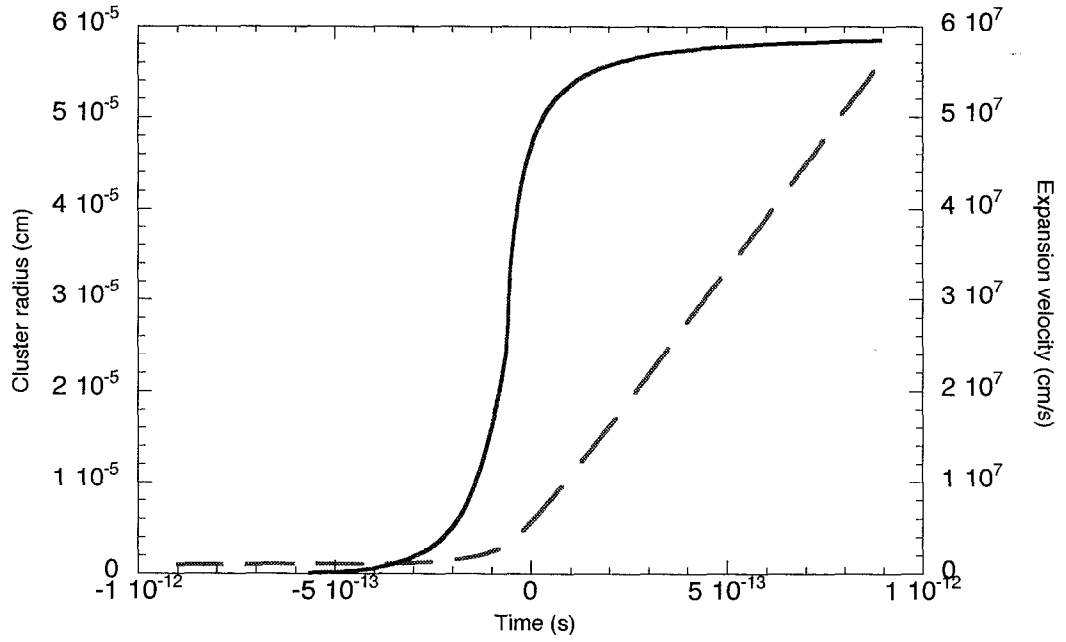


Figure 3.5: Expansion velocity and radius of 100 Å initial xenon radius. The laser conditions are 450 fs and an intensity of 1.16×10^{16} W/cm². The solid line is the velocity and the dashed line is the cluster radius.

spike in the electron temperature (Fig. 3.4) up to 10 keV. The cluster now rapidly expands and cools. The cluster forms an underdense bulk plasma and hence interacts weakly for the remaining duration of the laser pulse.

The rapid acceleration is seen in Fig. 3.5. Just before the peak of the laser pulse, when the resonance occurs, the velocity increases rapidly. In the latter half of the pulse, the radius is increasing at a high rate; the cluster approaches the size of the laser wavelength. At this point we can no longer make the small cluster approximation and need to use the full Mie formulas to accurately calculate the absorption.

The problem with using the small sphere approximation (Eq. 3.43) is that it will predict a heating that is too high as the cluster radius becomes comparable to the wavelength. This will be a problem for longer pulse widths, since the cluster has more time to expand during the pulse. Figure 3.6 shows the total heating using Eq. 3.43 and the full Mie solution. At

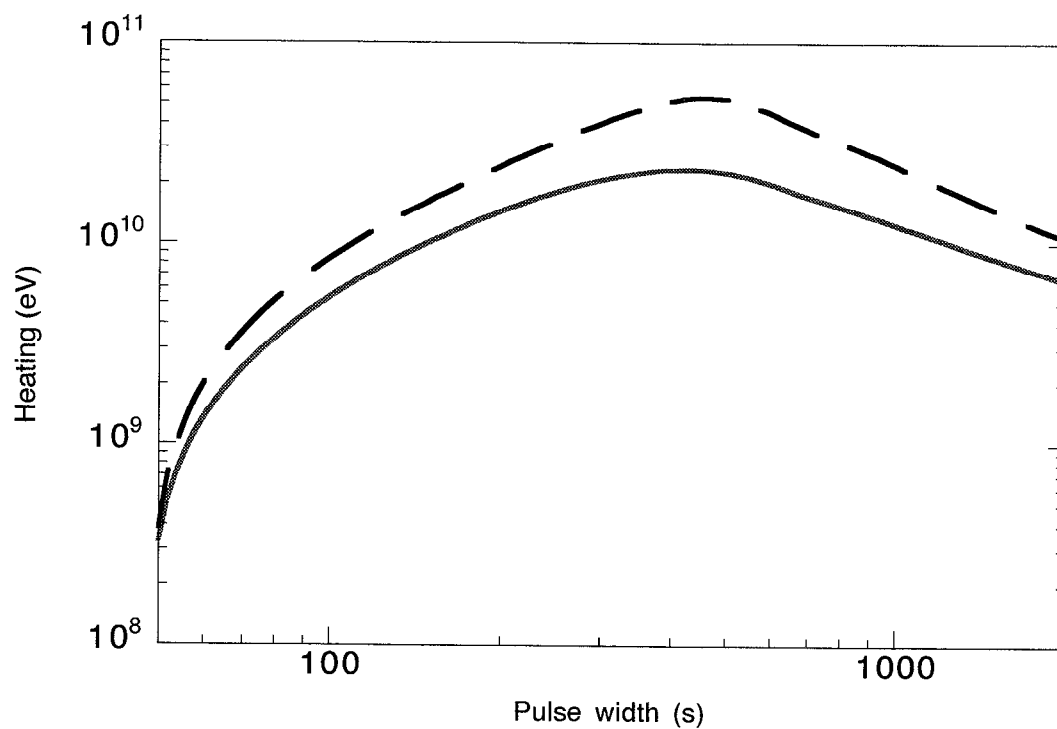


Figure 3.6: Heating of 100 Å initial radius xenon cluster using the small sphere approximation (dashed) and the full Mie solution (solid). The small sphere approximation overestimates the heating as the cluster radius becomes comparable to the wavelength.

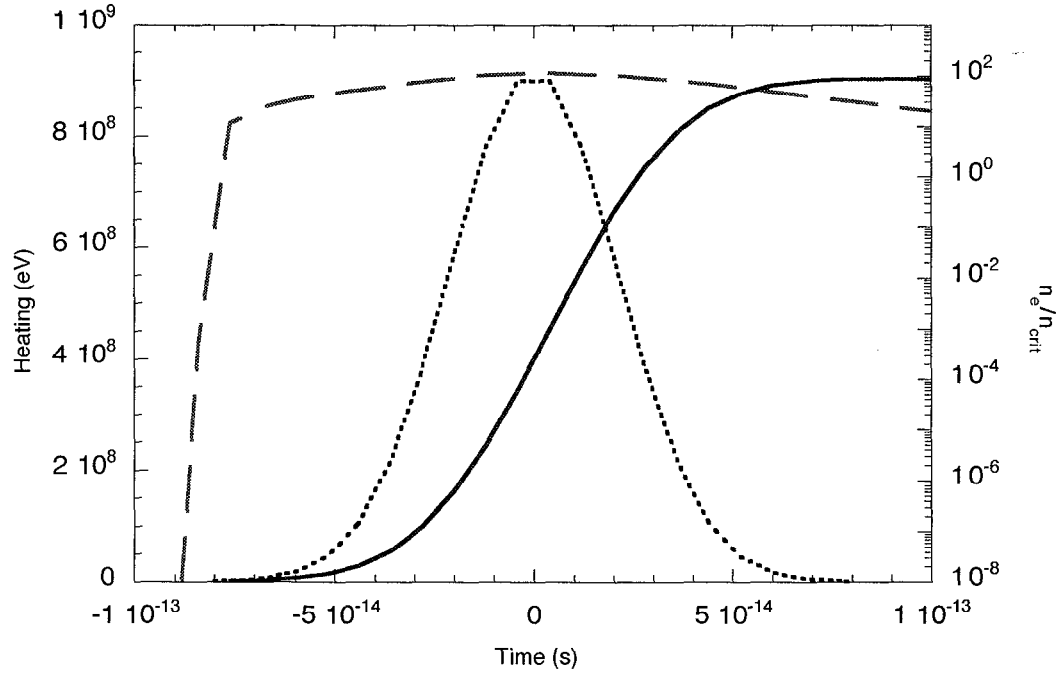


Figure 3.7: Heating and density of a 100 \AA initial radius xenon cluster. The laser conditions are 50 fs and an intensity of $1.0 \times 10^{17} \text{ W/cm}^2$. The graph shows the total energy absorbed by collisional heating per cluster (solid), the electron density compared to the critical density (dashed) and the relative intensity of the laser pulse (dotted).

short pulses the heating is similar. As the pulse width gets longer, the heating is larger for the small sphere approximation. This will overestimate the absorption, and shows the need for the full Mie calculation.

Where the resonance occurs during the laser pulse is going to greatly effect the transfer of energy between the laser and the cluster. There will be more heating if the resonance occurs near the peak of the pulse, rather than in the wings. If we use a short enough pulse, the laser will be gone before the cluster reaches resonance. This can be seen in Fig. 3.7. We do not see the sharp increase in the heating as in Fig. 3.3. We ionize the cluster and create an overdense plasma, but now there is not enough time for that plasma to expand to the resonance condition. Hence we see over an order of magnitude less energy absorbed by the cluster compared with Fig. 3.3. This leads to the idea of an optimal pulse width for

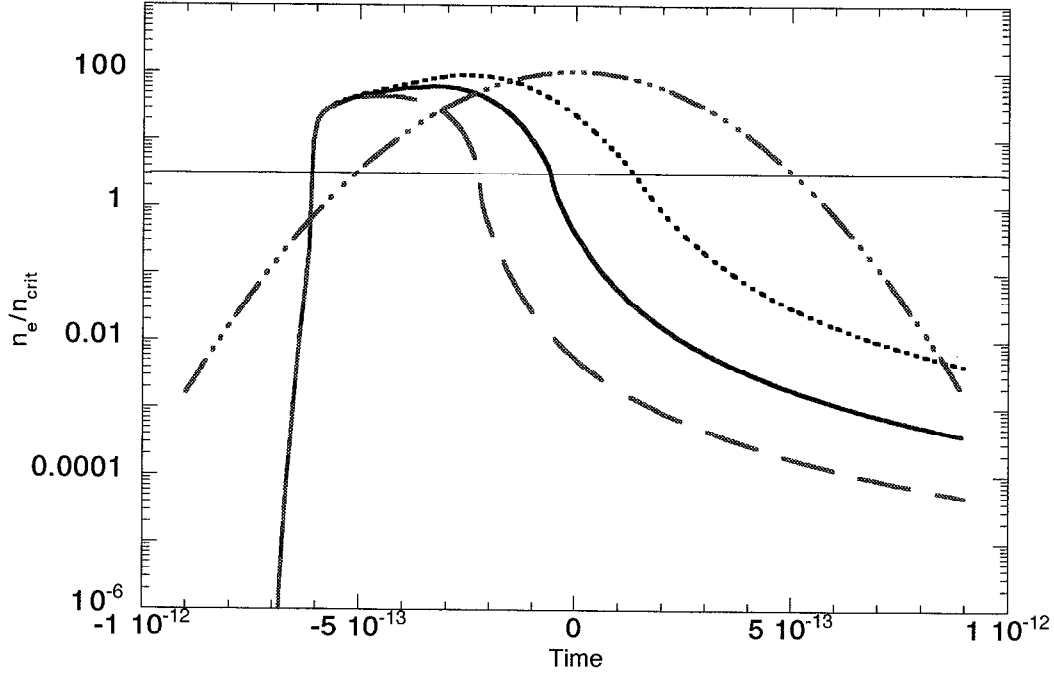


Figure 3.8: Density of different sized xenon cluster. The laser conditions were 450 fs and an intensity of 1.16×10^{16} W/cm². The sizes modeled were: 50 Å(dashed), 100 Å(solid), and 200 Å(dotted). The dotted dashed line is the relative laser intensity.

heating which will be investigated experimentally in the next chapter.

The time for a cluster to reach resonance will depend on initial cluster radius. If we assume a constant expansion velocity, the radius of the cluster becomes

$$r(t) = r_0 + vt, \quad (3.66)$$

where r_0 is the initial radius. The time it takes for a cluster to expand to resonance ($n_e = 3n_{crit}$) is

$$\tau_r = \frac{r_0}{v} \left[\left(\frac{n_0}{3n_{crit}} \right)^{1/3} - 1 \right], \quad (3.67)$$

where n_0 is the initial density, n_{crit} is the critical density, and v is the expansion velocity.

From Eq. 3.66 we can write

$$n(t) \propto (r_0 + vt)^{-3}. \quad (3.68)$$

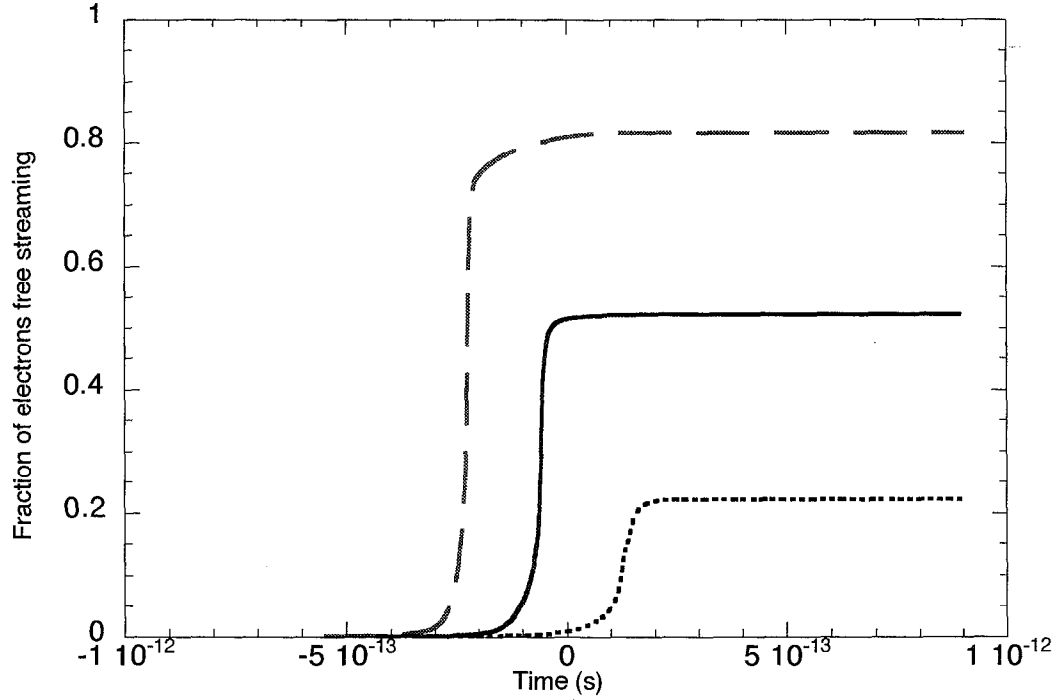


Figure 3.9: Free-streaming of electrons from different sized xenon cluster. The laser conditions were 450 fs and an intensity of 1.16×10^{16} W/cm². The sizes modeled were: 50 Å (dashed), 100 Å (solid), and 200 Å (dotted).

Taking the derivative we find

$$\frac{dn}{dt} = -3v(r_0 + vt)^{-4}. \quad (3.69)$$

From this we see that the density of larger clusters will initially change slower than small clusters. From this we expect the breadth of the resonance to be larger for larger clusters.

Figure 3.8 shows the density of various sized clusters interacting with a 450 fs pulse. Each size reaches $n_e/n_{crit} = 3$ at a different point in the laser pulse. Each size would be expected to have a different optimal pulse width for maximum absorption.

In a small cluster (a few atoms), all of the electrons leave the cluster once the atoms are ionized. This leads to the well know Coulomb explosion⁸² which is used to also describe the dynamics of molecules in intense fields. Large clusters will confine the electrons to their volume behaving like a plasma, much like a laser fusion target capsule. In the range of

several hundred to millions of atoms the behavior is some combination of the two. Figure 3.9 shows the fraction of ionized electrons which free-stream away from different sized clusters. The larger a cluster is, the smaller the fraction of electrons that leave. It should be noted that this calculation overestimates the free streaming rate since it does not account for the changes in the Maxwellian distribution of electron energies in the cluster from the free streaming.²²

Figure 3.9 also shows that the majority of the electrons which leave the cluster do so during the resonance. The cluster plasma is effectively neutral before it reaches this point. We would expect the hydrodynamic forces to dominate in this region. We can see this in Fig. 3.10. Before the resonance the hydrodynamic pressure is well above the Coulomb pressure, driving a hydrodynamic expansion. There is a spike in the pressure at the resonance which causes the rapid acceleration seen in Fig. 3.5. This is when most of the free streaming occurs, increasing the charge on the cluster. After resonance, the pressure drops rapidly. The smaller cluster has lost most of its electrons, and hence the Coulomb pressure is larger than the hydrodynamic pressure; while in the large cluster the two pressures are nearly equal.

3.6 Conclusion

This completes the basic theory of laser-cluster interactions. This theory assumes the cluster can be treated as a plasma. We have seen that a large fraction of the electrons are confined to the cluster (especially in larger clusters), supporting the plasma assumption. The clusters expand during the laser pulse and, for longer pulses, become comparable to the wavelength of the laser. At this point a full Mie calculation has to be performed in order to compute energy absorption. A small sphere approximation²² will overestimate the absorbed energy.

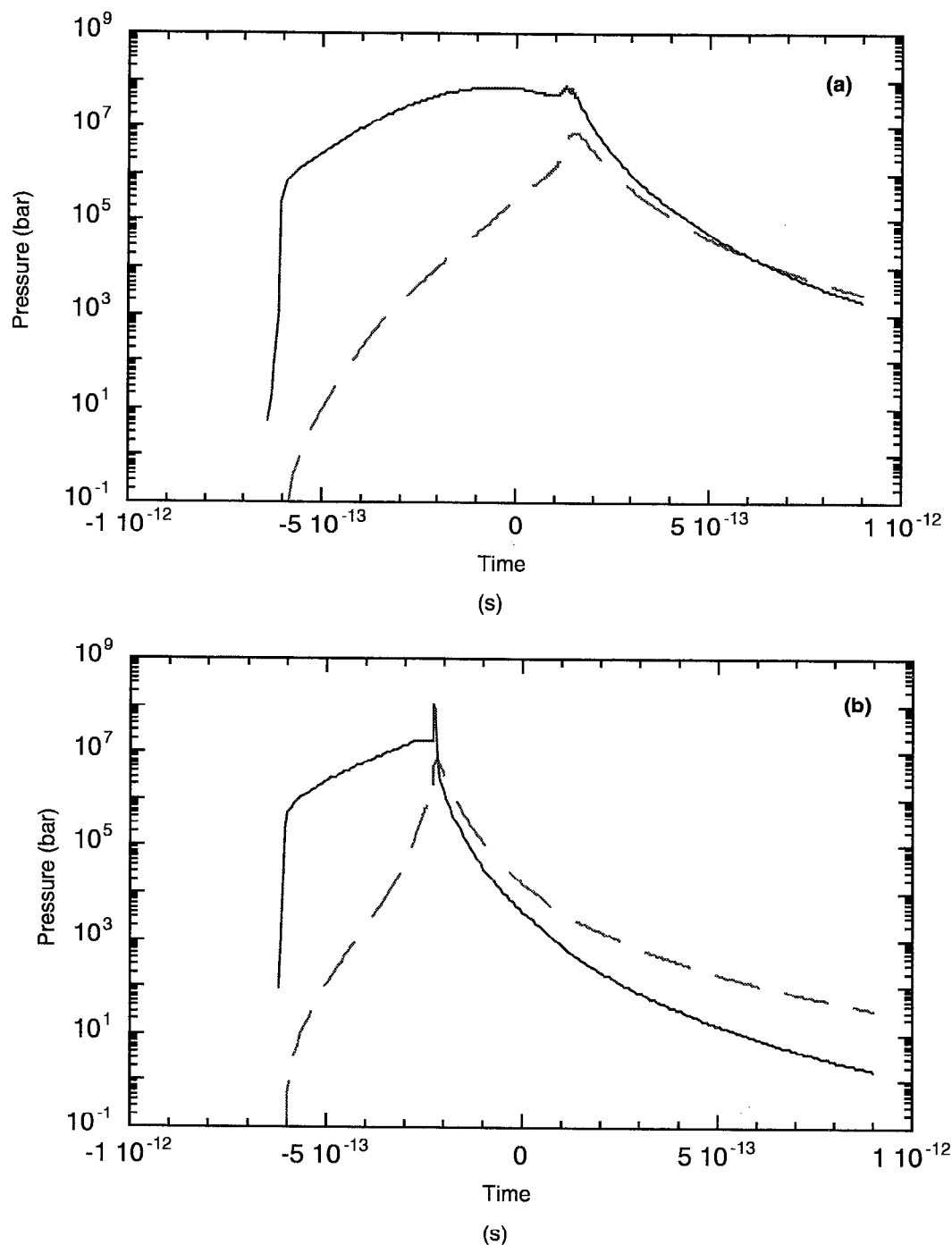


Figure 3.10: Coulomb (dashed) and hydrodynamic pressure (solid) on xenon clusters. (a) 50 \AA cluster and (b) 200 \AA cluster. The laser conditions are 450 fs and an intensity of $1.16 \times 10^{16} \text{ W/cm}^2$.

Modeling shows that a resonance, when $n_e = 3n_{crit}$, will greatly effect the absorption. Different pulse widths should interact differently with this resonance. We now move on to examine this experimentally.

Chapter 4

Absorption and Soft X-ray Experiments

4.1 Experimental design

The experiments in this section were conceived to test the hydrodynamic theory of cluster interactions. Our goal was to directly observe the effects of resonance on the coupling of the laser energy to the cluster target. We needed to perform a time resolved measurement with a resolution much greater than the expansion time to resonance. From Eq. 3.67 we estimate the expansion time to be on the order of 100's of femtoseconds to a few picoseconds. It was with this in mind, that we designed and built the 50 fs laser system, described in chapter 2.

4.2 Cluster formation and characterization

Clusters are formed by the expansion of a gas into a vacuum through a nozzle. The gas jet used in these experiments was a Mach 8 Laval nozzle. This nozzle was attached to a standard General Valve solenoid gas jet. The throat diameter was $150\ \mu\text{m}$, and the half

angle of the nozzle was 5° . The jet was backed with 50–200 psi of xenon or 300–600 psi of argon. Based on our calculations of laser absorption to be discussed in section 4.3.5 we estimate the average gas density to be 6.9×10^{17} at 200 psi and it scales linearly with pressure. This is in reasonable agreement with previous density measurements of these jets.⁸³

Cluster sources have been thoroughly investigated by the chemistry community. They have studied their formation^{13,84} and electronic properties.^{14,85} The onset of cluster formation can be determined by calculation of the Hagen scaling parameter, Γ^* . This is defined as

$$\Gamma^* = k \frac{d_{eq}^{85} p_0}{T_0^{2.29}} \quad (4.1)$$

where p_0 is the stagnation pressure in mbar, T_0 is the initial gas temperature, d_{eq} is the equivalent jet throat diameter in μm , and k is a constant depending on the gas used ($k=5500$ for Xe, 2890 for Kr, and 1650 for Ar).⁸⁵ For a sonic jet, d_{eq} is the actual throat diameter, d . However, for a supersonic nozzle it is equal to $.73d/\tan\alpha$, where α is the nozzle half angle.⁸⁶

The relation of the Hagen parameter to average cluster size can be found in the literature (Fig. 4.1).⁸⁵ The onset of clustering is seen when the Hagen parameter is about 300. For the conditions of these experiments the Hagen parameter is on the order of several times 10^4 , so we expect the formation of massive clusters. If we extrapolate from Fig. 4.1 we can write a power law relation for \overline{N}

$$\overline{N} = 4.33 \times 10^{-4} (\Gamma^*)^{1.87} \quad \Gamma > 1000 \quad (4.2)$$

We needed to measure the sizes of the clusters produced from this jet to ensure they agree with the Hagen scaling. The standard method for measuring cluster size is with

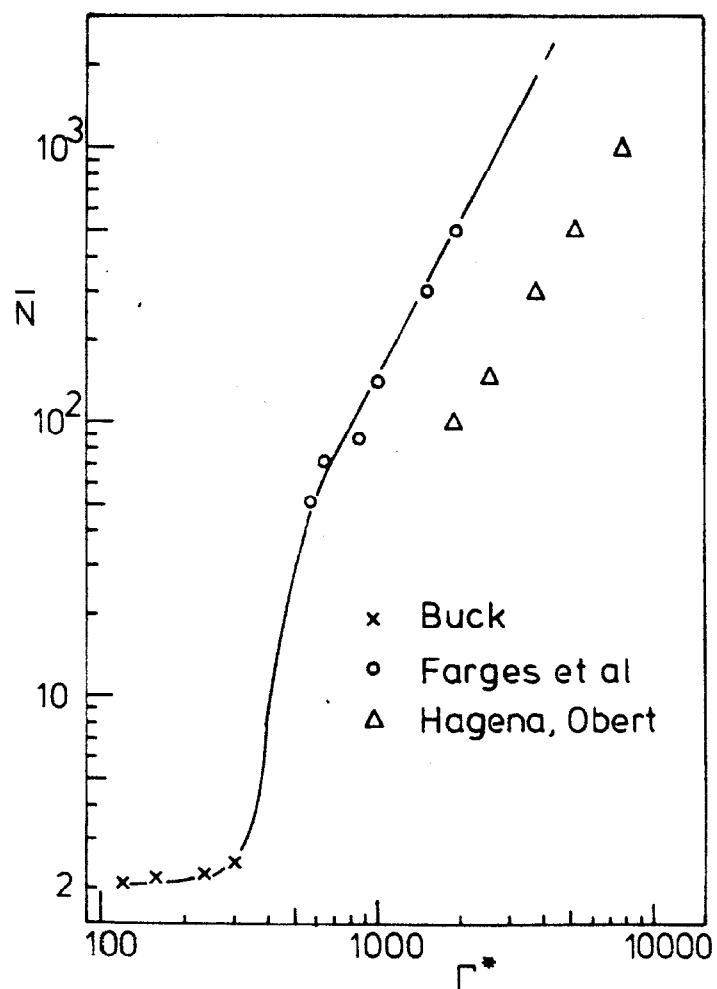


Figure 4.1: Cluster size as a function of Hagen parameter. The data points are from the literature.^{13,87,88} Reprinted from Chem. Phys. Lett. **159**, "Fluorescence excitation spectroscopy of xenon clusters in the VUV," p. 322, Copyright 1989, with permission from Elsevier Science.

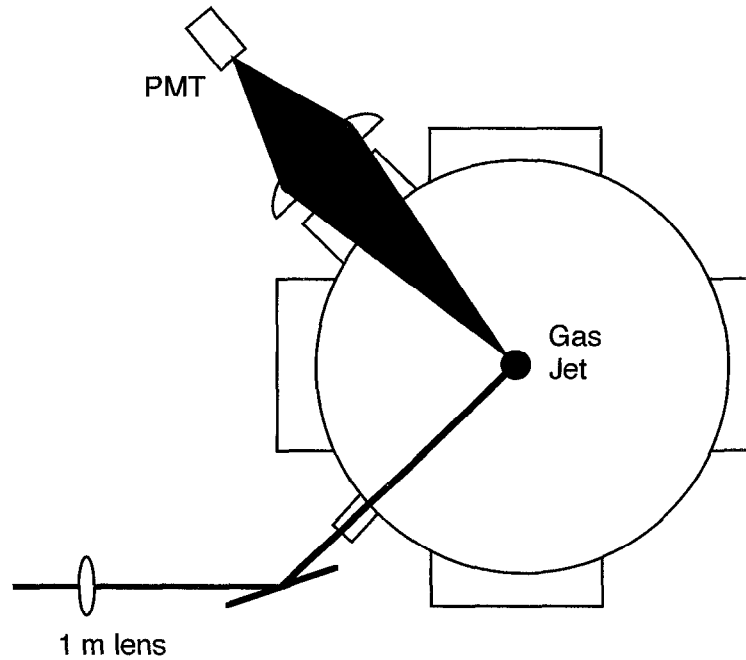


Figure 4.2: Setup for cluster size measurement.

electron impact ionization followed by time of flight (TOF) spectroscopy.¹³ This gives a measurement of the charge to mass ratio from which the full cluster size distribution can be determined. Unfortunately this cannot be done with the very large clusters we are using in these experiments. Large clusters will fragment once they are ionized and we will not be able to determine the initial size distribution.

To get information about the cluster sizes we will use Mie scattering. This will not break apart the clusters. However, we will only be able to measure an average cluster radius. Since the clusters are much smaller than the wavelength of the laser we will use (532 nm), we can use the Rayleigh scattering limit. In this limit the differential scattering cross-section is

$$\frac{d\sigma}{d\Omega} = 2\pi \frac{r^6}{\lambda^4} \left(\frac{n^2 - 1}{n^2 + 2} \right) \cos^2 \theta, \quad \text{for } \mathbf{E} \parallel \text{scattering plane} \quad (4.3)$$

$$\frac{d\sigma}{d\Omega} = 2\pi \frac{r^6}{\lambda^4} \left(\frac{n^2 - 1}{n^2 + 2} \right), \quad \text{for } \mathbf{E} \perp \text{scattering plane} \quad (4.4)$$

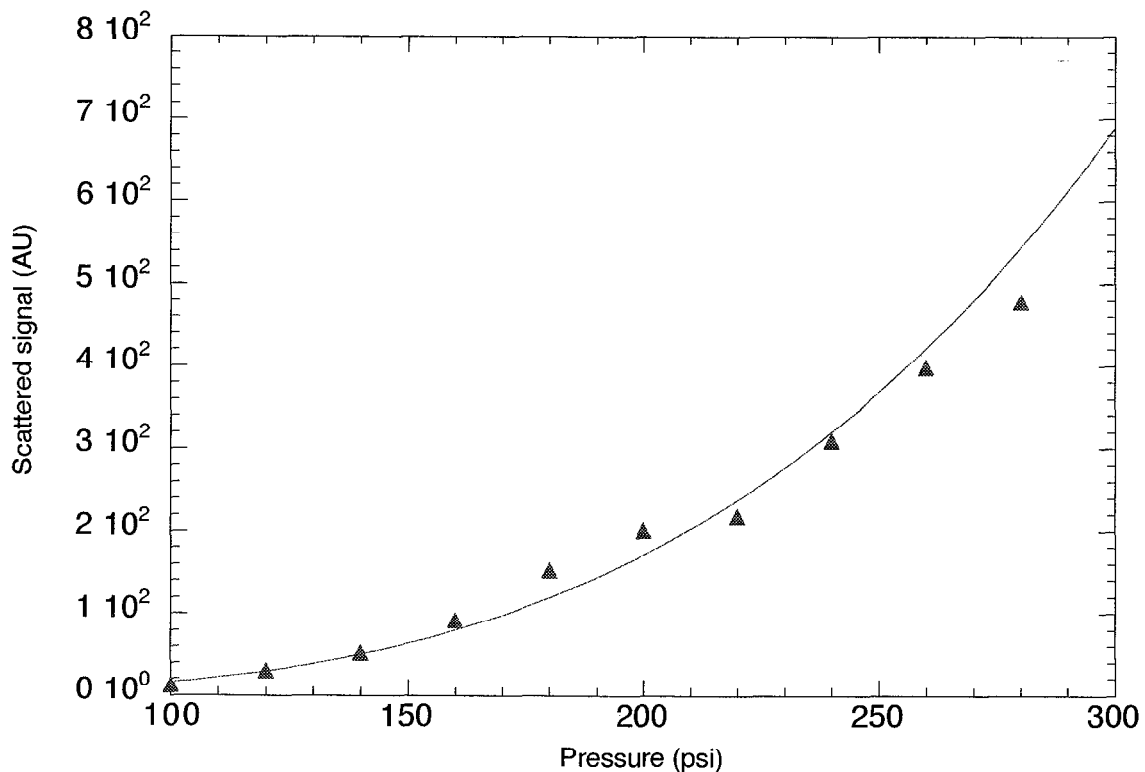


Figure 4.3: Rayleigh scatter measurement for Xe. The line is a power law curve fit to the data.

where n is the index of refraction of the clusters, λ is the wavelength of the scattered light, θ is the angle in the scattering plane with respect to the k -vector, and r is the cluster radius. The setup for this measurement is shown in Fig. 4.2. Our diagnostic measured the light scattered perpendicular to the polarization, at $\theta = 90^\circ$. The incoming beam, several hundred microjoules from the doubled Nd:YAG pump laser, is approximately 1 cm in diameter. It is focused with a 1 m lens onto the target. The scattered light is collected with a large 30 cm focal length lens and imaged onto a photomultiplier tube (PMT).

Figure 4.3 shows some scattering data from Xe. The signal goes as $p_0^{3.4}$ which is in reasonable agreement with the expected p^3 relation.²² We can estimate the average cluster size from the magnitude of the scattered signal. Using the index of refraction for solid Xe⁸⁹ we calculate the mean cluster radius at 200 psi backing pressure to be 200 Å.

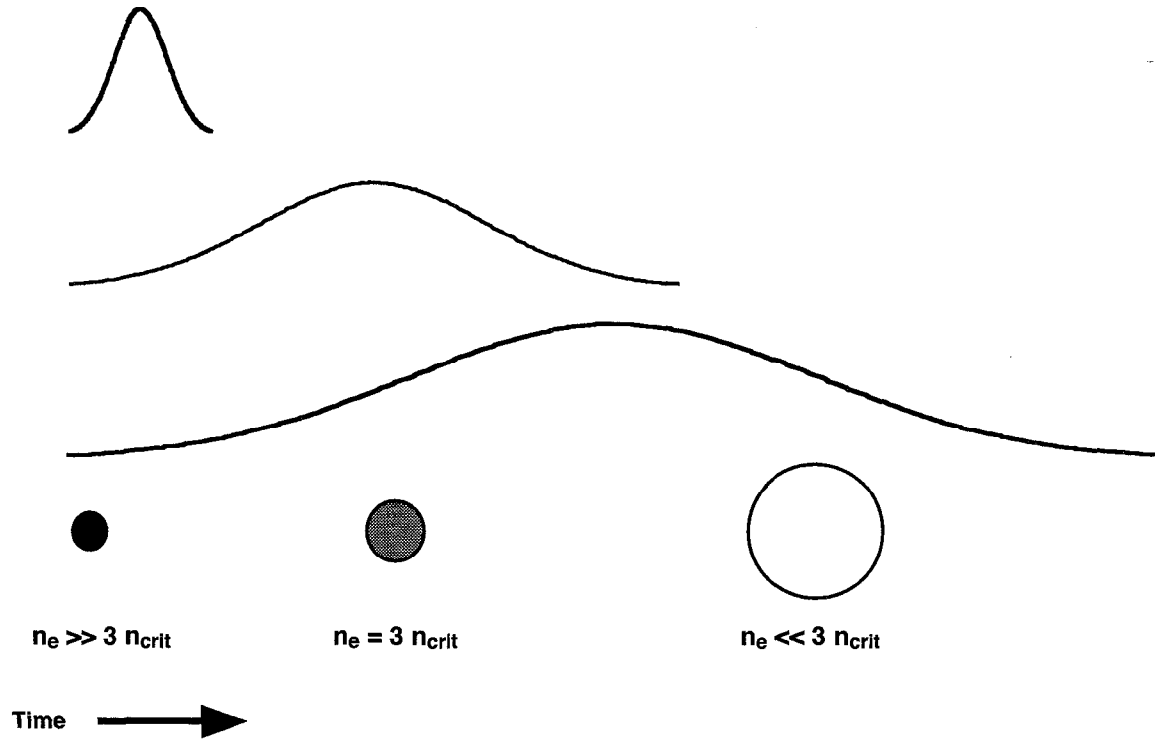


Figure 4.4: Experimental concept for variable pulse width experiments.

If we calculate the Hagena parameter and use Eq. 4.2 we find the cluster radius is 205 Å.¹⁴ This is excellent agreement, and we will use the Hagena parameter to estimate our cluster sizes. In xenon the cluster radii are 205 Å, 170 Å, 130 Å, and 85 Å for 200, 150, 100, and 50 psi, respectively. In argon the cluster radius is 110 Å at 300 psi and 170 Å at 600 psi. Assuming the clusters are of solid density,⁹⁰ the number of atoms range from 4×10^4 for 50 psi Xe, to 6×10^5 for 200 psi Xe. In Ar the number of atoms ranged from 1.3×10^5 to 5×10^5 .

4.3 Variable pulse width experiments

The initial experiments to examine the cluster resonance used a variable laser pulse width. The concept behind these experiments is shown in Fig. 4.4. With a very short laser pulse

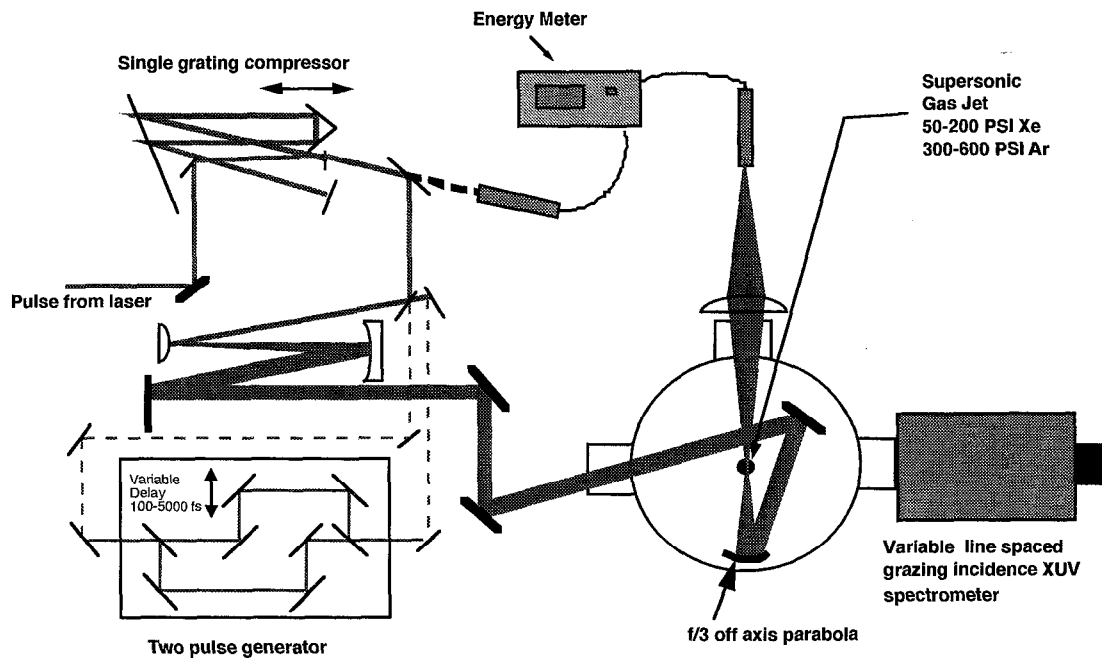


Figure 4.5: Setup for cluster experiments.

(top), the pulse passes before the cluster has had enough time to expand to the resonance condition. We would expect absorption to be low in this case. When the pulse width is longer (middle), such that the laser pulse is near its maximum intensity when the resonance condition is met, the absorption should be much higher. If the pulse gets too long (bottom), the majority of the laser pulse interacts with a greatly expanded cluster and again we should see low absorption.

4.3.1 Experimental setup

The experimental setup is shown in Fig. 4.5. We can adjust the pulse width of the laser by varying the spacing of the fold mirror in the compressor. After the single grating compressor, the beam was sent to an expanding Galilean telescope ($M=4\times$). This was done to minimize the accumulation of non-linear phase traveling through the air and the 1 cm thick fused silica target chamber window. Additionally, this beam expansion permitted a lower

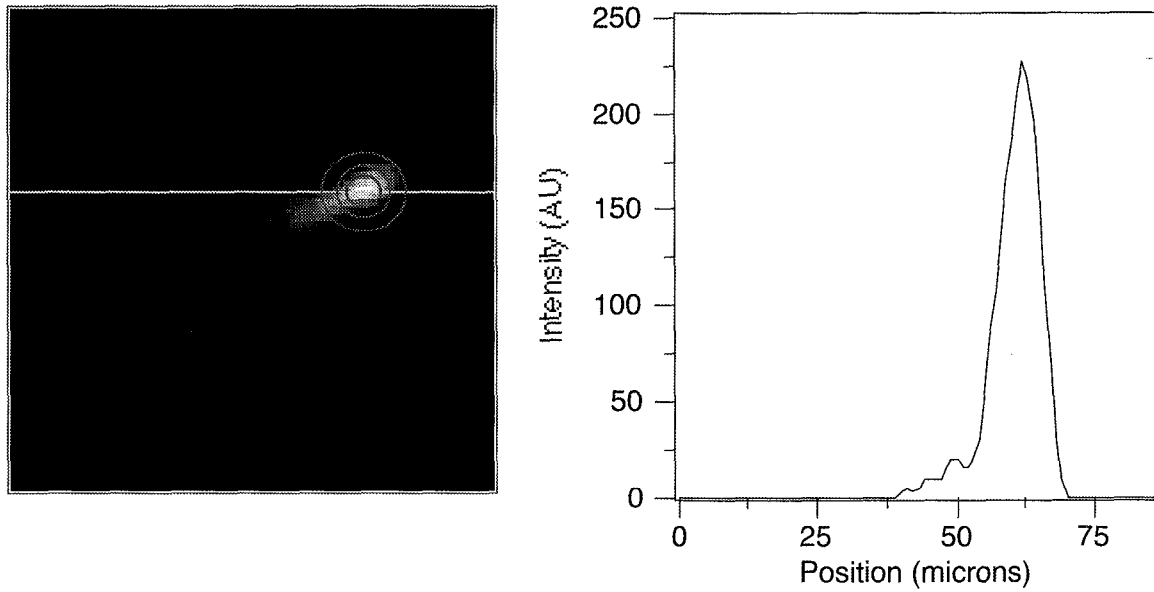


Figure 4.6: Image of focal spot with f/3 paraboloid. The circles contain 25%, 50%, and 75% of the energy.

f-number for our final focusing, increasing the intensity on target. After the telescope the beam was sent into a 2' diameter, spherical target chamber. The beam was then focused with an f/3 off axis paraboloid onto a cluster target. The focal spot can be seen in Fig. 4.6. Approximately 70% of the energy was contained in a $9\text{ }\mu\text{m}$ gaussian spot, with the remaining energy in low intensity wings.

The input energy of the laser was measured with a pyroelectric energy meter, measuring transmitted light through one of the mirrors before the target. The laser energy transmitted through the target was collected with an f/2.3 lens and measured with a similar energy meter. We checked for scattered laser light (90° , 45° forward) by imaging the interaction region onto a silicon detector with an f/2.3 lens. Additionally, we looked for backscattered light by placing a diode behind the dielectric mirror before the entrance of the chamber. These data will be discussed in chapter 5, but the signals levels were small. We found only a negligible amount of energy was scattered ($< 1\%$ over 4π sr), so the absorbed energy was taken to be the difference between the input and output energies. The absorption

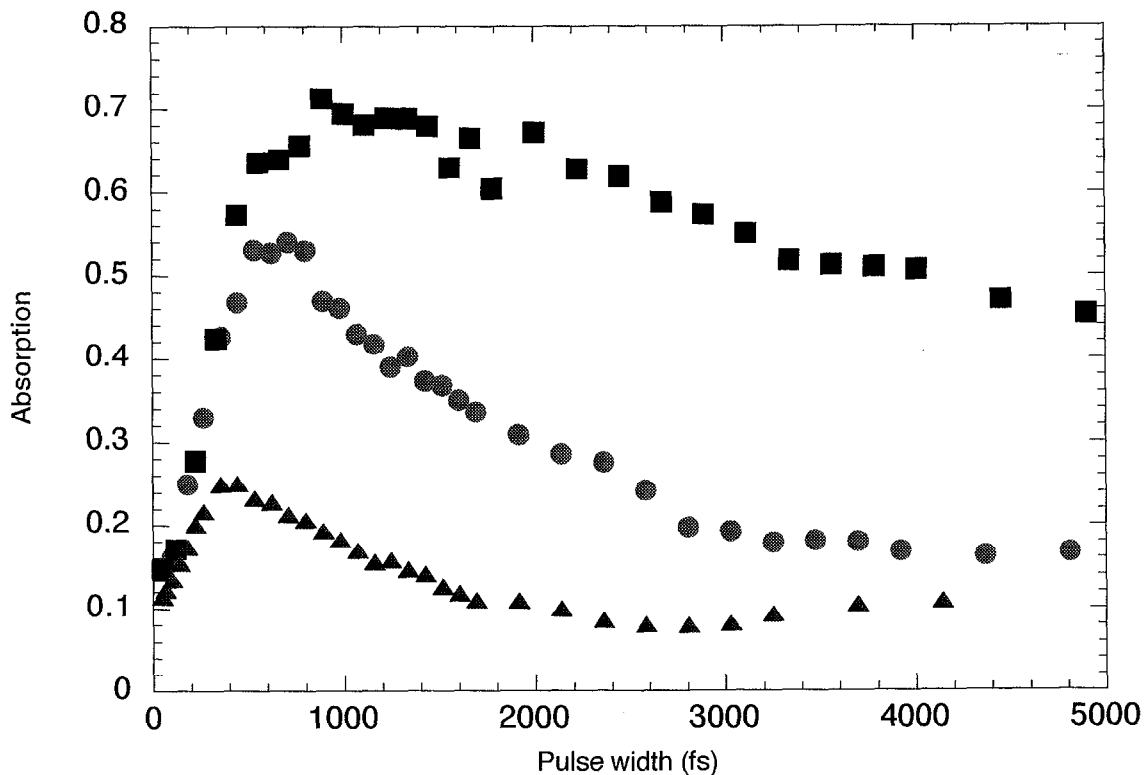


Figure 4.7: Absorption measurement in xenon for variable pulse length experiments. The pressure 50 (diamonds), 100 (circles), 200 (squares) psi.

measurements were averaged over 50 shots. We also utilized a variable line spaced, grazing incidence soft x-ray spectrometer (resolution = $\lambda/\Delta\lambda \approx 100$)⁹¹ with a soft x-ray CCD camera to look at plasma emission with wavelengths between 170 Å to 300 Å. There was a 3000 Å thick Al filter in the spectrometer to prevent the laser radiation from getting to the CCD.

4.3.2 Absorption measurements

Figure 4.7 shows the results of absorption measurements as a function of laser pulse duration for several pressures. The laser energy is about 6.5 mJ, with a peak intensity of 2.3×10^{17} W/cm² in vacuum for a 50 fs pulse. When the pulse is short the absorption is about 15%. At 50 fs, the pulse length is small compared to the hydrodynamic expansion time. An

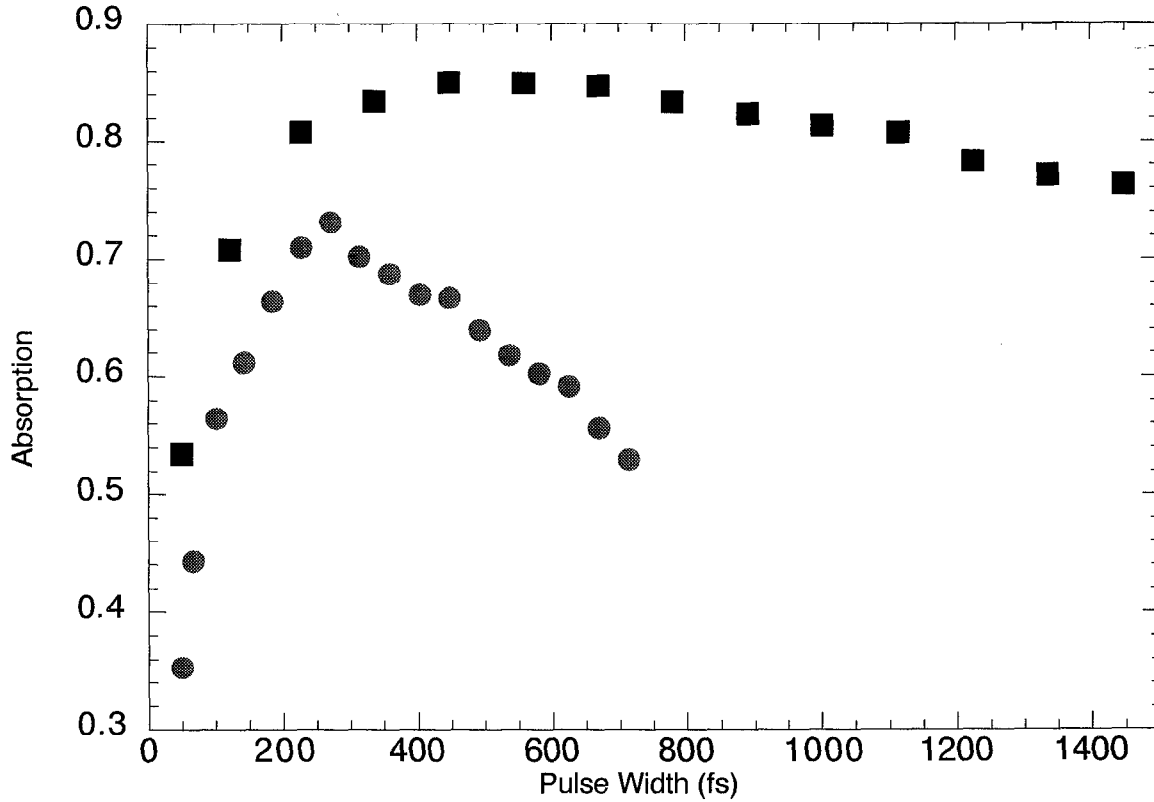


Figure 4.8: Absorption measurement for variable pulse length experiments. The target was argon at 300 (circles) and 600 (squares) psi.

overdense plasma is formed from each cluster, but by the time it expands to the resonance condition, the laser pulse is already past. As the pulse gets longer the resonance begins to occur during the laser pulse, enhancing the absorption. Eventually, the absorption begins to fall off as the resonance occurs early in the pulse and most of the laser energy interacts with a bulk plasma with relatively low density.

As the cluster size increases, the peak absorption occurs for a larger pulse width. This is expected from Eq. 3.67. We also observe that the width of the resonance is larger for increasing cluster size. In a larger cluster the rate of change in density is less than for a smaller one. Hence, a larger cluster will be near resonance for a longer period of time, increasing the absorption of laser light.

We should see similar effects in other cluster species. The absorption results for argon

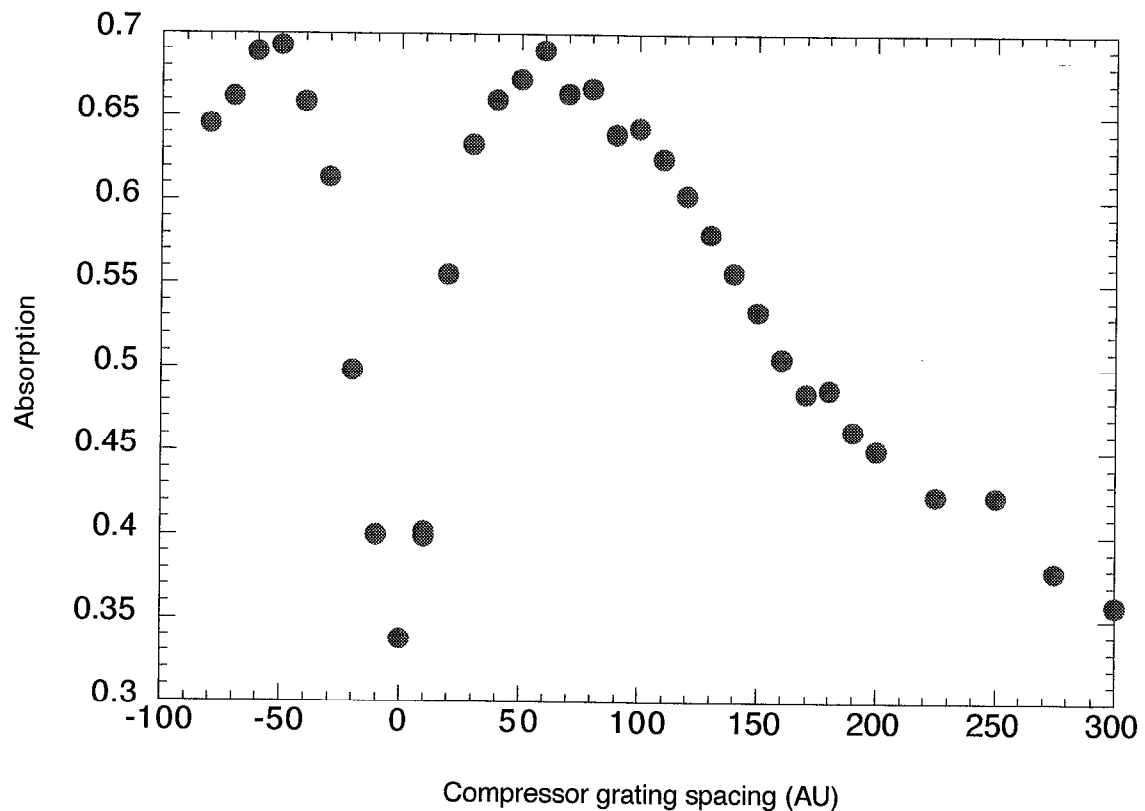


Figure 4.9: Absorption measurement for both positive and negative chirp. Negative grating spacing indicates positive chirp and positive spacing is negative chirp. The target was Ar at 300 psi.

are seen in Fig. 4.8. The graph shows the same trend as in xenon. The larger clusters take a longer time to reach resonance, and the resonance is wider as well.

Note on pulse chirp

When we change the grating spacing to get a longer pulse width we are chirping the pulse. The resonance condition is dependent on the laser frequency through the critical density. If the instantaneous frequency is varying in the direction such that it matches the changes in the plasma frequency due to expansion (negative chirp) there may be higher absorption. In Fig. 4.9 we look at absorption as we sweep the pulse width from positive chirp (negative spacing), to transform limited pulse, to negative chirp (positive spacing). There is no

significant difference for positive or negative chirp. If there is an effect here it is small.

4.3.3 X-ray measurements

As electrons recombine with ions and transition between energy levels, radiation will be emitted. Along with the kinetic energy of electrons and ions, this is one of the ways the absorbed energy will be emitted from the plasma. We expect the increased absorption seen in the previous section to imply increased x-ray emission.

The spectra from argon (600 psi) at two different pulse lengths are shown in Fig. 4.10. The spectra were integrated over 20 shots. The pulse length was 50 fs, corresponding to a peak intensity in vacuum of 1.9×10^{17} W/cm² for the left spectra; and the pulse length was 900 fs, corresponding to 1.1×10^{16} W/cm² for the right one. The input energy is the same in both spectra (5.4 mJ). The frequency increases vertically in the raw spectra, with the lower emission edge being about 170 Å, which is the cutoff of the Al filter. The x-ray yield increased almost 400% by making the pulse length 18 times longer. Although the intensity has dropped by over an order of magnitude, the two spectra look similar. Collisional ionization still produces a significant amount of sodium-like argon at 1.1×10^{16} W/cm², while tunnel ionization does not.⁹²

By estimating the total throughput of our system we can find the overall conversion efficiency. From the manufacture's literature, the quantum efficiency of the back-illuminated CCD is 40% in this energy range. The energy gain is approximately 1 electron per 3.65 eV of photon energy. The spectrometer subtends 5.81×10^{-6} sr. Throughput of the spectrometer is estimated⁹³ to be about 1% and the Al filter in front of the spectrometer transmits 60% of the incident radiation. From these number we find the conversion efficiency for argon into the 170 Å to 300 Å band, at optimal pulse width, to be $\sim 1\%$. There is an uncertainty of

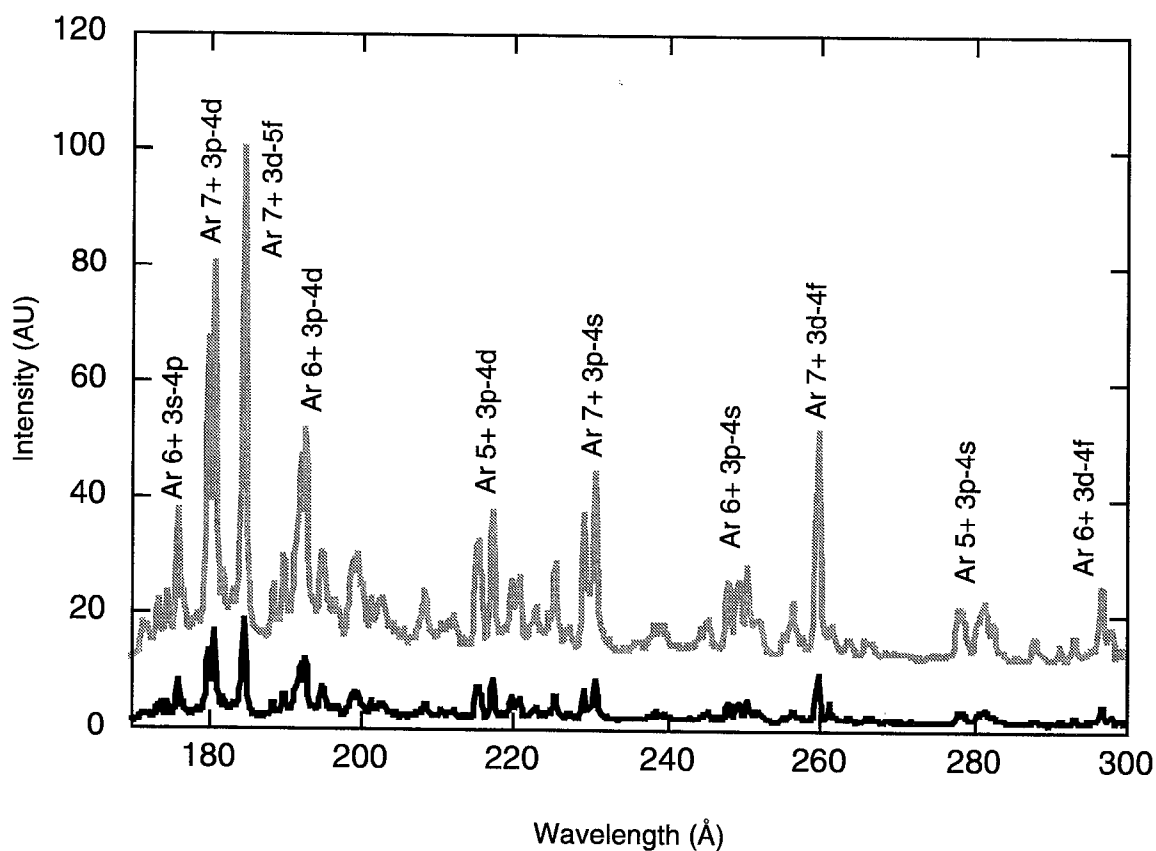
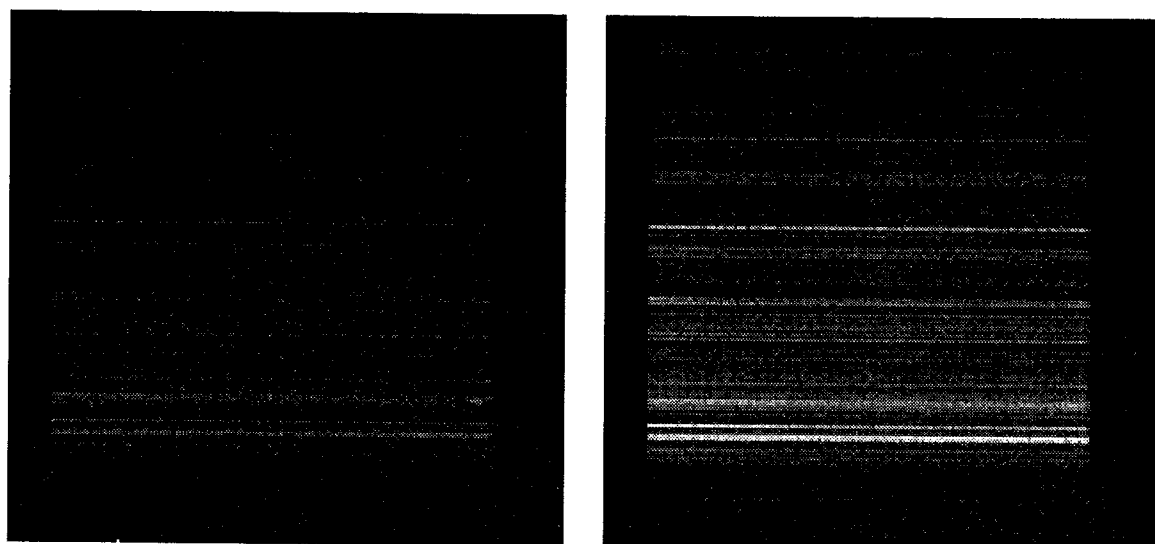


Figure 4.10: Argon spectra at 600 psi. The spectra on the left is for a 50 fs pulse and the one on the left is for a 900 fs pulse. The input energy is 5.4 mJ for both spectra. The graph shows a partial line out of the spectra with some main lines identified. The lower trace corresponds to the 50 fs pulse and the upper one the 900 fs pulse. The upper trace has been offset 10 AU for clarity.

about a factor of 2 since we do not have specific calibrations for the equipment used and we are using the manufacturers typical numbers; ideally the entire spectrometer and detector system would be calibrated either with synchrotron radiation or calibrated photodiodes. As we decrease the pulse width from the optimal, the overall conversion efficiency drops. However, if we take into account the change in absorption, we find that the percentage of the absorbed energy which is converted into x-ray emission remains constant.

We see the spectra for 200 psi Xe in Fig. 4.11. The intensity in vacuum for the 50 fs pulse is 1.9×10^{17} W/cm² for the spectra on the left and for the one on the right it was 2 ps, corresponding to 4.8×10^{15} W/cm². In this case the emitted radiation increased by 600%. The conversion efficiency into this band is comparable to the previous case of argon. There should be substantial emission below the 170 Å cutoff, but our diagnostics were not set up to observe it.

These data all imply that when the absorption increases, the x-ray emission increases along with it. To verify this we measured the spectra and the absorption simultaneously (Fig. 4.12). The x-ray yield tracks the absorption very closely. By adjusting the pulse width we can control the conversion efficiency into soft x-ray energy. This is an attractive technique for source development, since a brighter source can be produced without increasing the laser energy.

4.3.4 Variable energy

Since we are keeping the energy constant in these experiments, the intensity increases as we shorten the pulse. It has been previously observed, using a 2 ps pulse, that as the laser intensity increases, the absorption saturates and eventually decreases.²³ To see if the increasing intensity was responsible for the decrease in absorption at the shortest pulses,

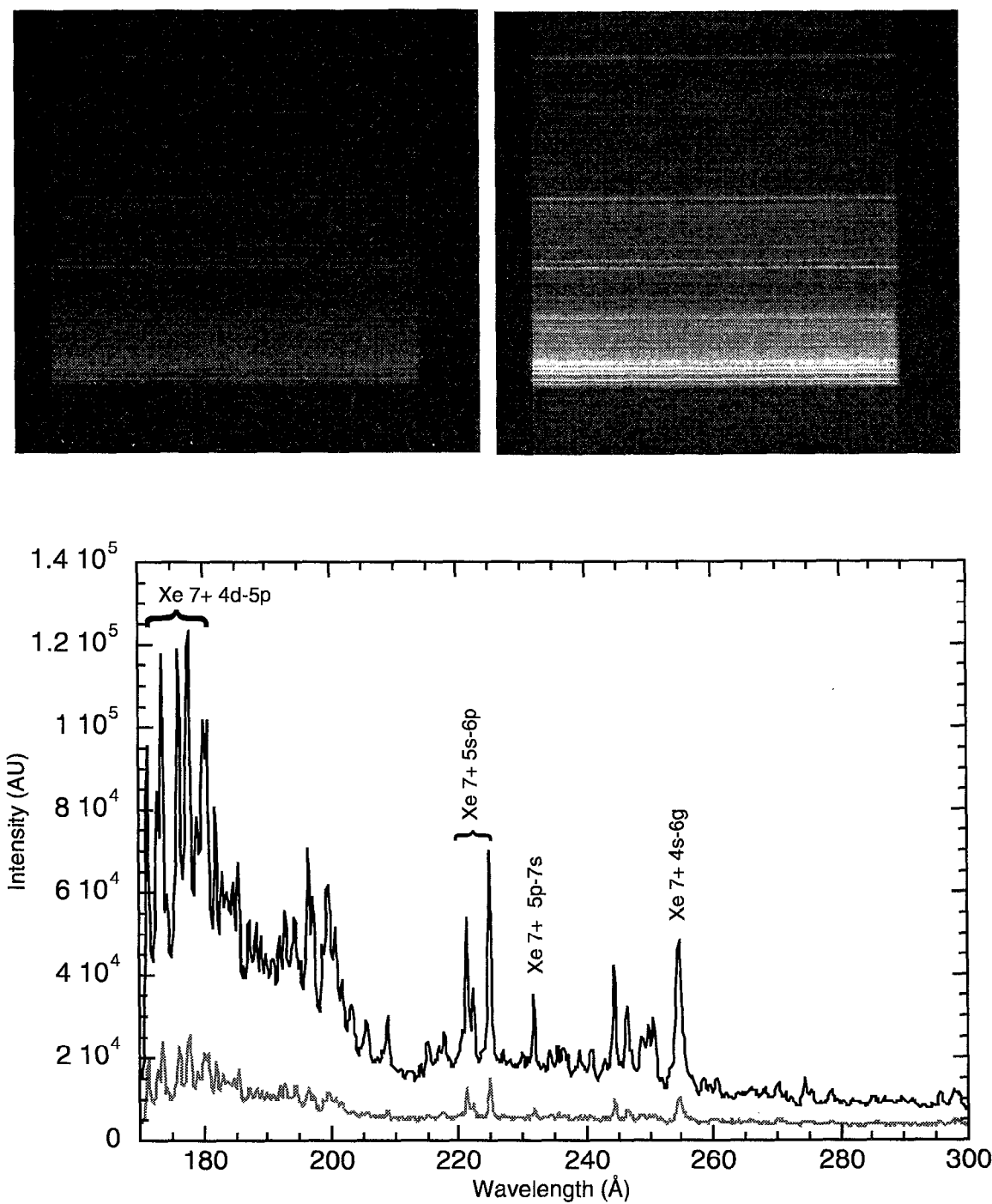


Figure 4.11: Xenon spectra at 200 psi. The spectra on the left is for a 50 fs pulse and the one on the right is for a 2 ps pulse. The input energy is 5.4 mJ for both spectra. The graph shows a partial line out of the spectra with some main lines identified. The lower trace corresponds to the 50 fs pulse and the upper one the 2 ps pulse. The traces are on the same scale.

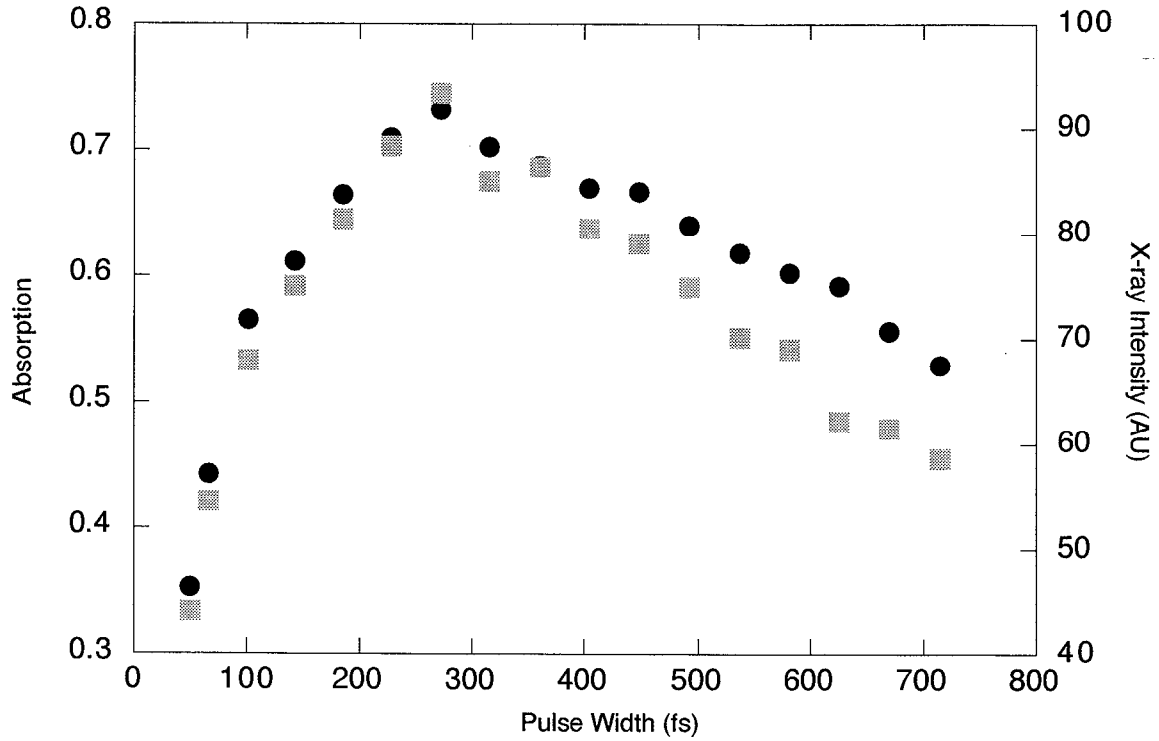


Figure 4.12: Absorption (circles) and x-ray intensity (squares) from 300 psi Ar.

we measured the absorption of laser light as a function of intensity, keeping the pulse width constant and varying the input energy. The shortest pulse of 50 fs was used since this produces the highest intensities and would therefore cause the most saturation. The results of these experiments are shown in Fig. 4.13. Over the intensity range in which these experiments were performed, the absorption is a monotonically increasing function of the laser intensity, clearly indicating that it is the change in pulse width and not the change in intensity which is responsible for the results seen in section 4.3.

When we use a long pulse, shown in Fig. 4.14, the absorption is also increasing over our intensity range. The behavior here, however, is different from the 50 fs case. We see absorption at much lower intensities. Absorption is seen down to 2×10^{13} while, with a 50 fs pulse, the absorption is down below 10% by 6×10^{16} . These data are similar to what has

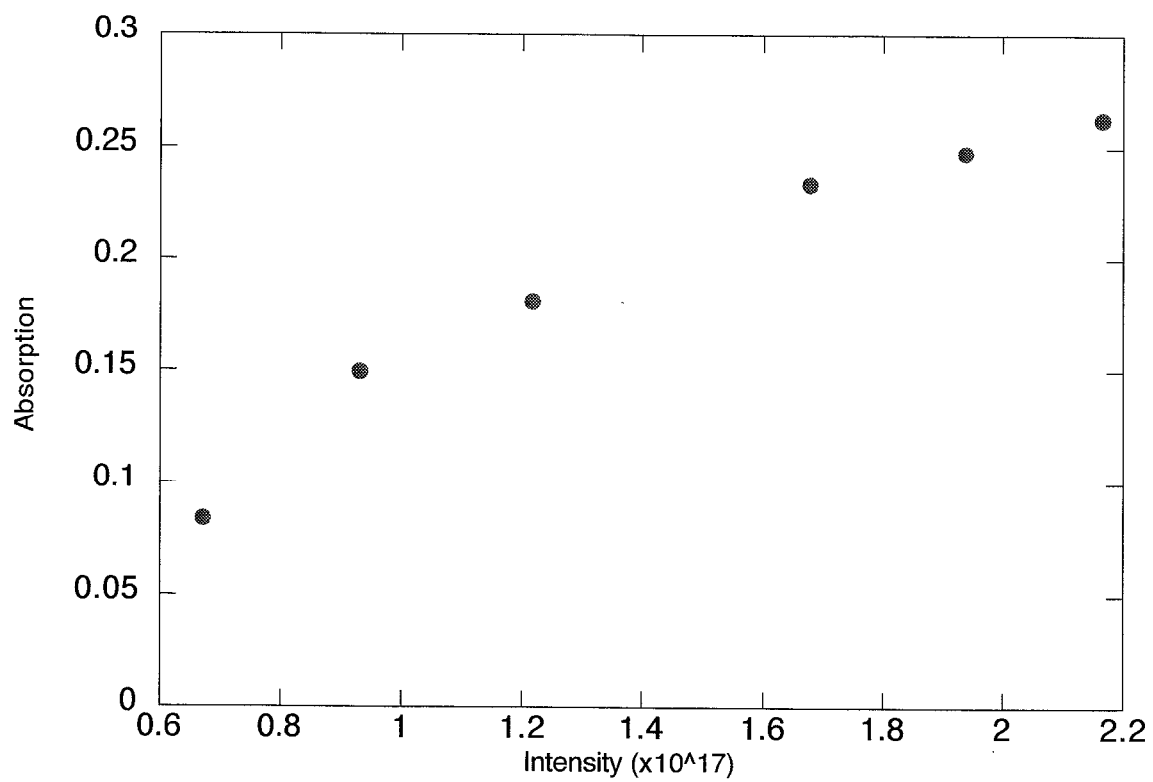


Figure 4.13: Absorption as a function of intensity from 190 psi Xe. Pulse width was 50 fs.

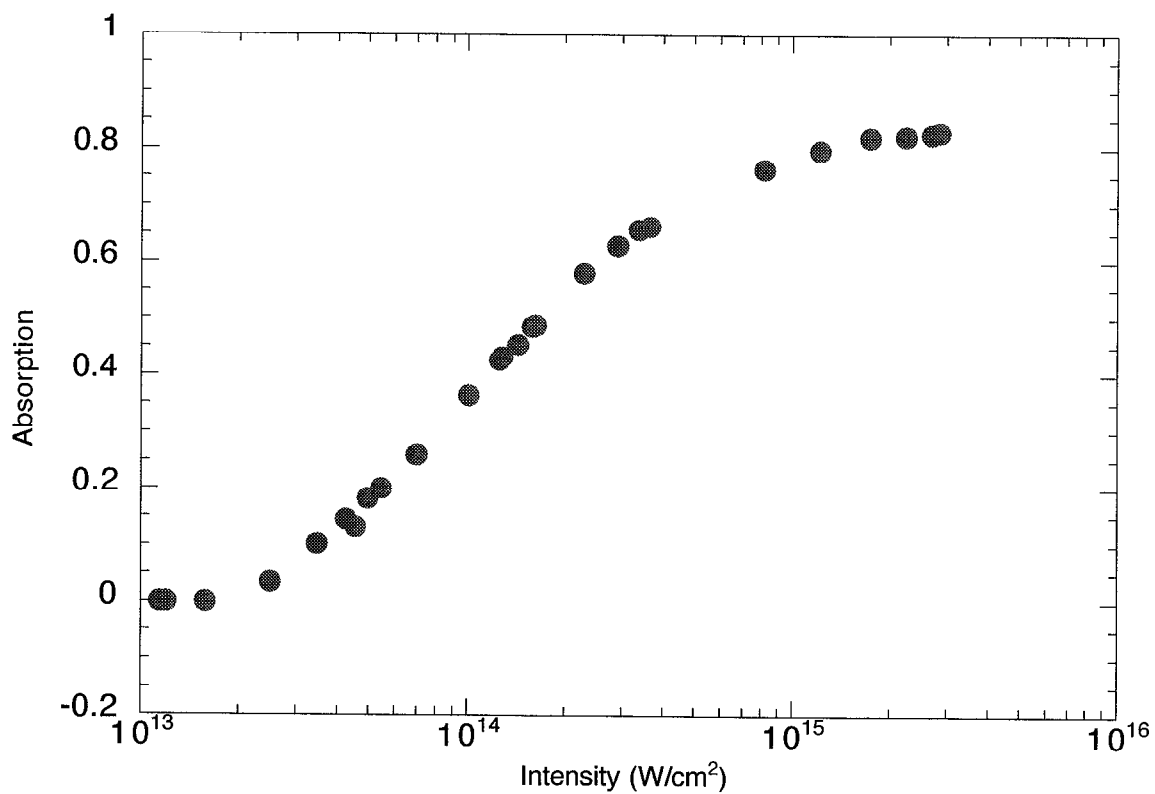


Figure 4.14: Absorption as a function of intensity for 190 psi Xe. Pulse width was 1.2 ps.

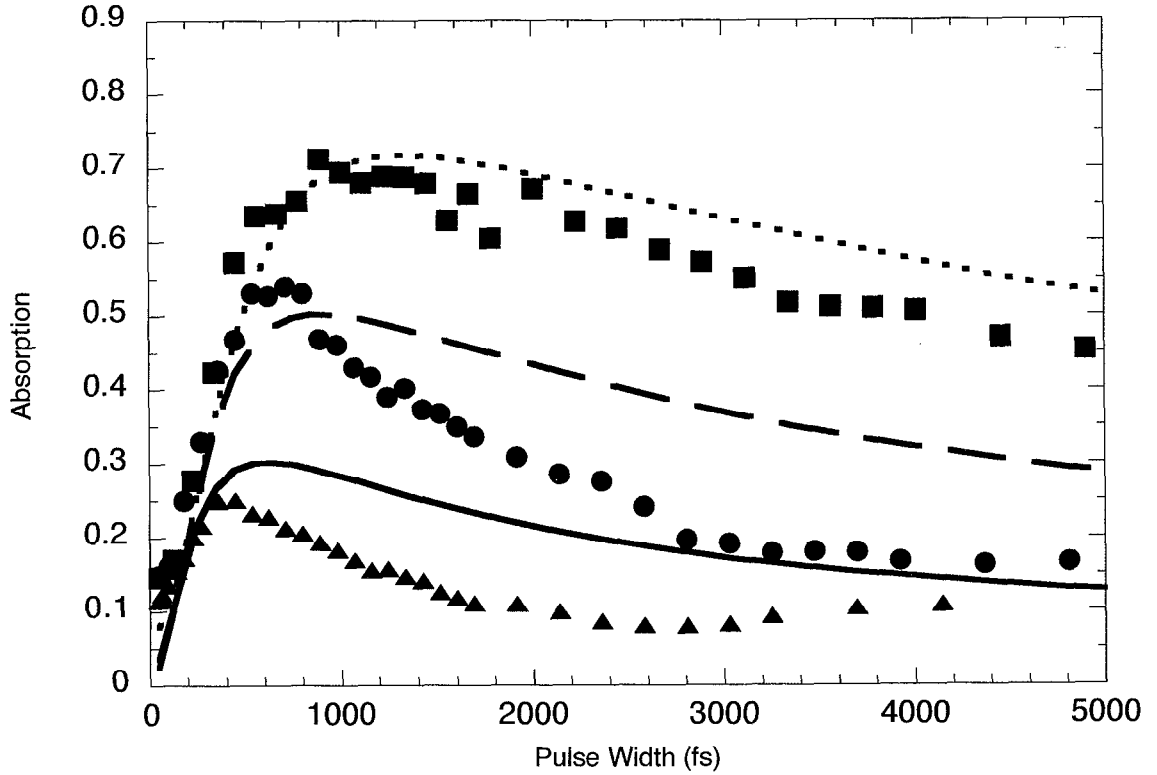


Figure 4.15: Model calculations for variable pulse width data in Xe. The lines are calculated values for 50 (solid), 100 (dashed), and 200 (dotted) psi. The calculations are overlaid on the data from Fig. 4.7

been previously observed with picosecond pulses.²³

4.3.5 Modeling

To further understand the interaction we applied the model discussed in chapter 3 to the entire jet. The jet was divided into slices for purposes of computation. The incident electric field was then applied to a sample cluster in the first slice, and the computation described in chapter 3 was performed. Each timestep, the energy absorbed was multiplied by the number of clusters in the slice and subtracted from the incident energy contained in the timestep. Once the pulse has propagated through the slice, the modified laser electric field was applied to the next slice. This process was repeated until the laser has passed through the entire jet. In our experiments the Rayleigh range was smaller than the jet length. We accounted

for this by adjusting the beam waist through the jet, based on a gaussian beam propagating through focus with a $14\ \mu\text{m}$ waist. The code was run for several intensities and then these were used to integrate over the actual intensity distribution in the focal spot. Summarizing from chapter 3, the overall model considers a uniform density cluster plasma, taking into account tunnel and collisional ionization, ATI and inverse bremsstrahlung heating, along with the hydrodynamic and Coulomb explosion aspects of the expansion.

The distribution of cluster sizes in the jet may effect the calculation. Each cluster size will reach peak absorption at a different pulse width. To account for this we ran the code for several cluster sizes and then took a weighted average. While we do not know the exact distribution, previous work in hydrogen⁹⁴ shows an asymmetric distribution biased toward larger clusters. We used a superposition of a gaussian distribution with a FWIIM equal to the average cluster size and an exponential distribution producing a tail of large clusters.

The computational results are shown in Fig. 4.15. While the code does not produce an exact fit, the agreement is acceptable for a simple model of this nature. All of the curves show the basic features of a fast rise to a peak and then a slow fall as the pulse width increases. As the cluster sizes get larger, the peak absorption moves to longer pulse widths, just as predicted by Eq. 3.67. The peak absorption also gives reasonable agreement between model and data.

The most troubling disagreement is that the code predicts a much slower fall off than was seen in the data. In this regime a significant portion of the laser pulse interacts with clusters after they hit resonance. We saw in chapter 3 how the clusters begin to expand rapidly after the resonance. We will begin to transition from cluster behavior to bulk plasma behavior in this regime. The code does not account for this. Once we form a bulk plasma the Mie code will no longer accurately model the absorption. Additionally,

nonlinear propagation effects in the plasma, which may occur at these high intensities, are not considered.

4.4 Two-pulse experiments, single time delay

The variable pulse width experiments indicated that resonance was playing a major role in cluster interactions. One complication of these experiments was the fact that the laser pulse is continuous while the cluster is expanding to the resonance condition. The dynamics of the laser interaction with the cluster target during this expansion time will be convolved with the effects of the resonance. This complicates the analysis of the experiment.

A pump-probe style experiment would lend itself to simpler analysis. Figure 4.16 shows this experiment. It is probing the same effect as the variable pulse experiments, however, now we use two short 50 fs pulses. A small pulse is placed in front of the main pulse. The small pulse starts the cluster expanding. If there is a small delay (top) the plasma is overdense when the main pulse arrives and absorption is low, similar to the case of no prepulse. If it arrives when the plasma is at the resonance condition (middle), absorption is much higher than it would be without the prepulse. If the delay is too great (bottom), the cluster density is low and we expect the absorption to be small.

4.4.1 Experimental setup

A simple way to create the two pulses for this kind of experiment is to pass the beam through an optic with a hole in the middle of it. Shown in Fig. 4.17, the part of the beam going through the hole will be ahead of the rest of the beam since it does not see the larger index of refraction in the optic. This technique eliminates any alignment problems one may have if they split the beam in two and then recombine the two beams after each has gone

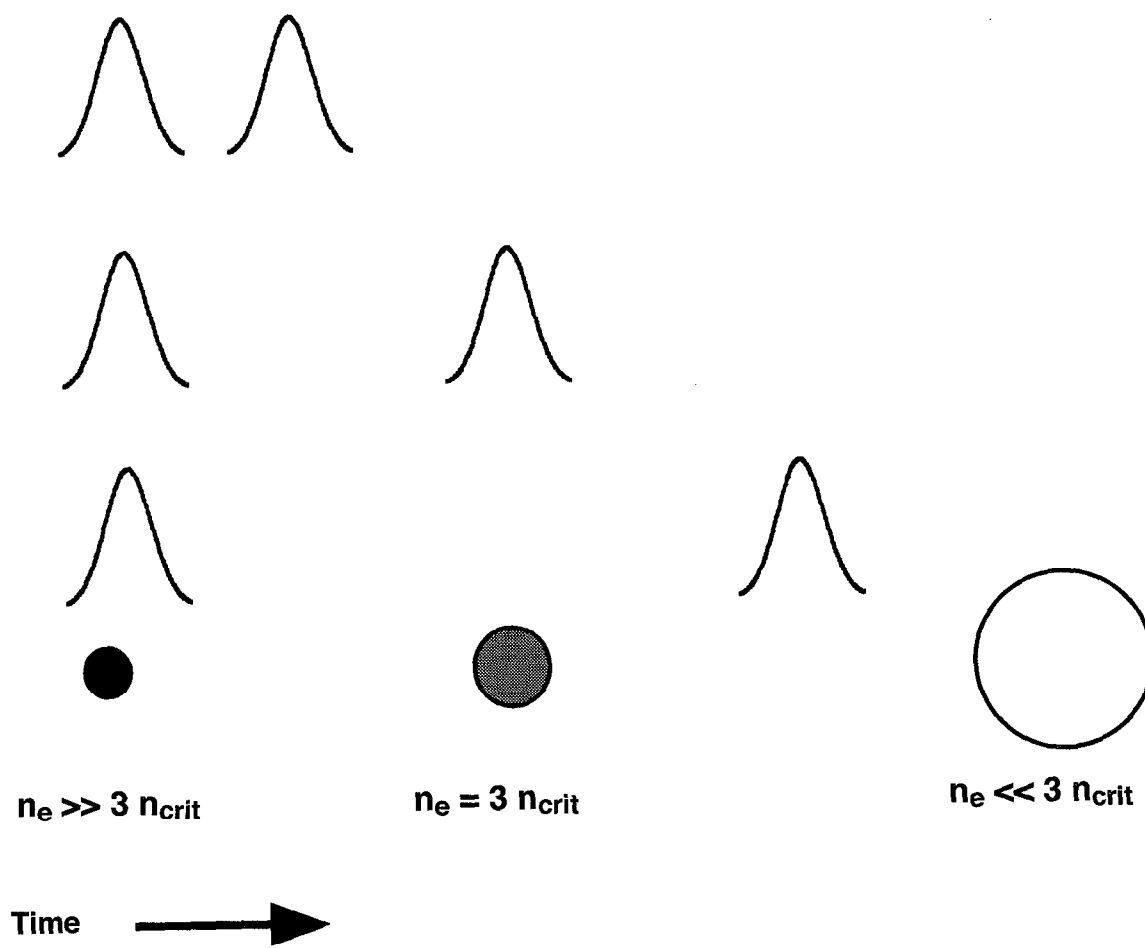


Figure 4.16: Experimental concept for pump-probe experiments.

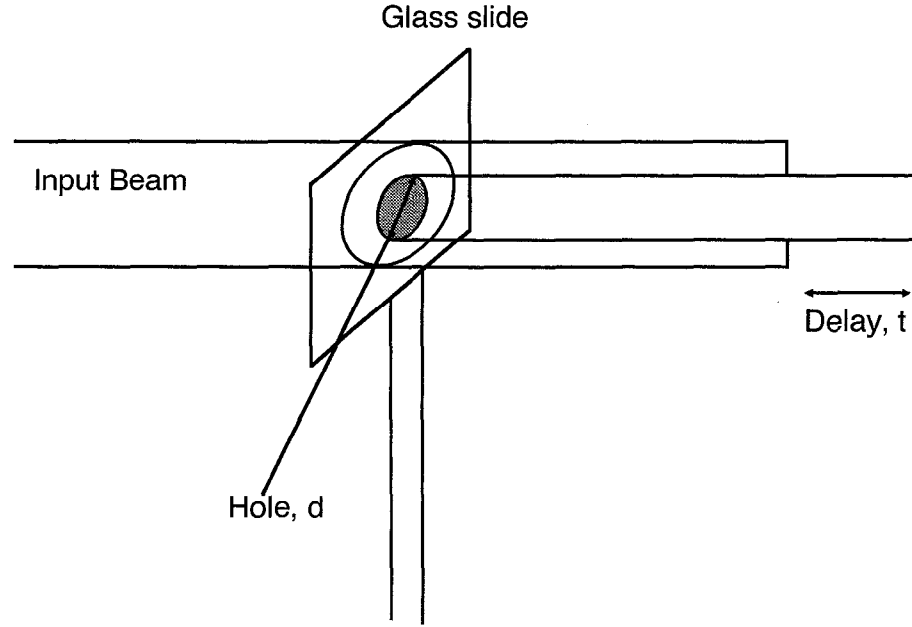


Figure 4.17: Experimental setup for pump-probe experiments.

through a different path length. The delay induced by the optic will be

$$\tau = (n - 1) \frac{t}{c}, \quad (4.5)$$

where n is the index of refraction in the optic, t is the thickness of the optic, and c is the speed of light in vacuum. We knew from the previous experiments that the delay would have to be on the order of 100's of femtoseconds. In order to achieve this, the optic needs to be about $100 \mu m$ thick. Although standard laser optics are not found this thin, microscope slide cover glass of this thickness can be purchased.

We had two hole sizes (.8 and 1.2 cm) ultrasonically drilled in cover glass to provide our delay. These could be inserted and removed from the laser beam after the compressor. The absorption was measured with the same setup described in section 4.3.1. We could also insert cover glass with no hole in it so that we could demonstrate that it is the prepulse

Table 4.1: Data for prepulse experiment using an optic with a hole to generate the delay. Target was 300 psi argon.

Optic thickness (mm)	Delay (fs)	Hole size (cm)	Total absorption
.130	220	no hole	.19
.130	220	.8	.43
.130	220	1.2	.37
2	3300	1.0	.19

and not the cover glass itself that is causing the effect.

4.4.2 Experimental results

Table 4.1 shows the data from this experiment. With only the cover glass there is no enhancement of the absorption and only 19% of the laser energy is absorbed. The .8 cm hole creates a prepulse containing 14% of the energy. This causes the overall absorption to more than double. If we use a larger hole we create a larger prepulse, 33% in this case. The absorption goes down since the delayed pulse, which has the higher absorption, is now smaller. We can calculate the absorption of the delayed pulse since we know only 19% of the prepulse is absorbed. If we do this, we find that for the small hole 47% of the main pulse is absorbed, while with the large hole 46% is absorbed. The difference in the prepulse intensity is small, so the clusters expand in the same manner for both cases. The main pulse comes at the same point in the expansion and the absorption is more or less the same for both cases.

We also used a thick optic to delay the main pulse to long after the clusters go through the resonance condition. In this case the total absorption was only 19%. Both the prepulse and the main pulse are poorly absorbed. The clusters have expanded into a low density bulk plasma by the time the delayed pulse arrives and we see weak coupling with the laser.

4.5 Two-pulse experiments, variable time delay

The success of the glass slide experiments encouraged us to do an actual pump probe style experiment. This way we can continuously change the delay between the main pulse and the prepulse, allowing us to probe the expansion process.

4.5.1 Experimental setup

The setup is similar to Fig. 4.5. The compressor is set to the shortest pulse and a delay leg is inserted (lower left corner). This unit consists of a beam splitter which directs the pulse down two separate paths one of which has an adjustable length. The beams are then recombined with another beam splitter and sent to the expanding telescope.

In order to check alignment a far field diagnostic was set up and used to be sure the beams overlap at the focus. When the alignment was correct we could easily see an interference pattern when the pulses overlapped in time. The input and output energies were measured in the manor described in section 4.3.1. By changing the input polarization to the beam splitter we were able to adjust the relative magnitude of the two pulses. We had previously determined that the polarization does not effect the absorption of the laser pulse.

4.5.2 Experimental results

Figure 4.18 shows absorption as a function of probe delay for different backing pressures of xenon. The peak intensity in vacuum for the pump was 1.6×10^{16} W/cm² and for the probe it was 1.6×10^{17} W/cm². The pulse length was 50 fs. At very small delays, absorption is low; the cluster has little time to expand and the second pulse arrives long before the electron density reaches the resonance condition. However, as we increase the delay, absorption

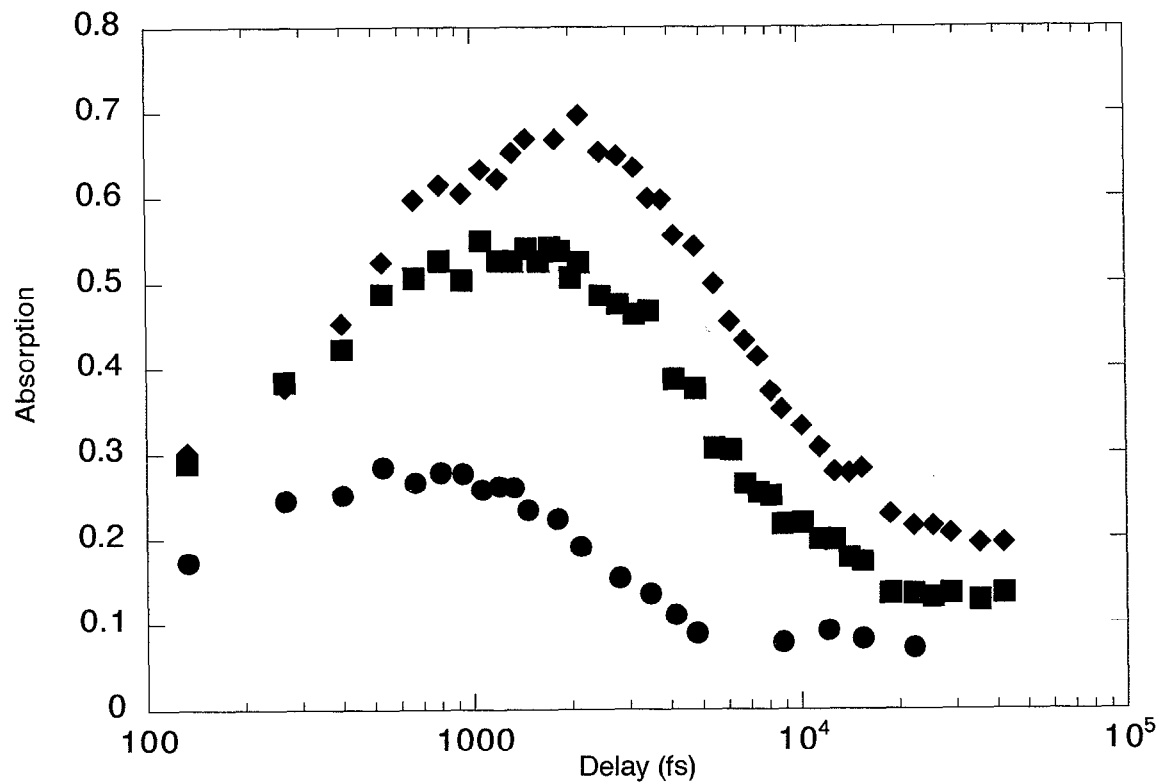


Figure 4.18: Absorption measurements for pump-probe experiments. The target was xenon at 50 (circles), 100 (squares), and 150 (diamonds) psi. The peak intensity in vacuum for the pump is 1.6×10^{16} W/cm² and for the probe it is 1.6×10^{17} W/cm². The pulse length was 50 fs.

increases. The longer delay allows the electron density to be near the resonance condition when the pulse arrives, greatly enhancing the absorption of laser light. For longer delays, the cluster has continued to expand and the probe pulse is poorly absorbed by the, now underdense, plasma. Eventually, we reach a condition in which the local atomic density within a cluster equals the average atomic density in the jet. At this point the clusters are fully disassembled and play little role in the interaction. The absorption approaches a constant depending only on the average gas density.

Similar to the variable width experiments, larger clusters have broader resonance peaks. If we measure the width of the resonance at 70% of the maximum absorption in xenon we find that it is about 2, 3 and 5 ps for 50, 100, 150 psi backing pressures respectively. The larger clusters have lower density rates of change and are near resonance for a longer period of time, increasing the absorption of laser light. A smaller rate of change in density would also indicate a longer disassembly time. The three curves flatten out, indicating full cluster disassembly, after different delays with larger clusters taking longer periods of time to reach this point. The largest clusters are fully disassembled after 35 ps.

We see similar behavior in argon. The delay for peak absorption is about 400 fs for 300 psi, while it is slightly over 1 ps at 600 psi. The lighter argon ions move faster than xenon and hence the clusters expand faster, leading to shorter delays. Interestingly, the absorption for the fully disassembled clusters ($> 10^4$ fs) is higher for argon (Fig. 4.19) than it is for xenon (Fig. 4.18). To first order one would expect the electron density to be about the same for both of these systems, the higher pressure of the argon being canceled by the larger number of electrons in xenon. However, the ionization is tied to collisions in the clusters before they are disassembled. The ion density is about 50% greater in argon than in xenon. This will produce more collisional ionization and a greater electron density in

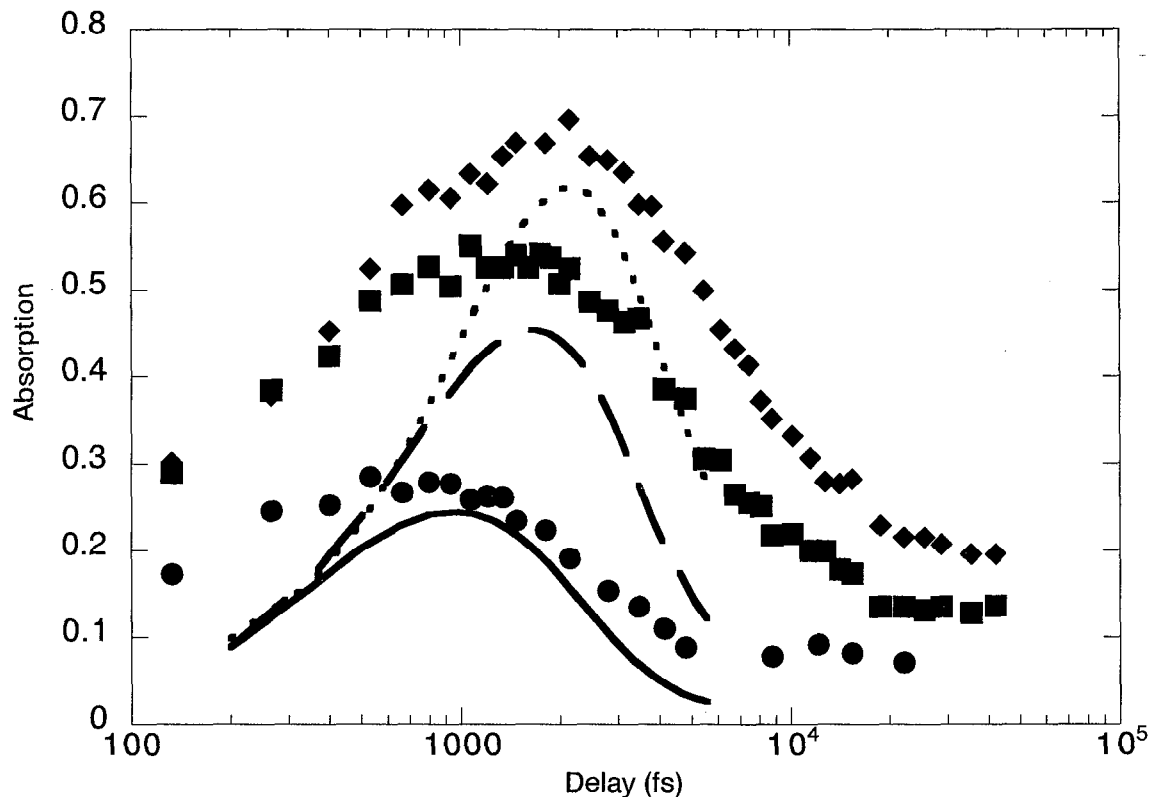


Figure 4.21: Theory for data from Fig. 4.18. The lines show the results of computer modeling for 50 (solid), 100 (dashed), and 150 (dotted) psi.

4.5.3 Modeling

We modified the code used in the variable pulse experiments for the pump-probe experiments. The incident electric field was changed from a single pulse with variable width, to two discrete pulses of 50 fs width. The results of this modeling is shown in Fig. 4.21. We see the trend of larger clusters requiring longer periods of time to expand to resonance. The calculated peaks are somewhat narrower than experiment. This discrepancy may be due to our incomplete knowledge of the exact cluster distribution in the jet. Since larger clusters will require more delay and smaller clusters will require less, a broader distribution will broaden the widths of the model curves. Soft x-ray scattering, using either harmonics or synchrotron radiation, could be used to find out more precise information about the

actual distribution (the wavelength must be on the order of the cluster size to get this information). However, the main problem is most likely the limitations of the code itself. The uniform density cluster model does not fully describe the hydrodynamics involved in the expansion process. As density gradients develop within the expanding cluster the resonance will spread out and not be so distinct; this will broaden the calculated curve. While the intensity is not high enough to see significant $\mathbf{J} \times \mathbf{B}$ heating,⁹⁵ vacuum heating⁹⁶ may contribute to the absorption. The fluid model assumes small oscillations. In reality, some electrons will be pulled out of the cluster and then reenter the cluster on the next half-cycle, depositing energy. Kinetics modeling would have to be done to do the calculation, but this effect should be maximum for short pulse lengths (high intensities) and sharply bounded overdense plasmas.

4.6 Conclusions

The data in this chapter shows the behavior expected from the plasma model for cluster interactions; resonance behavior dominates and we see enhanced absorption when the cluster is given some time to expand to resonance before the bulk of the laser energy interacts with the target. For variable pulse width experiments the optimal pulse width is from 300 fs to 1.2 ps, depending on atomic species (lighter elements have smaller optimal pulse widths) and cluster size (larger clusters have larger optimal pulse widths) Clearly both pulse length and laser energy, not just intensity, control the dynamics of laser interactions with clusters.

This phenomena can also be investigated with a pump-probe style experiment. The same behavior is observed where a certain delay is needed to allow the cluster to expand to resonance. The optimal delays ranged 500 fs to 2.1 ps.

We have also seen that we can effect the conversion efficiency of the laser into soft x-ray

energies. This can increase the brightness of small soft x-ray sources, without increasing laser energy, possibly making XUV plasma sources for lithography more economical.

Chapter 5

Mie Scattering Experiments

As we saw in chapter 3, Mie scattering theory gives the total field both inside and outside of the sphere. The field inside leads to the absorption which we measured in chapter 4. Laser light will also scatter from the cluster target during the interaction. If we see a resonance in the absorption, we would expect to see a resonance in the scattering.

Normally Mie scattering is done with low irradiance such that the laser does not change the state of the target. In our case the clusters are changing rapidly while the laser interacts with them. This will greatly complicate the calculations; both the index of refraction and the radius will be changing. However, the same physics will apply to this dynamic Mie scattering and we can use our code, discussed in chapter 3, to model the interaction.

5.1 Experimental setup

The experimental setup is basically the same as in Fig. 4.5. In this case, the spectrometer was removed and a large $f/2.3$ lens is used to collect the 90° scattered light, that is the light scattered perpendicular to the direction of propagation. The signal was detected with a silicon energy probe. An 810 nm bandpass filter, with a 10 nm FWHM bandwidth, was

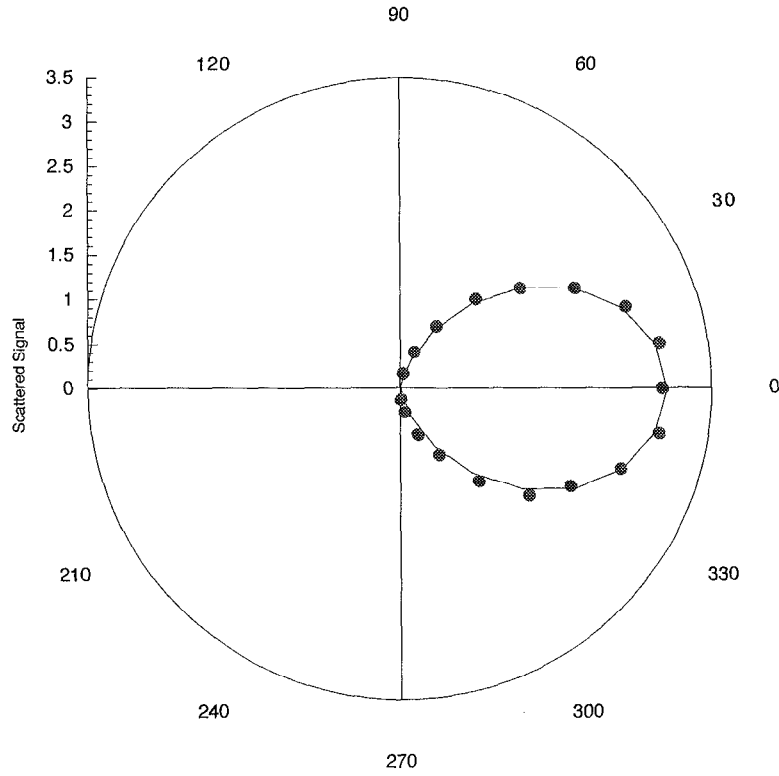


Figure 5.1: Emission pattern for scattered laser light. The target was argon at 600 psi. The intensity was $1.3 \times 10^{16} \text{ W/cm}^2$. The pulse width was 800 fs.

placed in front of the energy head to filter both room light and most plasma light. A $\lambda/2$ waveplate before the expanding telescope allowed us to rotate the polarization before the beam enters the chamber. All measurements are 50 shot averages.

5.2 Emission pattern

We first examined the radiation pattern to be sure that the plasma dynamics were not interfering with the scattered signal. By rotating the waveplate we can map out the scattered intensity with respect to the laser polarization. The characteristic of Mie scattering, in the Rayleigh limit, is a dipole radiation pattern. The radiation pattern for 600 psi argon is shown in Fig. 5.1. The $\cos^2(\theta)$ dependence is exactly what we expect.

To be sure plasma light was not interfering with the measurement, we put a filter to

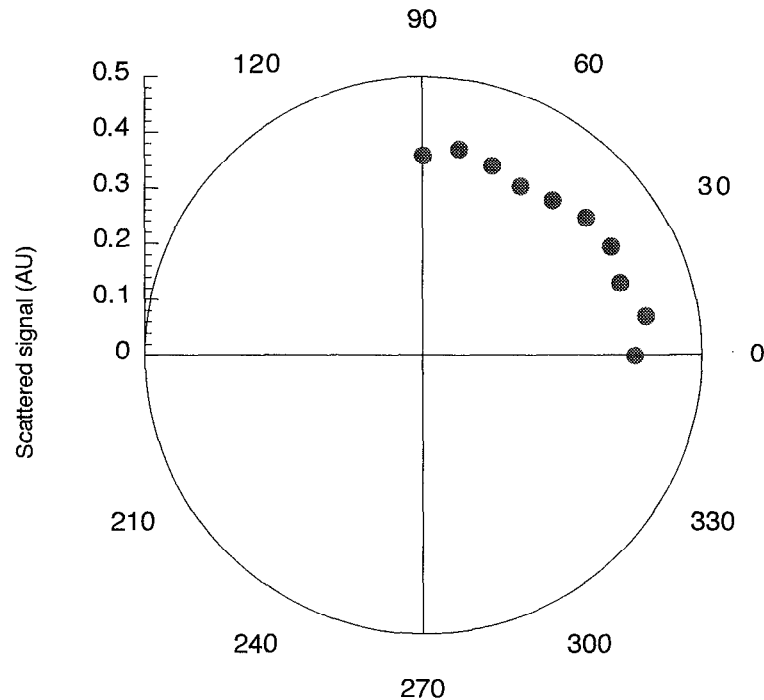


Figure 5.2: Emission pattern for plasma light. The target was xenon at 200 psi. The intensity was $1 \times 10^{16} \text{ W/cm}^2$. The pulse width was 1.2 ps.

block the scattered laser light in front of the detector. We simply used a dielectric mirror which reflected the band from about 770-870 nm. The radiation pattern for 200 psi xenon, with the mirror, is shown in Fig. 5.2. Xenon had to be used here in order to produce enough signal to measure. This shows an isotropic radiation pattern which would be expected from plasma light. The difference between the two plots shows that the signal measured in Fig. 5.1 is from scattering and not plasma emission.

5.3 Scattering data

We examined argon and xenon, both of which produced similar results. We observed the scatter perpendicular to the polarization of the incident field. From the previous section we see that this is where the signal is the largest.

The total amount of energy scattered was small. The maximum detected signal was 16

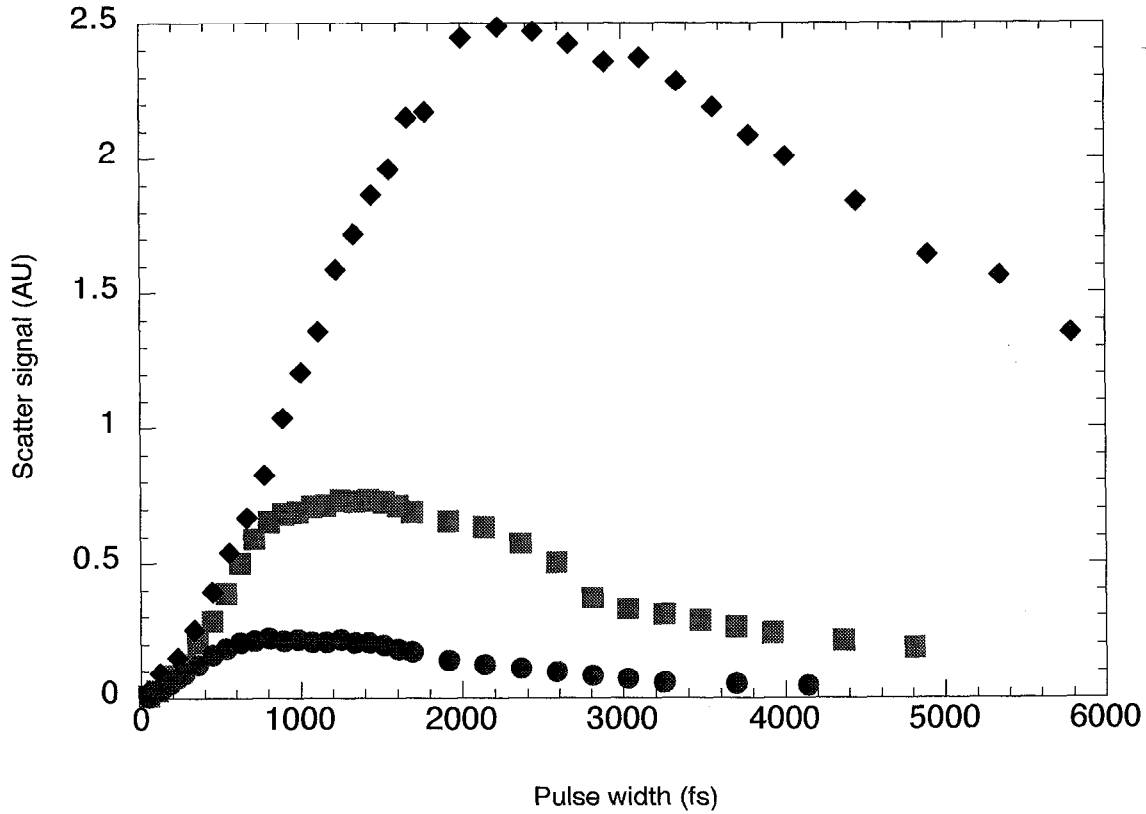


Figure 5.3: Scattering in xenon as a function of pulse width. The input energy was 6.4 mJ which corresponds to an intensity of 2.4×10^{17} W/cm² for a 50 fs pulse. Data for 50 psi (circles), 100 psi (squares), and 200 psi (diamonds) backing pressures are shown.

nJ for 200 psi xenon. The detector could reliably measure 30 pJ, so the measured signal was well above the detection limit.

5.3.1 Scattering in xenon

Figure 5.3 shows the scattered signal from the cluster target for several backing pressures of xenon and many pulse widths. We see the same qualitative features which we saw in the absorption measurements from chapter 4. There is a rapid rise to a peak and then a gradual decrease in signal. Both the magnitude of the signal and the pulse width for peak signal are larger for higher backing pressure.

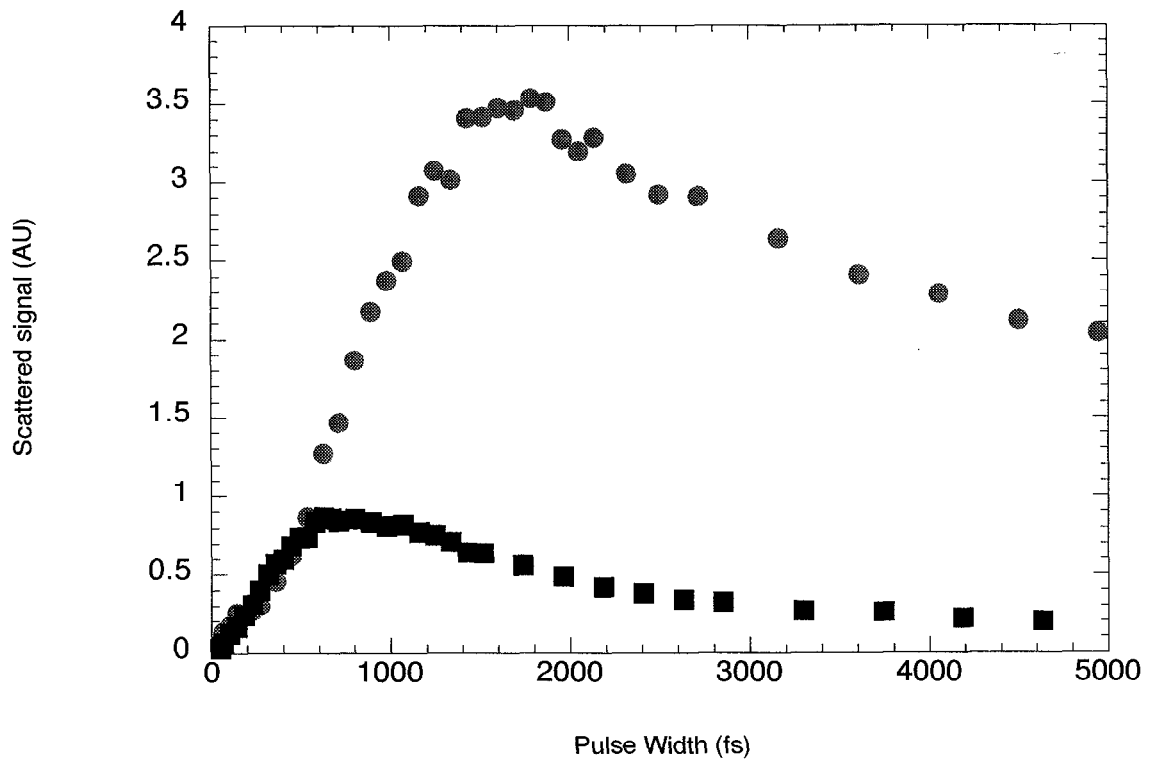


Figure 5.4: Scattering in argon as a function of pulse width. The input energy was 6.4 mJ which corresponds to an intensity of 2.4×10^{17} W/cm² for a 50 fs pulse. Data for 300 psi (squares) and 600 psi (circles) backing pressures are shown.

5.3.2 Scattering in argon

The scattering data for argon are shown in Fig. 5.4. The results are similar to what was seen in xenon. There is a relatively rapid rise, and a gradual decrease after the peak is reached.

5.4 Scattering and absorption

If we compare the scattering (Figs. 5.3 and 5.4) and absorption (Figs. 4.7 and 4.8) data, we see one major difference. The scattering signal peaks at a longer pulse width than the absorption. Initially, it was thought there may be some systematic error causing the difference since the data were taken at different times. Simultaneous measurements were

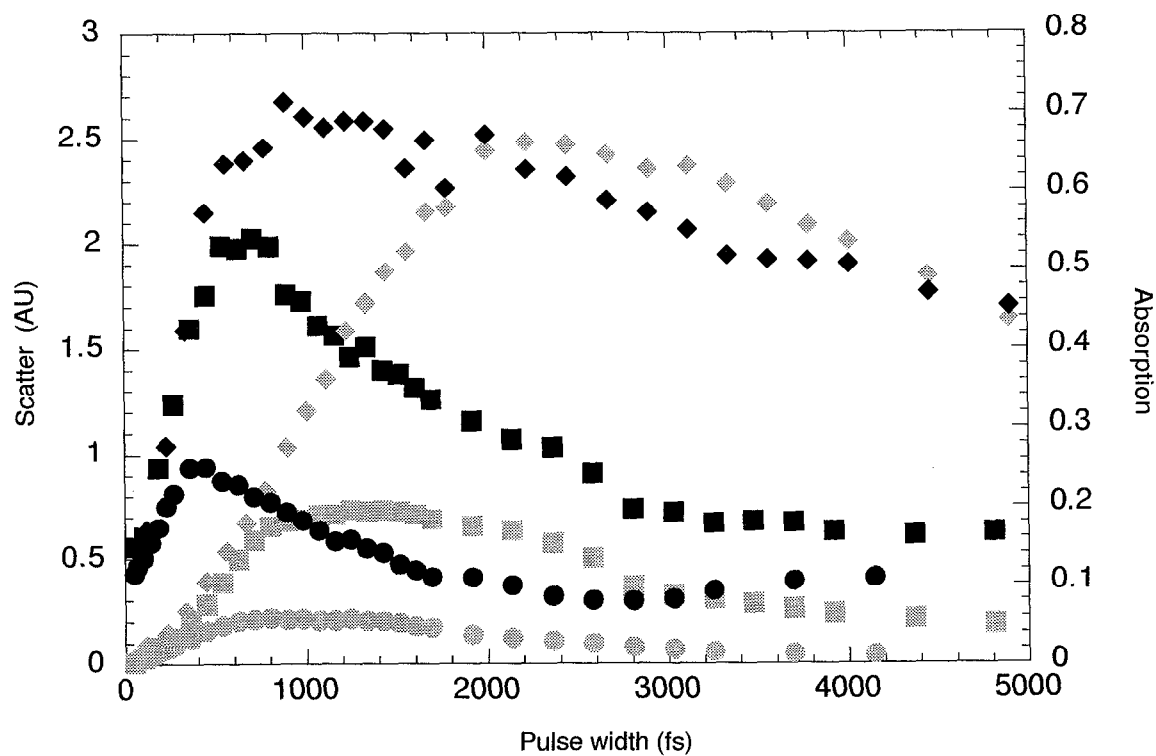


Figure 5.5: Scattering (gray) and absorption (black) in xenon as a function of pulse width. The input energy was 6.4 mJ which corresponds to an intensity of 2.4×10^{17} W/cm² for a 50 fs pulse. Data for 50 psi (circles), 100 psi (squares), and 200 psi (diamonds) backing pressures are shown.

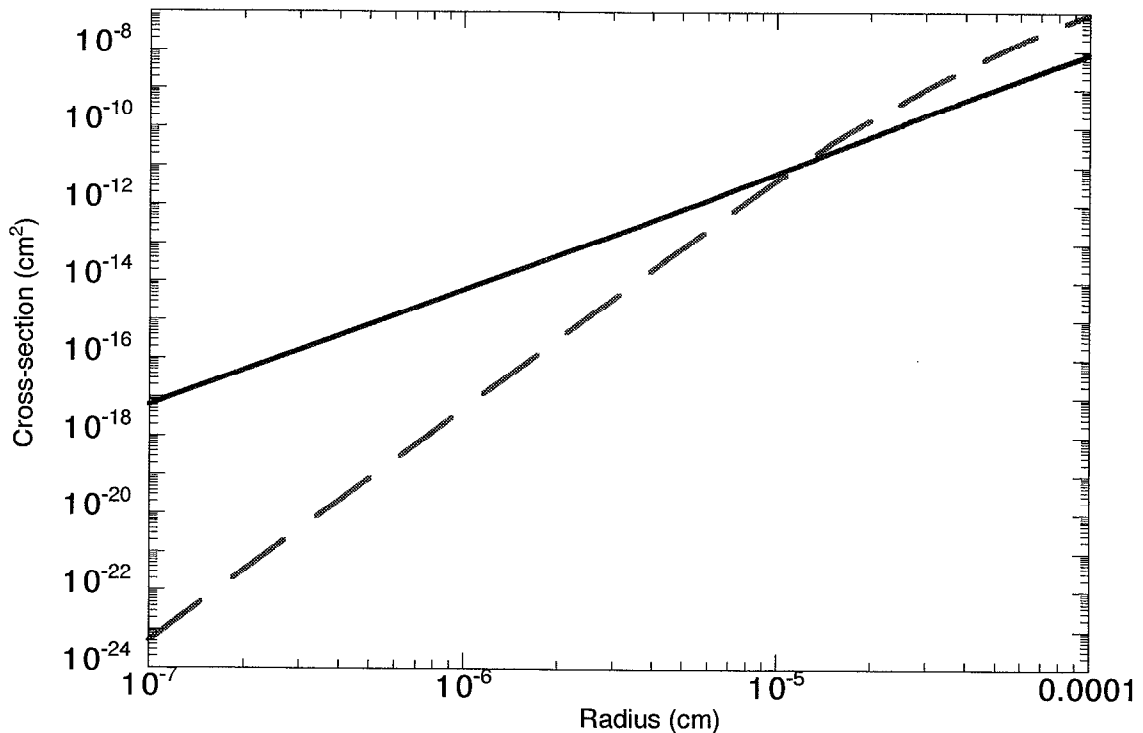


Figure 5.6: Calculated scattering (dashed) and absorption (solid) cross sections from Mie theory. The index of refraction was the same for all radii.

performed for xenon. The results, shown in Fig. 5.5, show the same discrepancy. Hence the difference in pulse width is real and not a systematic error.

This is somewhat of a surprising result. Figure 5.1 showed a dipole nature, indicating small object scattering. In this limit the scattering and absorption cross sections are

$$\sigma_{sca} = \frac{8\pi}{3} k^4 r^6 \left| \frac{\epsilon - 1}{\epsilon + 2} \right|^2, \quad \sigma_{abs} = 4\pi k r^3 \text{Im} \left\{ \frac{\epsilon - 1}{\epsilon + 2} \right\}. \quad (5.1)$$

These are similar in form and, to first order, we would expect to see similar behavior.

While absorption generally dominates for very small particles,⁷⁵ it is well known that as the radius increases the r^6 scaling of the scattering cross section will overcome the r^3 scaling of the absorption cross section (Fig 5.6). This looks like it could be an explanation of the data. With a longer pulse, the resonance will be reached early in the pulse so a cluster will have a larger radius during more of the pulse than it would for a short pulse. However,

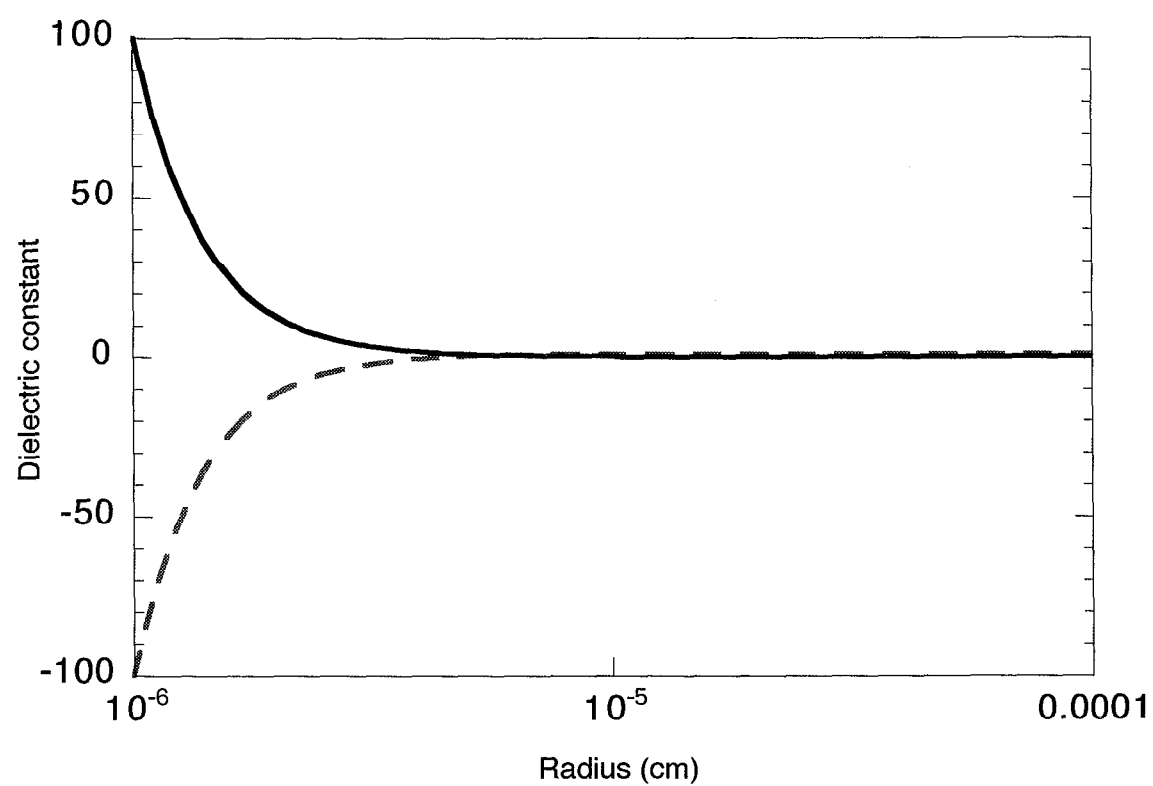


Figure 5.7: Calculated dielectric constant for an expanding plasma sphere. Plot shows both real (dashed) and imaginary (solid) components.

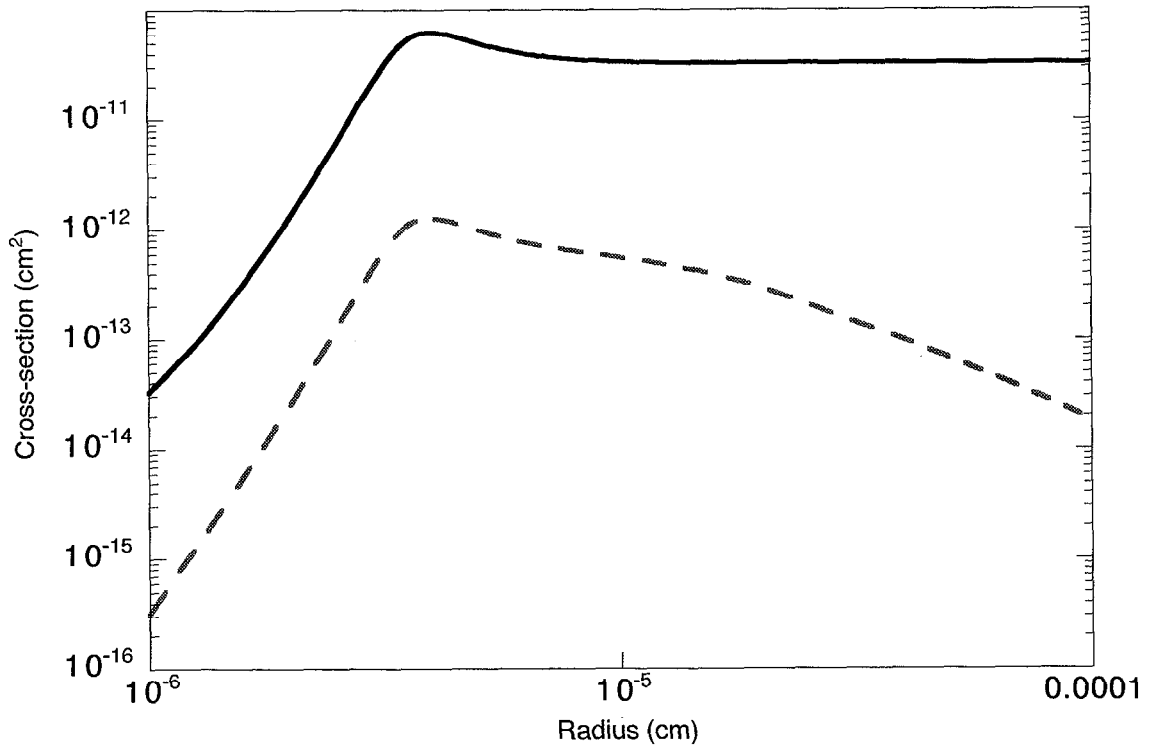


Figure 5.8: Calculated cross-sections for an expanding plasma sphere. Plot shows both absorption (solid) and scattering (dashed) cross-sections.

this scaling holds only for a constant index of refraction. As a cluster expands, the density drops and hence the index of refraction drops. We can rewrite Eq. 3.15 as

$$\epsilon = 1 - \frac{n_0}{n_{crit}} \left(\frac{r_0}{r} \right)^3 \left(1 + \frac{i\nu}{\omega} \right)^{-1} \quad (5.2)$$

where n_0 is the initial electron density and r_0 is the initial cluster radius. This is plotted in Fig. 5.7 for an expanding plasma sphere. Both real and imaginary parts start off very large and then approach their vacuum values. Using the Mie code, we can calculate the cross-sections for a radially expanding cluster using this dielectric constant. Seen in Fig. 5.8, both cross-sections reach their peaks at the same time. Also, while the scattering is less than the absorption, the general shape of the curves are the same.

We can calculate the heating and scattering of a cluster with the full absorption code.

Figure 5.9 shows the calculated scattered signal (as measured in the experiment) along with

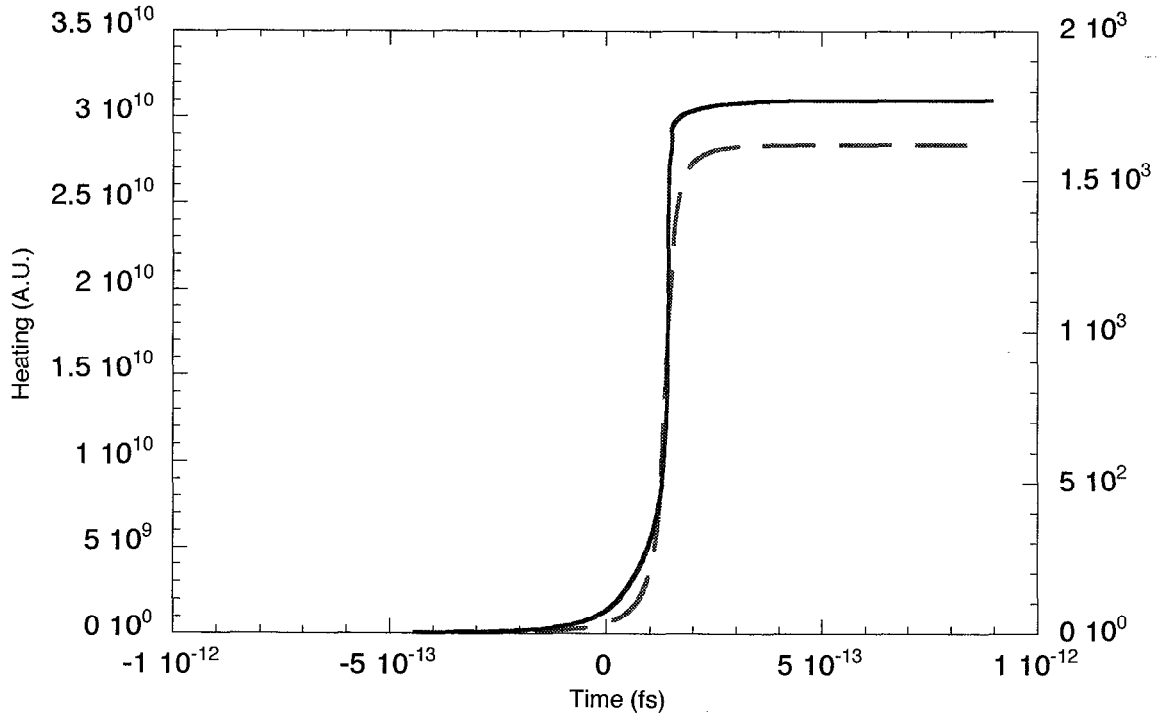


Figure 5.9: Calculated scattering (dashed) and heating (solid) for a 100 Å xenon cluster. The pulse width was 450 fs and the intensity was 4.1×10^{15} .

the heating as a function of time. This calculation shows what we expect from the previous calculations. Both of these show a rapid increase at the same time. This resonant behavior, which we discussed in section 3.2.4, dominates both absorption and scattering.

This leaves the data in Fig. 5.5 unexplained. More experiments in this area need to be done. It would be helpful to perform two pulse scattering experiments. Much as this experiment made the absorption experiments easier to interpret, it can clear up the scattering experiments. This should provide better resolution to see if it is a true shifting of the resonance, or an effect from having significant laser radiation present when we are away from the resonance.

One possible explanation of these data is effects from the ions in the plasma. The Drude model only accounts for the free electrons in the plasma. The ions still have a large number of bound electrons around the nucleus. These are tightly held and one would not

expect this to be a large effect. However, it is possible that electron recombination into outer orbitals are creating effective scatterers.

5.5 Conclusions

Clearly there is a resonance in the scattered radiation. While this is related to the resonance seen in the absorption, the fact that the peaks occur at different pulse widths indicates that there is more happening than a simple model assumes. Calculations show that both absorption and scattering should behave in the same way, and the resonance should be reached at the same time.

We do not know if the scattering data is due to scattered light before the resonance, after the resonance, or if the location of the resonance actually shifts. Further experiments measuring the scattered light in a pump-probe configuration should help determine this and resolve the disagreement between theory and experiment.

Chapter 6

Conclusion and future directions

In the preceding chapters we have seen the results from several different experiments. These data make a very convincing argument for the plasma model of cluster interactions. Resonance effects dominate and are responsible for the gross behavior of the clusters. Though there is some data which cannot be fully explained by the current model, the general agreement with experimental results infers that a modification to the model is required and not a fundamentally different approach.

We have seen that absorption optimizes with pulse width between 300 fs and 1.2 ps. This is dependent on both the size and atomic species of the cluster. Absorption also optimizes for delay between pulses in pump-probe style experiments. Delays are longer than the optimal single pulse widths. This is due to smaller expansion velocities in a pump-probe configuration. Clusters disassemble, expanding from solid density to the average gas density, on a scale of 1–10's of ps.

Perhaps the most important result from this research is that the pulse width of a laser must be carefully considered when designing and analyzing cluster experiments. Results taken with different lasers which have different pulse widths, but the same intensity,⁹⁷

cannot be freely compared; energy and pulse width must be considered independently.

6.1 Future directions

High intensity cluster interactions is still a relatively new field. While the work presented in this thesis answers one question, there are still further questions about the exact dynamics of the cluster expansion. Also, cluster targets are being investigated as possible sources in other applications. We will now briefly discuss some areas for future work.

6.1.1 Computer modeling

The model presented in this thesis is admittedly simple. While it does a good job of predicting the absorption and resonance effects in the interaction, there are some discrepancies between the model and the data.

A first step would be to add bulk plasma effects. In addition to just adding the effects, the code would have to take into account the transition in behavior, as the cluster expands, from individual cluster behavior to a bulk plasma. However, what is really needed to model this problem is a full scale code to solve the hydrodynamic equations of motion coupled with Maxwell's equations. This would have to be done in two dimensions since the electric field breaks the radial symmetry of the cluster. A code of this nature is a daunting task, and would need large scale computer support.

6.1.2 Electron emission

One interesting observation from these experiments is shown in Fig. 6.1. The small spots all over the image were found to be electrons scattering through the 3000 Å Al filter in front of the spectrometer, scattering off the spectrometer optics and finally hitting the CCD

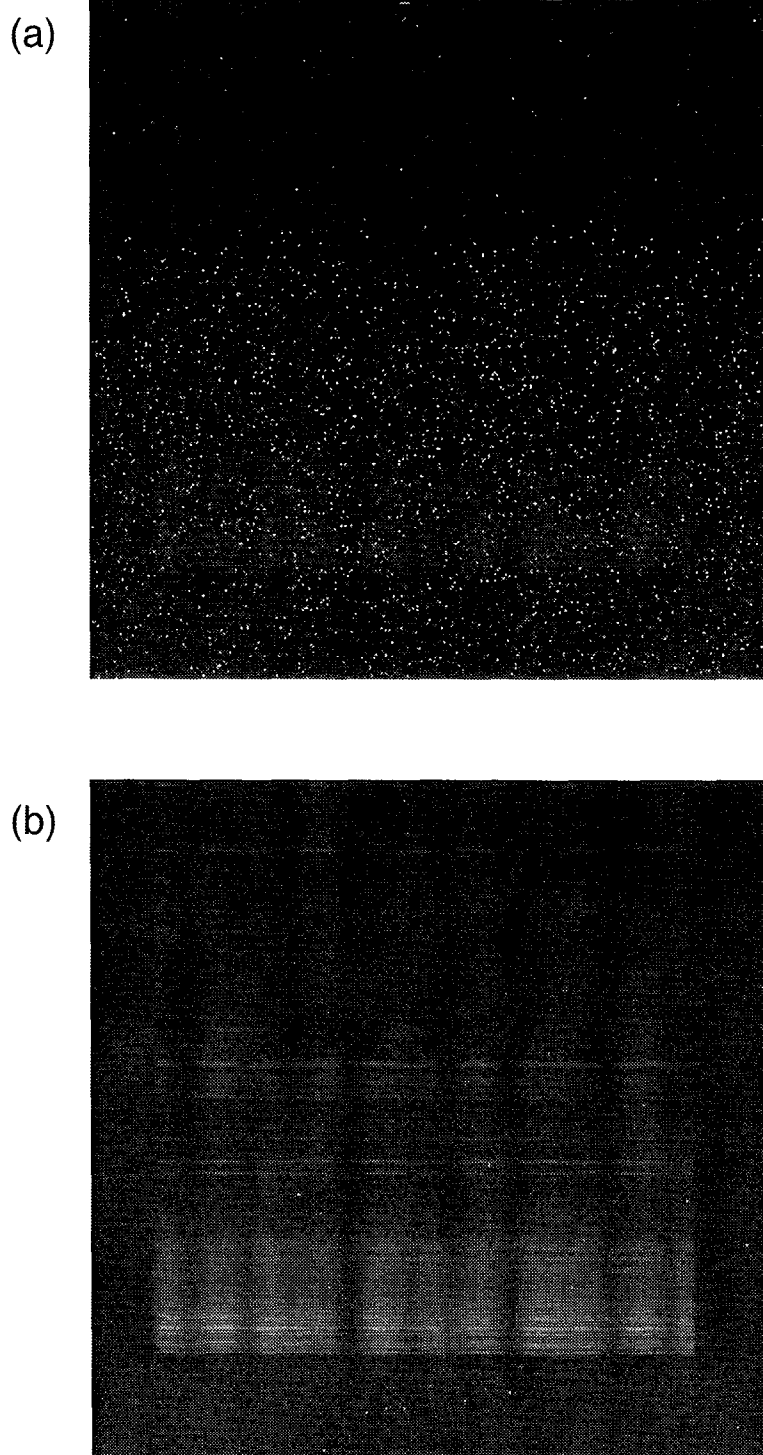


Figure 6.1: Target in both cases is 200 psi Xe. (a) The pulse width was 50 fs. A very dim spectrum is seen under the white spots. The spots are electrons hitting the CCD. (b) The pulse width is 900 fs. The x-ray emission is now much greater, but the electrons have for the most part disappeared. The dark vertical lines are from a grid placed in front of the spectrometer.

camera. In order to have traveled this path the electrons have to have energies of several keV. The interesting thing is that these electrons seem to be produced when absorption is low. When the pulse length is increased from 50 fs, the electron signal rapidly decreases. Possible explanations are that this is caused by an instability at high intensities or actual electron acceleration.⁹⁸ Further work is required to determine the origin of these electrons.

6.1.3 Neutron generation

It was predicted²⁷ that it should be possible to achieve high enough ion temperatures in deuterium clusters to cause thermonuclear fusion. This reaction ($D+D \rightarrow {}^3\text{He} + n$) would produce 2.45 MeV neutrons which can be detected outside of the target chamber. This has now been observed using the FALCON laser.⁹⁹

Figure 6.2 shows time of flight data for the neutrons produced in this reaction at several distances. The neutrons were detected with large area plastic scintillators wrapped in lead. The energy peak indicates the presence of 2.45 MeV neutrons as we would expect from this reaction. The production yield is on the order of 10^4 per shot over 4π sr.

Possible applications of this work include neutron radiography and materials science. It remains to be seen if these results can be scaled up to make this a useful, and relatively inexpensive, neutron source. However, this experiment certainly demonstrates the ability of clusters to produce very high ion temperatures.

6.1.4 X-ray emission

As more and more components are placed on a silicon wafer, there is a need to go to smaller and smaller feature sizes. This requires the use of shorter wavelengths in the lithographic manufacturing process. There is currently a major development effort to create a soft

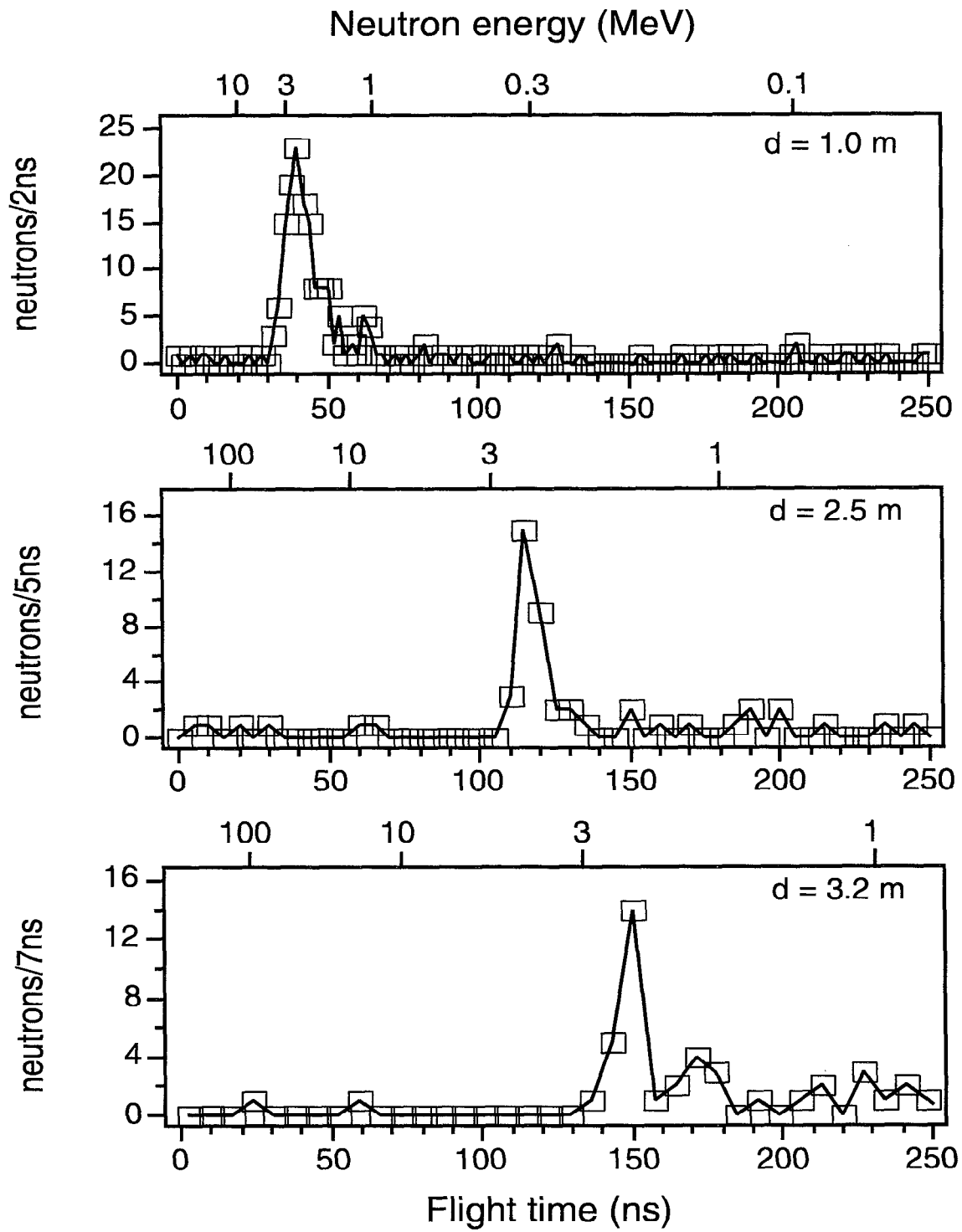


Figure 6.2: TOF data from neutron generation experiments.

x-ray source, near 134 \AA , to be used for the next generation of lithography. Kubiak *et al.*¹⁰⁰ has been working on a xenon cluster source for this purpose. Using a standard nanosecond pulse width laser, they have seen near total absorption and about 1% conversion into useful wavelengths. We have shown that the clusters are disassembled after the first few picoseconds of the pulse, so exactly how the clusters enhance the absorption is not clear. Most likely it has to do with enhanced ionization due to collisional ionization in the early stages of the pulse. Time resolved interferometry could help understand the role clusters play in the interaction. By using a shorter pulse it may be possible to make these sources more efficient and economical, and therefore more commercially viable.

6.2 Conclusions

After several years of research, the physics of laser cluster interactions is being understood. More work is needed before we have a complete picture of what is happening on the femtosecond timescale. The research presented here is a step along that road. Clusters are beginning to find some practical applications, and we can only wait and see if this research will find its way into mainstream use.

Appendix A

Derivation of the Mie Solution

The Mie solution has been presented in many works.^{75–77} This derivation will follow from these.

A.1 Maxwell's equations and the vector wave equation

The problem of solving for the electric and magnetic fields around and inside a sphere comes down to solving Maxwell's equations with the appropriate boundary conditions. Maxwell's equations can be written as

$$\nabla \times \mathbf{H} = \frac{4\pi}{c} \mathbf{J} + \frac{1}{c} \frac{d\mathbf{D}}{dt}, \quad (\text{A.1})$$

$$\nabla \times \mathbf{E} = -\frac{1}{c} \frac{d\mathbf{B}}{dt}, \quad (\text{A.2})$$

$$\nabla \cdot \mathbf{D} = 4\pi\rho, \quad (\text{A.3})$$

$$\nabla \cdot \mathbf{H} = 0. \quad (\text{A.4})$$

We are looking for periodic solutions to these equations of the form

$$A = Ce^{-i\omega t}. \quad (\text{A.5})$$

Using this and

$$\mathbf{J} = \sigma \mathbf{E}, \quad (\text{A.6})$$

$$\mathbf{D} = \epsilon \mathbf{E}, \quad (\text{A.7})$$

$$\mathbf{B} = \mu \mathbf{H}, \quad (\text{A.8})$$

we can simplify Eqs. A.1 and A.2

$$\nabla \times \mathbf{H} = ikm^2 \mathbf{E}, \quad (\text{A.9})$$

$$\nabla \times \mathbf{E} = -ik\mathbf{H}, \quad (\text{A.10})$$

where

$$k = \frac{\omega}{c}, \quad (\text{A.11})$$

$$m^2 = \epsilon + \frac{i4\pi\sigma}{\omega}, \quad (\text{A.12})$$

$$\mu = 1. \quad (\text{A.13})$$

Taking the curl of both sides of Eq. A.10 yields

$$\nabla \times \nabla \times \mathbf{E} = -ik\nabla \times \mathbf{H}. \quad (\text{A.14})$$

Using a vector identity and Eq. A.9 we obtain

$$\nabla(\nabla \cdot \mathbf{E}) - \nabla^2 \mathbf{E} = k^2 m^2 \mathbf{E}. \quad (\text{A.15})$$

The first term is zero from the divergence of Eq. A.9. Hence Eq. A.14 becomes

$$\nabla^2 \mathbf{E} + k^2 m^2 \mathbf{E} = 0, \quad (\text{A.16})$$

This is a vector wave equation. The same treatment will produce a similar result for \mathbf{H} so that both \mathbf{E} and \mathbf{H} will satisfy the vector wave equation of the form

$$\nabla^2 \mathbf{A} + k^2 m^2 \mathbf{A} = 0, \quad (\text{A.17})$$

Using Eqs. A.18, A.19, A.30, and A.31 we can form the solutions to the vector wave equation (A.17), namely the vector spherical harmonics

$$\begin{aligned} \mathbf{M}_{eln} = & \frac{-l}{\sin \theta} \sin l\phi P_n^l(\cos \theta) z_n(mkr) \hat{\theta} \\ & - \cos l\phi \frac{dP_n^l(\cos \theta)}{d\theta} z_n(mkr) \hat{\phi}, \end{aligned} \quad (\text{A.32})$$

$$\begin{aligned} \mathbf{M}_{oln} = & \frac{l}{\sin \theta} \cos l\phi P_n^l(\cos \theta) z_n(mkr) \hat{\theta} \\ & - \sin l\phi \frac{dP_n^l(\cos \theta)}{d\theta} z_n(mkr) \hat{\phi}, \end{aligned} \quad (\text{A.33})$$

$$\begin{aligned} \mathbf{N}_{eln} = & \frac{z_n(mkr)}{mkr} \cos l\phi n(n+1) P_n^l(\cos \theta) \hat{\mathbf{r}} \\ & + \cos l\phi \frac{dP_n^l(\cos \theta)}{d\theta} \frac{1}{mkr} \frac{d}{dr} [r z_n(mkr)] \hat{\theta} \\ & - l \sin l\phi \frac{P_n^l(\cos \theta)}{\sin \theta} \frac{1}{mkr} \frac{d}{dr} [r z_n(mkr)] \hat{\phi}, \end{aligned} \quad (\text{A.34})$$

$$\begin{aligned} \mathbf{N}_{oln} = & \frac{z_n(mkr)}{mkr} \sin l\phi n(n+1) P_n^l(\cos \theta) \hat{\mathbf{r}} \\ & + \sin l\phi \frac{dP_n^l(\cos \theta)}{d\theta} \frac{1}{mkr} \frac{d}{dr} [r z_n(mkr)] \hat{\theta} \\ & - l \cos l\phi \frac{P_n^l(\cos \theta)}{\sin \theta} \frac{1}{mkr} \frac{d}{dr} [r z_n(mkr)] \hat{\phi}. \end{aligned} \quad (\text{A.35})$$

A.2 Expansion of the fields in spherical harmonics

A.2.1 Incident field

The incident field will be a simple plane wave. The origin will be set at the center of the sphere and the z -axis will be the direction of propagation. The incident wave will be polarized with the x -axis being the plane of electric oscillation. This makes the incident field

$$\mathbf{E}_i = \hat{\mathbf{x}} E_0 e^{imkz - i\omega t} = \hat{\mathbf{x}} E_0 e^{imkr \cos \theta - i\omega t} = \hat{\mathbf{x}} E_0 e^{i\rho \cos \theta - i\omega t}, \quad (\text{A.36})$$

where

$$\hat{\mathbf{x}} = \sin \theta \cos \phi \hat{\mathbf{r}} + \cos \theta \cos \phi \hat{\boldsymbol{\theta}} - \sin \phi \hat{\boldsymbol{\phi}}, \quad (\text{A.37})$$

$$\rho = mkr. \quad (\text{A.38})$$

We need to now expand the field in the vector spherical harmonics. We can write the incident field as

$$\mathbf{E}_i = \sum_{l=0}^{\infty} \sum_{n=l}^{\infty} (B_{eln} \mathbf{M}_{eln} + B_{oln} \mathbf{M}_{oln} + A_{eln} \mathbf{N}_{eln} + A_{oln} \mathbf{N}_{oln}). \quad (\text{A.39})$$

We find the unknown coefficients, $A_{eln}, A_{oln}, B_{eln}, B_{oln}$ with the use of the orthogonal properties of the vector spherical harmonics. By taking the dot product of both sides with the individual vector spherical harmonics and integrating, we can solve for the coefficients. All permutations produce 16 different integrals, 10 of which are unique in form.

First we will use the properties of sine and cosine, namely

$$\int_0^{2\pi} \sin l\phi \cos n\phi d\phi = 0 \quad \text{for all integral } l \text{ and } n. \quad (\text{A.40})$$

$$\int_0^{2\pi} \cos l\phi \cos n\phi d\phi = \begin{cases} \pi \delta_{l,n} & l \neq 0, \\ 2\pi & l = n = 0, \end{cases} \quad (\text{A.41})$$

$$\int_0^{2\pi} \sin l\phi \sin n\phi d\phi = \begin{cases} \pi \delta_{l,n} & l \neq 0, \\ 0 & l = 0. \end{cases} \quad (\text{A.42})$$

Using this, it follows from Eqs. A.32 and A.33, that \mathbf{M}_{oln} and $\mathbf{M}_{el'n'}$ are orthogonal

$$\int_0^{2\pi} \int_0^{\pi} \mathbf{M}_{el'n'} \cdot \mathbf{M}_{oln} \sin \theta d\theta d\phi = 0 \quad (\text{for all } l, l', n, n'). \quad (\text{A.43})$$

From further inspection of Eqs. A.32–A.35 and A.40, we find that $(\mathbf{N}_{oln}, \mathbf{N}_{el'n'}), (\mathbf{M}_{oln}, \mathbf{N}_{ol'n'}),$ and $(\mathbf{M}_{eln}, \mathbf{N}_{el'n'})$ are also orthogonal. This eliminates 4 of the integrals.

To show the orthogonality of $(\mathbf{M}_{eln}, \mathbf{N}_{ol'n'})$, and $(\mathbf{N}_{eln}, \mathbf{M}_{ol'n'})$ is slightly more complicated. First we can eliminate all the terms where $l \neq l'$ by Eqs. A.41 and A.42. To deal with the remaining terms we need to evaluate

$$l \int_0^\pi \left(P_n^l \frac{dP_{n'}^l}{d\theta} + P_{n'}^l \frac{dP_n^l}{d\theta} \right) d\theta. \quad (\text{A.44})$$

Note we are leaving off the $(\cos \theta)$ argument of P_n^l for clarity. Recognizing the derivative of a product, we find

$$l \int_0^\pi \frac{d}{d\theta} \left(P_n^l P_{n'}^l \right) d\theta = l P_n^l P_{n'}^l \Big|_0^\pi. \quad (\text{A.45})$$

Which is zero immediately if $l = 0$, and is zero otherwise because $P_n^l = 0$ for $\theta = 0, \pi$ by Eq. A.27.

This leaves us with the four integrals containing the dot product of each vector spherical harmonic with itself. If we can show that these are zero when $l \neq l'$ or $n \neq n'$, the remaining terms can be used to calculate the unknown coefficients.

For $l \neq 0$ the sine and cosine relations again eliminate all $l \neq l'$ terms. For the $n \neq n'$ terms we need to show

$$\int_0^\pi \left(\frac{dP_n^l}{d\theta} \frac{dP_{n'}^l}{d\theta} + l^2 \frac{P_n^l P_{n'}^l}{\sin^2 \theta} + P_n^l P_{n'}^l \right) \sin \theta d\theta = 0. \quad (\text{A.46})$$

The last term (which is only from the N integrals) is zero by the orthogonality of the associated Legendre polynomials. We need to rewrite the remaining terms. Since P_n^l is a solution to Eq. A.24 we can write

$$\frac{1}{\sin \theta} \frac{d}{d\theta} \left(\sin \theta \frac{dP_n^l}{d\theta} \right) + \left[n(n+1) - \frac{l^2}{\sin^2 \theta} \right] P_n^l = 0. \quad (\text{A.47})$$

Multiplying by $P_{n'}^l$ and rearranging we get

$$\frac{d}{d\theta} \left(\sin \theta \frac{dP_n^l}{d\theta} \right) P_{n'}^l + \sin \theta n(n+1) P_n^l P_{n'}^l = \sin \theta \frac{l^2}{\sin^2 \theta} P_n^l P_{n'}^l. \quad (\text{A.48})$$

With further manipulation we can put this into the form of Eq. A.46

$$\left(\frac{dP_n^l}{d\theta} \frac{dP_{n'}^l}{d\theta} + l^2 \frac{P_n^l P_{n'}^l}{\sin^2 \theta} \right) \sin \theta = n(n+1) P_n^l P_{n'}^l \sin \theta + \frac{1}{2} \frac{d}{d\theta} \left(\sin \theta \frac{dP_{n'}^l}{d\theta} P_n^l + \sin \theta \frac{dP_n^l}{d\theta} P_{n'}^l \right). \quad (\text{A.49})$$

When this is substituted into Eq. A.46 and the integral is performed the first term on the right side of Eq. A.49 is zero by orthogonality of the associated Legendre function and the second term is zero from the values at the integration limits.

Finally for $l = 0$, \mathbf{N}_{o1n} and \mathbf{M}_{o1n} are zero by definition and the arguments in Eqs. A.46 and A.49 will hold for \mathbf{N}_{e1n} and \mathbf{M}_{e1n} .

What remains can be used to solve for the unknown coefficients, A_{eln} , A_{oln} , B_{eln} , B_{oln} . These will be of the form

$$B_{eln} = \frac{\int_0^{2\pi} \int_0^\pi \mathbf{E}_i \cdot \mathbf{M}_{eln} \sin \theta d\theta d\phi}{\int_0^{2\pi} \int_0^\pi |\mathbf{M}_{eln}|^2 \sin \theta d\theta d\phi}, \quad (\text{A.50})$$

with similar expressions for the other coefficients. Using Eqs. A.37 and A.40 we find that $B_{eln} = A_{oln} = 0$, for all l and n . Looking at Eqs A.41 and A.42, the remaining coefficients will only be non-zero when $l = 1$. Furthermore, in order for the field to be finite at the origin, the appropriate spherical Bessel function to use is $j_n(\rho)$ which will be well behaved at the origin. We will denote the vector spherical harmonics which use $j_n(\rho)$ with the superscript (1). With this we can now write the incident field as

$$\mathbf{E}_i = \sum_{n=1}^{\infty} (B_{o1n} \mathbf{M}_{o1n}^{(1)} + A_{e1n} \mathbf{N}_{e1n}^{(1)}). \quad (\text{A.51})$$

The denominator in Eq. A.50 for the B_{o1n} coefficient can be written as

$$\begin{aligned} & \int_0^{2\pi} \int_0^\pi |\mathbf{M}_{o1n}|^2 \sin \theta d\theta d\phi \\ &= j_n^2(\rho) \int_0^{2\pi} \int_0^\pi \left[\frac{1}{\sin^2 \theta} \cos^2 \phi P_n^1 P_n^1 + \sin^2 \phi \frac{dP_n^1}{d\theta} \frac{dP_n^1}{d\theta} \right] \sin \theta d\theta d\phi. \end{aligned} \quad (\text{A.52})$$

Performing the integral over ϕ and substituting in Eq. A.49 we obtain

$$j_n^2(\rho)\pi \int_0^\pi \left[n(n+1)P_n^1 P_n^1 \sin \theta + \frac{d}{d\theta} \left(\sin \theta \frac{dP_n^1}{d\theta} P_n^1 \right) \right] d\theta. \quad (\text{A.53})$$

The second half of this integral will zero by virtue of the values at the integration limits.

The first half is just the normalization integral for the associated Legendre polynomials

$$\int_0^\pi P_n^1 P_n^1 \sin \theta d\theta = \frac{2n(n+1)}{2n+1}. \quad (\text{A.54})$$

Therefore, the denominator becomes

$$\int_0^{2\pi} \int_0^\pi |\mathbf{M}_{o1n}|^2 \sin \theta d\theta d\phi = \frac{2\pi j_n^2(\rho)[n(n+1)]^2}{2n+1}. \quad (\text{A.55})$$

The numerator in Eq. A.50 for this coefficient is

$$\begin{aligned} & \int_0^{2\pi} \int_0^\pi \mathbf{E}_i \cdot \mathbf{M}_{o1n} \sin \theta d\theta d\phi \\ &= j_n(\rho) E_0 e^{-i\omega t} \int_0^{2\pi} \int_0^\pi \left[\frac{\cos \theta}{\sin \theta} \cos^2 \phi P_n^1 + \sin^2 \phi \frac{dP_n^1}{d\theta} \right] e^{i\rho \cos \theta} \sin \theta d\theta d\phi. \end{aligned} \quad (\text{A.56})$$

Again, the integral over ϕ is easily performed and the remaining term is the derivative of a product. Hence, Eq. A.56 becomes

$$\pi j_n(\rho) E_0 e^{-i\omega t} \int_0^\pi \frac{d}{d\theta} (\sin \theta P_n^1) e^{i\rho \cos \theta} d\theta. \quad (\text{A.57})$$

Using Eq. A.27 it is easily shown that

$$P_n^1 = -\frac{dP_n}{d\theta}, \quad (\text{A.58})$$

where P_n are the Legendre polynomials which satisfy Eq. A.24 for $l = 0$

$$\frac{d}{d\theta} \left(\sin \theta \frac{dP_n}{d\theta} \right) = -n(n+1)P_n \sin \theta. \quad (\text{A.59})$$

With Eqs. A.58 and A.59 we can rewrite Eq. A.57 as

$$E_0 e^{-i\omega t} \pi j_n(\rho) n(n+1) \int_0^\pi P_n \sin \theta e^{i\rho \cos \theta} d\theta. \quad (\text{A.60})$$

We immediately recognize this as being similar to an integral representation of j_n ¹⁰¹

$$j_n(\rho) = \frac{i^{-n}}{2} \int_0^\pi P_n \sin \theta e^{i\rho \cos \theta} d\theta. \quad (\text{A.61})$$

Hence Eq. A.56 becomes

$$\int_0^{2\pi} \int_0^\pi \mathbf{E}_i \cdot \mathbf{M}_{o1n} \sin \theta d\theta d\phi = 2\pi j_n^2(\rho) e^{-i\omega t} E_0 n(n+1) i^n. \quad (\text{A.62})$$

Bringing this together with Eq. A.55 we find

$$B_{o1n} = i^n e^{-i\omega t} E_0 \frac{2n+1}{n(n+1)}. \quad (\text{A.63})$$

Calculating A_{e1n} is going to be more complicated. The denominator can be written

$$\begin{aligned} & \int_0^{2\pi} \int_0^\pi |\mathbf{N}_{e1n}|^2 \sin \theta d\theta d\phi \\ &= \int_0^{2\pi} \int_0^\pi \left[\frac{j_n^2(\rho)}{\rho^2} \cos^2 \phi [n(n+1)]^2 P_n^1 P_n^1 + \cos^2 \phi \frac{dP_n^1}{d\theta} \frac{dP_n^1}{d\theta} \frac{1}{\rho^2} \left(\frac{d}{d\rho} [\rho j_n(\rho)] \right)^2 \right. \\ & \quad \left. + \sin^2 \phi \frac{P_n^1 P_n^1}{\sin^2 \theta} \frac{1}{\rho^2} \left(\frac{d}{d\rho} [\rho j_n(\rho)] \right)^2 \right] \sin \theta d\theta d\phi. \end{aligned} \quad (\text{A.64})$$

Performing the ϕ integral and collecting terms we obtain

$$\frac{\pi}{\rho^2} \int_0^\pi \left[j_n^2(\rho) [n(n+1)]^2 P_n^1 P_n^1 + \left(\frac{dP_n^1}{d\theta} \frac{dP_n^1}{d\theta} + \frac{P_n^1 P_n^1}{\sin^2 \theta} \right) \left(\frac{d}{d\rho} [\rho j_n(\rho)] \right)^2 \right] \sin \theta d\theta. \quad (\text{A.65})$$

Substituting in Eq. A.49 and using Eqs. A.27 and A.54 to evaluate the integral we find

$$\int_0^{2\pi} \int_0^\pi |\mathbf{N}_{e1n}|^2 \sin \theta d\theta d\phi = \frac{2\pi [n(n+1)]^2}{(2n+1)\rho^2} \left[j_n^2(\rho) n(n+1) + \left(\frac{d}{d\rho} [\rho j_n(\rho)] \right)^2 \right]. \quad (\text{A.66})$$

The numerator for the A_{e1n} coefficient is

$$\begin{aligned} & \int_0^{2\pi} \int_0^\pi \mathbf{E}_i \cdot \mathbf{N}_{e1n} \sin \theta d\theta d\phi = E_0 e^{-i\omega t} \int_0^{2\pi} \int_0^\pi \left[\frac{j_n(\rho)}{\rho} \cos^2 \phi n(n+1) P_n^1 \sin \theta \right. \\ & \quad \left. + \cos^2 \phi \frac{dP_n^1}{d\theta} \cos \theta \frac{1}{\rho} \frac{d}{d\rho} [\rho j_n(\rho)] + \sin^2 \phi \frac{P_n^1}{\sin \theta} \frac{1}{\rho} \frac{d}{d\rho} [\rho j_n(\rho)] \right] e^{i\rho \cos \theta} d\theta d\phi. \end{aligned} \quad (\text{A.67})$$

The integral over ϕ is trivial and after some manipulation we obtain

$$\frac{\pi E_0 e^{-i\omega t}}{\rho} \int_0^\pi \left[j_n(\rho) n(n+1) P_n^1 \sin^2 \theta + \left(\frac{dP_n^1}{d\theta} \cos \theta \sin \theta + P_n^1 \right) \frac{d}{d\rho} [\rho j_n(\rho)] \right] e^{i\rho \cos \theta} d\theta. \quad (\text{A.68})$$

The first term can be integrated by parts

$$\begin{aligned} \int_0^\pi [j_n(\rho) n(n+1) P_n^1 \sin^2 \theta] e^{i\rho \cos \theta} d\theta \\ = \frac{j_n(\rho)}{i\rho} P_n^1 e^{i\rho \cos \theta} \Big|_0^\pi + \frac{j_n(\rho)}{i\rho} \int_0^\pi e^{i\rho \cos \theta} \frac{d}{d\theta} (P_n^1 \sin \theta) d\theta. \end{aligned} \quad (\text{A.69})$$

The first term here is zero by Eq. A.27. The remaining term is basically the same as Eq. A.57. Hence we find that

$$\int_0^\pi [j_n(\rho) n(n+1) P_n^1 \sin^2 \theta] e^{i\rho \cos \theta} d\theta = \frac{2j_n^2(\rho)}{i\rho} [n(n+1)]^2 i^n. \quad (\text{A.70})$$

We are going to have to do some work to evaluate the second term in Eq. A.68. Taking Eq. A.61, multiplying both sides by ρ , and differentiating with respect to ρ we obtain

$$\frac{d}{d\rho} [\rho j_n(\rho)] = j_n + \frac{i^{-n}}{2} i\rho \int_0^\pi \cos \theta e^{i\rho \cos \theta} \sin \theta P_n d\theta \quad (\text{A.71})$$

Substituting in from Eq. A.59 for $\sin \theta P_n$, using Eq. A.58, and expanding the derivative gives us

$$\frac{d}{d\rho} [\rho j_n(\rho)] = j_n + \frac{i^{-n}}{2n(n+1)} i\rho \int_0^\pi \left(\cos^2 \theta P_n^1 + \cos \theta \sin \theta \frac{dP_n^1}{d\theta} \right) e^{i\rho \cos \theta} d\theta. \quad (\text{A.72})$$

Using

$$\sin^2 \theta + \cos^2 \theta = 1, \quad (\text{A.73})$$

we can rewrite Eq. A.72 as

$$\frac{d}{d\rho} [\rho j_n(\rho)] = j_n + \frac{i^{-n}}{2n(n+1)} i\rho \int_0^\pi \left[-\sin^2 \theta P_n^1 + \left(P_n^1 + \cos \theta \sin \theta \frac{dP_n^1}{d\theta} \right) \right] e^{i\rho \cos \theta} d\theta. \quad (\text{A.74})$$

Using Eq. A.70 we find that the first term in the integral equals j_n and cancels. Rearranging terms, we find what we have been looking for, namely an expression for the second term of Eq. A.68

$$\int_0^\pi \left(P_n^1 + \cos \theta \sin \theta \frac{dP_n^1}{d\theta} \right) e^{i\rho \cos \theta} d\theta = \frac{2n(n+1)i^n}{i\rho} \frac{d}{d\rho} [\rho j_n(\rho)]. \quad (\text{A.75})$$

We can now write the numerator of the A_{e1n} coefficient as

$$\int_0^{2\pi} \int_0^\pi \mathbf{E}_i \cdot \mathbf{N}_{e1n} \sin \theta d\theta d\phi = \frac{2\pi E_0 e^{-i\omega t} n(n+1)i^n}{i\rho^2} \left[j_n^2(\rho) n(n+1) + \left(\frac{d}{d\rho} [\rho j_n(\rho)] \right)^2 \right]. \quad (\text{A.76})$$

Taking this with Eq. A.66 we find

$$A_{e1n} = -iE_0 e^{-i\omega t} i^n \frac{2n+1}{n(n+1)}. \quad (\text{A.77})$$

Finally, we use Eqs. A.63 and A.77 in Eq. A.51 and obtain the desired result

$$\mathbf{E}_i = E_0 e^{-i\omega t} \sum_{n=1}^{\infty} i^n \frac{2n+1}{n(n+1)} (\mathbf{M}_{o1n}^{(1)} - i\mathbf{N}_{e1n}^{(1)}). \quad (\text{A.78})$$

The incident magnetic field can be easily written by using Eqs. A.10, A.19, and A.21

$$\mathbf{H}_i = -mE_0 e^{-i\omega t} \sum_{n=1}^{\infty} i^n \frac{2n+1}{n(n+1)} (\mathbf{M}_{e1n}^{(1)} + i\mathbf{N}_{o1n}^{(1)}). \quad (\text{A.79})$$

A.2.2 Internal and scattered fields

When the plane wave described in the previous section is incident on a sphere of radius a there will be two additional fields we must deal with, the internal field, \mathbf{E}_l , and the scattered field, \mathbf{E}_s . The total external field will be the sum of the scattered and incident fields. We need to use the condition that the tangential components of both \mathbf{E} and \mathbf{H} will be the same inside and outside the sphere at the boundary

$$(\mathbf{E}_i + \mathbf{E}_s - \mathbf{E}_l) \times \hat{\mathbf{r}} = (\mathbf{H}_i + \mathbf{H}_s - \mathbf{H}_l) \times \hat{\mathbf{r}} = 0, \quad r = a. \quad (\text{A.80})$$

The internal field must be finite at the origin. Hence we will use $j_n(\rho)$ for the spherical Bessel function in the vector spherical harmonics. Using the boundary condition, the form of the incident field and the general orthogonality of the vector spherical harmonics, the internal field must take on the form of

$$\mathbf{E}_l = E_0 e^{-i\omega t} \sum_{n=1}^{\infty} i^n \frac{2n+1}{n(n+1)} (c_n \mathbf{M}_{o1n}^{(1)} - i d_n \mathbf{N}_{e1n}^{(1)}). \quad (\text{A.81})$$

$$\mathbf{H}_l = -m_i E_0 e^{-i\omega t} \sum_{n=1}^{\infty} i^n \frac{2n+1}{n(n+1)} (d_n \mathbf{M}_{e1n}^{(1)} + i c_n \mathbf{N}_{o1n}^{(1)}). \quad (\text{A.82})$$

where c_n and d_n are constants to be determined and m_i is the internal index of refraction.

The scattered field has no condition at the origin which has to be satisfied, and therefore we cannot eliminate the spherical Bessel function of the second kind. However, as we get very far away from the sphere, the scattered field should become an outgoing spherical wave. We recall that the asymptotic limit of the spherical Hankel function of the first kind ($h_n^{(1)}(\rho) = j_n(\rho) + i y_n(\rho)$) is

$$h_n^{(1)}(\rho) \sim \frac{(-i)^{n+1}}{\rho} e^{i\rho}. \quad (\text{A.83})$$

This is the outgoing spherical wave we want.

The asymptotic limit of the derivative of the spherical Hankel function of the first kind will have a similar form

$$\frac{dh_n^{(1)}(\rho)}{d\rho} \sim \frac{(-i)^n}{\rho} e^{i\rho}. \quad (\text{A.84})$$

Hence we want to use these functions for the radial dependence in the vector spherical harmonics. We will denote the vector spherical harmonics which use the spherical Hankel

functions of the first kind with the superscript (3). The scattered fields can be written as

$$\mathbf{E}_s = E_0 \sum_{n=1}^{\infty} i^n \frac{2n+1}{n(n+1)} (ia_n \mathbf{N}_{e1n}^{(3)} - b_n \mathbf{M}_{o1n}^{(3)}). \quad (\text{A.85})$$

$$\mathbf{H}_s = mE_0 \sum_{n=1}^{\infty} i^n \frac{2n+1}{n(n+1)} (ib_n \mathbf{N}_{o1n}^{(3)} + a_n \mathbf{M}_{e1n}^{(3)}). \quad (\text{A.86})$$

Where a_n and b_n are another set of constants.

A.3 Determination of coefficients

We are first going to simplify the vector spherical harmonics by introducing the functions

$$\pi_n(\cos \theta) = \frac{1}{\sin \theta} P_n^1(\cos \theta), \quad (\text{A.87})$$

$$\tau_n(\cos \theta) = \frac{d}{d\theta} P_n^1(\cos \theta), \quad (\text{A.88})$$

Using these we can rewrite Eqs. A.32–A.35 (for the relevant $l = 1$ case) as

$$\mathbf{M}_{o1n} = \cos \phi \pi_n(\cos \theta) z_n(\rho) \hat{\theta} - \sin \phi \tau_n(\cos \theta) z_n(\rho) \hat{\phi} \quad (\text{A.89})$$

$$\mathbf{M}_{e1n} = -\sin \phi \pi_n(\cos \theta) z_n(\rho) \hat{\theta} - \cos \phi \tau_n(\cos \theta) z_n(\rho) \hat{\phi} \quad (\text{A.90})$$

$$\begin{aligned} \mathbf{N}_{o1n} = & \sin \phi n(n+1) \sin \theta \pi_n(\cos \theta) \frac{z_n(\rho)}{\rho} \hat{\mathbf{r}} \\ & + \sin \phi \tau_n(\cos \theta) \frac{[\rho z_n(\rho)]'}{\rho} \hat{\theta} + \cos \phi \pi_n(\cos \theta) \frac{[\rho z_n(\rho)]'}{\rho} \hat{\phi} \end{aligned} \quad (\text{A.91})$$

$$\begin{aligned} \mathbf{N}_{e1n} = & \cos \phi n(n+1) \sin \theta \pi_n(\cos \theta) \frac{z_n(\rho)}{\rho} \hat{\mathbf{r}} \\ & + \cos \phi \tau_n(\cos \theta) \frac{[\rho z_n(\rho)]'}{\rho} \hat{\theta} - \sin \phi \pi_n(\cos \theta) \frac{[\rho z_n(\rho)]'}{\rho} \hat{\phi} \end{aligned} \quad (\text{A.92})$$

$$(\text{A.93})$$

where the prime denotes derivative.

The boundary conditions (Eq. A.80) at $r = a$ can be written as

$$\begin{aligned} E_{i\theta} + E_{s\theta} &= E_{l\theta} & E_{i\phi} + E_{s\phi} &= E_{l\phi} \\ H_{i\theta} + H_{s\theta} &= H_{l\theta} & H_{i\phi} + H_{s\phi} &= H_{l\phi} \end{aligned} \quad (\text{A.94})$$

To find the coefficients for the internal and scattered fields we plug in the expression we found for the fields into the boundary conditions and solve for the unknown constants. The sphere will be sitting in a vacuum so the external index of refraction will be unity. We will set the internal index of refraction to m . It turns out that the ϕ components give redundant information, so we only need to look at the θ terms. Using Eqs. A.78, A.79, A.81, A.82, A.85, A.86, A.89–A.91, and A.94 we find

$$\begin{aligned} i \sin \phi \pi_n(\cos \theta) \frac{[\rho j_n(\rho)]'}{\rho} - \sin \phi \tau_n(\cos \theta) j_n(\rho) \\ - i a_n \sin \phi \pi_n(\cos \theta) \frac{[\rho h_n^{(1)}(\rho)]'}{\rho} + b_n \sin \phi \tau_n(\cos \theta) h_n^{(1)}(\rho) \\ = c_n \sin \phi \tau_n(\cos \theta) j_n(\rho) - i d_n \sin \phi \pi_n(\cos \theta) \frac{[\rho j_n(\rho)]'}{\rho} \end{aligned} \quad (\text{A.95})$$

$$\begin{aligned} \cos \phi \tau_n(\cos \theta) j_n(\rho) - i \cos \phi \pi_n(\cos \theta) \frac{[\rho j_n(\rho)]'}{\rho} \\ - a_n \sin \phi \tau_n(\cos \theta) h_n^{(1)}(\rho) + b_n \cos \phi \pi_n(\cos \theta) \frac{[\rho h_n^{(1)}(\rho)]'}{\rho} \\ = i m c_n \cos \phi \pi_n(\cos \theta) \frac{[\rho j_n(\rho)]'}{\rho} - m d_n \cos \phi \tau_n(\cos \theta) j_n(\rho) \end{aligned} \quad (\text{A.96})$$

Collecting the real and imaginary terms, introducing the Riccati-Bessel functions

$$\psi_n(\rho) = \rho j_n(\rho), \quad (\text{A.97})$$

$$\xi_n(\rho) = \rho h_n^{(1)}(\rho). \quad (\text{A.98})$$

and using the arguments

$$x = ka = \frac{2\pi a}{\lambda}, \quad y = mka. \quad (\text{A.99})$$

we obtain four linear equations

$$\psi_n(y)c_n + \xi_n(x)b_n = \psi_n(x), \quad (\text{A.100})$$

$$m\psi'_n c_n + \xi'_n(x)b_n = \psi'_n(x), \quad (\text{A.101})$$

$$m\psi_n(y)d_n + \xi_n(x)a_n = \psi_n(x), \quad (\text{A.102})$$

$$\psi'_n d_n + \xi'_n(x)a_n = \psi'_n(x). \quad (\text{A.103})$$

These are easily solved to yield the needed coefficients

$$a_n = \frac{m\psi_n(y)\psi'_n(x) - \psi_n(x)\psi'_n(y)}{m\psi_n(y)\xi'_n(x) - \xi_n(x)\psi'_n(y)} \quad (\text{A.104})$$

$$b_n = \frac{\psi_n(y)\psi'_n(x) - m\psi_n(x)\psi'_n(y)}{\psi_n(y)\xi'_n(x) - m\xi_n(x)\psi'_n(y)} \quad (\text{A.105})$$

$$c_n = \frac{\psi_n(x)\xi'_n(x) - \xi_n(x)\psi'_n(x)}{\psi_n(y)\xi'_n(x) - m\xi_n(x)\psi'_n(y)} \quad (\text{A.106})$$

$$d_n = \frac{\psi_n(x)\xi'_n(x) - \xi_n(x)\psi'_n(x)}{m\psi_n(y)\xi'_n(x) - \xi_n(x)\psi'_n(y)} \quad (\text{A.107})$$

We now know the field at every point both inside and outside the sphere.

A.4 Amplitude functions and cross-sections

Our interest is in finding the absorption of the incident radiation. This is generally done by looking at the scattered energy and the extinction from the incident beam. The difference will be the absorption. We can look at the scattered wave at a distance far from the sphere. The spherical Hankel functions can be replaced with their asymptotic expressions (Eqs. A.83 and A.84). The scattered field components in the far field can be written as

$$E_\theta = H_\phi = \frac{iE_0}{kr} e^{i(kr - \omega t)} \cos \phi S_2(\theta), \quad (\text{A.108})$$

$$E_\phi = -H_\theta = \frac{-iE_0}{kr} e^{i(kr - \omega t)} \sin \phi S_1(\theta), \quad (\text{A.109})$$

where

$$S_1(\theta) = \sum_{n=1}^{\infty} \frac{2n+1}{n(n+1)} \{a_n \pi_n(\cos \theta) + b_n \tau_n(\cos \theta)\}, \quad (\text{A.110})$$

$$S_2(\theta) = \sum_{n=1}^{\infty} \frac{2n+1}{n(n+1)} \{b_n \pi_n(\cos \theta) + a_n \tau_n(\cos \theta)\}. \quad (\text{A.111})$$

The radial components of the fields tend to zero faster than $1/r$ so they do not significantly contribute to the far field. S_1 and S_2 are called the amplitude functions. These functions contain the angular dependence of the fields.

We can now calculate the cross-sections for extinction and scattering. This can be done integrating the Poynting vector. For a time harmonic field we can write

$$\mathbf{S} = \frac{c}{8\pi} \text{Re}(\mathbf{E} \times \mathbf{H}^*). \quad (\text{A.112})$$

Integrating this over a sphere ($r > a$) will give the net energy flow across the boundary. We want to use the total field outside of the sphere (incident and scattered). From this and conservation of energy, we find

$$W_{ext} = \text{Re} \frac{c}{8\pi} \int_0^\pi \int_0^{2\pi} (E_{i\phi} H_{s\theta}^* - E_{i\theta} H_{s\phi}^* - E_{s\theta} H_{i\phi}^* + E_{s\phi} H_{i\theta}^*) r^2 \sin \theta d\theta d\phi. \quad (\text{A.113})$$

The total scattering can be calculated by only looking at the scattered field

$$W_{sca} = \text{Re} \frac{c}{8\pi} \int_0^\pi \int_0^{2\pi} (E_{s\theta} H_{s\phi}^* - E_{s\phi} H_{s\theta}^*) r^2 \sin \theta d\theta d\phi. \quad (\text{A.114})$$

Using Eqs. A.78, A.79, A.87, A.88, A.89, A.92, A.108–A.111, and

$$\int_0^\pi (\pi_n \pi_m + \tau_n \tau_m) \sin \theta d\theta = \delta_n^m \frac{2n^2(n+1)^2}{2n+1} \quad (\text{A.115})$$

these integrals can be easily evaluated. Dividing by the incident intensity

$$I_i = \frac{c}{8\pi} |E_0|^2 \quad (\text{A.116})$$

we obtain the cross-sections

$$\sigma_{ext} = \frac{W_{ext}}{I_i} \frac{2\pi}{k^2} \sum_{n=1}^{\infty} (2n+1) \text{Re}(a_n + b_n), \quad (\text{A.117})$$

and

$$\sigma_{sca} = \frac{W_{sca}}{I_i} = \frac{2\pi}{k^2} \sum_{n=1}^{\infty} (2n+1) \{|a_n|^2 + |b_n|^2\}. \quad (\text{A.118})$$

From conservation of energy we have

$$\sigma_{abs} = \sigma_{ext} - \sigma_{sca} \quad (\text{A.119})$$

A.5 Conclusion

Using Eq. A.119 we can calculate the absorbed energy for a sphere of any size with a complex dielectric constant. This will enable us to perform cluster calculations on a long time scale in which the small clusters expand to a size on the order of the wavelength of light.

Bibliography

1. T. H. Maiman, "Stimulated optical radiation in ruby," *Nature (London)* **187**, 493–494 (1960).
2. J. R.G. Meyerand and A.F.Haught, "Gas Breakdown at Optical Frequencies," *Phys. Rev. Lett.* **11**, 401–403 (1963).
3. L. Keldysh, "Ionization in the field of a strong electromagnetic wave," *Sov. Phys. JETP* **20**, 1307–1314 (1965).
4. H. B. Bebb and A. Gold, "Multiphoton Ionization of Hydrogen and Rare-Gas Atoms," *Phys. Rev.* **143**, 1–22 (1966).
5. S. Augst, D. Meyerhofer, D. Strickland, and S. Chin, "Laser ionization of noble gases by Coulomb-barrier suppression," *J. Opt. Soc. Am. B* **8**, 858–867 (1991).
6. M. Perry, O. Landen, A. Szöke, and E. Campbell, "Multiphoton ionization of the noble gases by an intense 10^{14} -W/cm² dye laser," *Phys. Rev. A* **37**, 747–760 (1988).
7. E. Mevel, P. Breger, R. Trainham, G. Petite, and P. Agostini, "Atoms in Strong Optical Fields: Evolution from Multiphoton to Tunnel Ionization," *Phys. Rev. Lett.* **70**, 406–409 (1993).
8. D. Strickland and G. Mourou, "Compression of amplified chirped optical pulses," *Opt. Commun.* **56**, 219–221 (1985).
9. M. D. Perry and G. Mourou, "Terawatt to petawatt subpicosecond lasers," *Science* **264**, 917–924 (1994).
10. M. Murnane, H. Kapteyn, S. Gordon, J. Bokor, E. Glytsis, and R. Falcone, "Efficient coupling of high-intensity subpicosecond laser pulses into solids," *Appl. Phys. Lett.* **62**, 1068–1070 (1993).
11. J. Kmetec, I. C.L. Gordon, J. Macklin, B. Lemoff, G. Brown, and S. Harris, "MeV X-Ray Generation with a Femtosecond Laser," *Phys. Rev. Lett.* **68**, 1527–1530 (1992).
12. J. A.W. Castleman and R. Keesee, "Gas-Phase Clusters: Spanning the States of Matter," *Science* **241**, 36–42 (1988).
13. O. Hagena and W. Obert, "Cluster Formation in Expanding Supersonic Jets: Effect of Pressure, Temperature, Nozzle Size, and Test Gas," *J. Chem. Phys.* **56**, 1793–1802 (1972).

14. J. Stapelfeldt, J. Wörmer, and T. Möller, "Evolution of Electronic Energy Levels in Krypton Clusters from the Atom to the Solid," *Phys. Rev. Lett.* **62**, 98–101 (1988).
15. G. Gibson, R. Rosman, T. Luk, I. McIntyre, A. McPherson, G. Wendin, K. Boyer, and C. Rhodes, "Characteristics of a Non-Equilibrium Picosecond Laser Plasma," In *Short Wavelength Coherent Radiation: Generation and Applications*, R. Falcone, ed., **2**, 246–250 (Optical Society of America, 1988).
16. A. McPherson, T. Luk, B. Thompson, K. Boyer, and C. Rhodes, "Multiphoton-Induced X-Ray Emission and Amplification from Clusters," *Appl. Phys.* **B57**, 337–347 (1993).
17. K. Boyer, B. Thompson, A. McPherson, and C. Rhodes, "Evidence for coherent electron motions in multiphotons x-ray production from Kr and Xe clusters," *J. Opt. Soc. Am. B* **27**, 4373–4389 (1994).
18. K. Boyer and C. Rhodes, "Atomic Inner-Shell Excitation Induced by Coherent Motion of Outer-Shell Electrons," *Phys. Rev. Lett.* **54**, 1490–1493 (1985).
19. P. Lambropoulos, "Mechanisms for Multiple Ionization of Atoms by Strong Pulsed Lasers," *Phys. Rev. Lett.* **55**, 2141–2144 (1985).
20. P. Lee, D. Casperson, and G. Schappert, "Search for multiphoton-induced inner-shell excitations," *Phys. Rev. A* **40**, 1363–1366 (1989).
21. C. Rose-Petruck, K. Schafer, K. Wilson, and C. Barty, "Ultrafast electron dynamics and inner-shell ionization in laser driven clusters," *Phys. Rev. A* **55**, 1182–1190 (1997).
22. T. Ditmire, T. Donnelly, A. Rubenchik, R. Falcone, and M. Perry, "Interaction of intense laser pulses with atomic clusters," *Phys. Rev. A* **53**, 3379–3402 (1996).
23. T. Ditmire, R. Smith, J. Tisch, and M. Hutchinson, "High Intensity Laser Absorption by Gases of Atomic Clusters," *Phys. Rev. Lett.* **78**, 3121–3124 (1997).
24. T. Ditmire, E. Springate, J. Tisch, Y. Shao, M. Mason, N. Hay, J. Marangos, and M. Hutchinson, "Explosion of atomic clusters heated by high-intensity femtosecond laser pulses," *Phys. Rev. A* **57**, 369–382 (1998).
25. J. Jackson, *Classical Electrodynamics* (John Wiley & Sons, 1975).
26. Y. Shao, T. Ditmire, J. Tisch, E. Springate, J. Marangos, and M. Hutchinson, "Multi-keV Electron Generation in the Interaction of Intense laser Pulses with Xe Clusters," *Phys. Rev. Lett.* **77**, 3343–3346 (1996).
27. T. Ditmire, J. Tisch, E. Springate, M. Mason, N. Hay, R. Smith, J. Marangos, and M. Hutchinson, "High-energy ions produced in explosions of superheated atomic clusters," *Nature (London)* **386**, 54–56 (1997).
28. P. Banks, Ph.D. thesis, University of California, Davis, 1997.
29. M. T. Asaki, C.-P. Huang, D. Garvey, J. Zhou, H. C. Kapteyn, and M. M. Murnane, "Generation of 11-fs pulses from a self-mode-locked Ti:sapphire laser," *Opt. Lett.* **18**, 977–979 (1993).

30. A. Stingl, M. Lenzner, C. Spielmann, F. Krausz, and R. Szipöcs, "Sub-10-fs mirror-dispersion-controlled Ti:sapphire laser," *Opt. Lett.* **20**, 602–604 (1995).
31. B. C. Stuart, M. D. Perry, J. Miller, G. Tietbohl, S. Herman, J. A. Britten, C. Brown, D. Pennington, V. Yanovsky, and K. Wharton, "125-TW Ti:sapphire/Nd:glass laser system," *Opt. Lett.* **22**, 242–244 (1997).
32. M. D. Perry *et al.*, "Petawatt Laser Final Report," Technical Report No. UCRL-ID-124933, Lawrence Livermore National Laboratory (1996) .
33. P. Moulton, "Spectroscopic and laser characteristics of Ti:Al₂O₃," *J. Opt. Soc. Am. B* **3**, 125–132 (1986).
34. J. Britten, M. Perry, B. Shore, and R. Boyd, "Universal grating design for pulse stretching and compression in the 800-1100-nm range," *Opt. Lett.* **21**, 540–542 (1996).
35. E. B. Treacy, "Optical pulse compression with diffraction gratings," *IEEE J. Quantum Electron.* **QE-5**, 454–458 (1969).
36. R. Fisher and W. Bischel, "Pulse Compression for More Efficient Operation of Solid-State Laser Amplifier Chains II," *IEEE J. Quantum Electron.* **QE-11**, 46–52 (1975).
37. R. Fisher and W. Bischel, "Pulse compression for more efficient operation of solid-state laser amplifier chains," *Appl. Phys. Lett.* **24**, 468–470 (1974).
38. O. Martinez, J. Gordon, and R. Fork, "Negative group-velocity dispersion using refraction," *J. Opt. Soc. Am. A* **1**, 1003–1006 (1984).
39. M. Pessot, P. Maine, and G. Mourou, "1000 times expansion/compression of optical pulses for chirped pulse amplification," *Opt. Commun.* **62**, 419–421 (1987).
40. M. Perry, F. Patterson, and J. Weston, "Spectral shaping in chirped-pulse amplification," *Opt. Lett.* **15**, 381–383 (1990).
41. C. Barty, T. Guo, C. L. Blanc, F. Raksi, C. Rose-Petruck, J. Squier, K. Wilson, V. Yakovlev, and K. Yamakawa, "Generation of 18-fs multiterawatt pulses by regenerative pulse shaping and chirped-pulse amplification," *Opt. Lett.* **21**, 668–670 (1996).
42. S. Fochs, Master's thesis, University of California, Los Angeles, 1995.
43. D. Spence, P. Kean, and W. Sibbett, "60-fsec pulse generation from a self-mode-locked Ti:sapphire laser," *Opt. Lett.* **16**, 42–44 (1991).
44. P. Banks, M. Perry, S. Fochs, V. Yanovsky, B. Stuart, and J. Zweiback, "Novel, all-reflective stretcher for chirped-pulse-amplification of ultrashort pulses," , submitted to *IEEE J. Quantum Electron.* .
45. W. White, F. Patterson, R. Combs, D. Price, and R. Shepherd, "Compensation of higher-order frequency-dependent phase terms in chirped-pulse amplification systems," *Opt. Lett.* **18**, 1343–1345 (1993).
46. B. C. Stuart, S. Herman, and M. D. Perry, "Chirped-pulse amplification in Ti:sapphire beyond 1 μ m," *IEEE J. Quantum Electron.* **31**, 528–538 (1995).

47. J. M. Auerbach and V. P. Karpenko, "Serrated-aperture apodizers for high-energy laser systems," *Appl. Opt.* **33**, 3179–3183 (1994).
48. C. Bibeau, S. A. Payne, and H. T. Powell, "Direct measurements of the terminal laser level lifetime in Neodymium-doped crystals and glasses," *J. Opt. Soc. Am. B* **12**, 1981–1992 (1995).
49. W. Koechner, *Solid-State Laser Engineering* (Springer, 1996).
50. C. Dane, personal communication (unpublished).
51. L. M. Frantz and J. S. Nodvik, "Theory of Pulse Propagation in a Laser Amplifier," *J. Appl. Phys.* **34**, 2346–2349 (1963).
52. A. E. Siegman, *Lasers* (University Science Books, Mill Valley, CA, 1986).
53. B. C. Stuart, M. D. Feit, S. Herman, A. M. Rubenchik, B. W. Shore, and M. D. Perry, "Nanosecond-to-femtosecond laser-induced breakdown in dielectrics," *Phys. Rev. B* **53**, 1749–1761 (1996).
54. W. Sooy and M. Stitch, "Energy Density Distribution in a Polished Cylinder of Laser Material," *J. Appl. Phys.* **34**, 1719–1723 (1963).
55. M. Ammosov, N. Delone, and V. Krařnov, "Tunnel ionization of complex atoms and of atomic ions in an alternating electromagnetic field," *Sov. Phys. JETP* **64**, 1191–1194 (1986).
56. W. Lotz, "An Empirical Formula for the Electron-Impact Ionization Cross-Section," *Z. Physik* **206**, 205–211 (1967).
57. W. Lotz, "Electron-Impact Ionization Cross-Sections and Ionization Rate Coefficients for Atoms and Ions from Hydrogen to Calcium," *Z. Physik* **216**, 241–247 (1968).
58. J. Eberly and J. Javanainen, "Above-threshold ionisation," *Eur. J. Phys.* **9**, 265–275 (1988).
59. P. Agostini, F. Fabre, G. Mainfray, G. Petite, and N. Rahman, "Free-Free Transitions Following Six-Photon Ionization of Xenon Atoms," *Phys. Rev. Lett.* **42**, 1127–1130 (1979).
60. N. Burnett and P. Corkum, "Cold-plasma production for recombination extreme-ultraviolet lasers by optical-field-induced ionization," *J. Opt. Soc. Am. B* **6**, 1195–1199 (1989).
61. V. Silin, "Nonlinear High-Frequency Plasma Conductivity," *Sov. Phys. JETP* **20**, 1510–1516 (1965).
62. L. Landau and E. Lifshitz, *Electrodynamics of Continuous Media* (Pergaman, 1984).
63. N. Deniov, "On a Singularity of the Field of an Electromagnetic Wave Propagated in an Inhomogeneous Plasma," *Sov. Phys. JETP* **4**, 544–553 (1957).
64. W. Kruer, *The Physics of Laser Plasma Interactions* (Addison-Wesley, 1988).

65. S. Wilks and W. Kruer, "Absorption of Ultrafast, Ultra-Intense Laser Light by Solids and Overdense Plasmas," *IEEE J. Quantum Electron.* **33**, 1954–1968 (1997).
66. L. Page and N. Adams, *Principles of Electricity, an intermediate text in electricity and magnetism* (D Van Nostrand Company, Inc., 1958).
67. G. Mie, "Considerations on the optics of turbid media, especially colloidal metal sols," *Ann. Physik.* **25**, 377–442 (1908).
68. N. Logan, "Survey of Some Early Studies of the Scattering of Plane Waves by a Sphere," *Proc. IEEE* **53**, 773–785 (1965).
69. A. Clebsch, "Ueber die Reflexion an einer Kugelfläche," *J. für Math.* **61**, 195–262 (1863).
70. V. Twersky, "Rayleigh Scattering," *Appl. Opt.* **3**, 1150–1162 (1964).
71. L. Rayleigh, "On the electromagnetic theory of light," *Phil. Mag.* **12**, 81–101 (1881).
72. L. Lorenz, "Sur la lumière réfléchiée et réfractée par une sphère transparente," *Vidensk. Selsk. Skrifter* **6**, 1–62 (1890).
73. G. Walker, "The scattering of electromagnetic waves by a sphere," *Quart. J. Math.* **31**, 36–49 (1900).
74. A. Love, "Scattering of electric waves by a sphere," *Proc. Math. Soc. (London)* **30**, 308–321 (1899).
75. M. Kerker, *The Scattering of Light and other electromagnetic radiation* (Academic Press, 1969).
76. H. van de Hulst, *Light Scattering by Small Particles* (Dover Publications, Inc., 1981).
77. C. Bohren and D. Huffman, *Absorption and Scattering of Light by Small Particles* (John Wiley & Sons, Inc., 1983).
78. A. Haught and D. Polk, "Formation and Heating of Laser Irradiated Solid Particle Plasma," *Phys. Fluids* **13**, 2825–2841 (1970).
79. J. L. Spitzer, *Physics of Fully Ionized Gases* (Interscience Publishers, Inc., 1956).
80. W. Wiscombe, "Improved Mie scattering algorithms," *Appl. Opt.* **19**, 1505–1509 (1980).
81. S. Chapra and R. Canale, *Numerical Methods for Engineers* (McGraw-Hill, 1988).
82. J. Purnell, E. Snyder, S. Wei, and A. C. Jr., "Ultrafast laser-induced Coulomb explosion of clusters with high charge states," *Chem. Phys. Lett.* **229**, 333–339 (1994).
83. M. Perry, C. Darrow, C. Coverdale, and J. Crane, "Measurement of the local electron density by means of stimulated Raman scattering in a laser-produced gas jet plasma," *Opt. Lett.* **17**, 523–525 (1992).
84. O. Abraham, S. Kim, and G. Stein, "Homogeneous nucleation of sulfur hexafluoride clusters in Laval nozzle molecular beams," *J. Chem. Phys.* **75**, 402–411 (1981).

85. J. Wörmer, V. Guzielski, J. Stapelfeldt, and T. Möller, "Fluorescence excitation spectroscopy of xenon clusters in the VUV," *Chem. Phys. Lett.* **159**, 321–326 (1989).
86. O. Hagen, in *Rarefied Gas Dynamics*, L. Trilling and H. Wachman, eds., (Academic, 1969), Vol. 2, pp. 1465–1468.
87. J. Farges, M. Feraudy, B. Raoult, and G. Torchet, "Noncrystalline structure of argon clusters. II. Multilayer icosahedral structure of Ar_N cluster $50 < N < 750$," *J. Chem. Phys.* **84**, 3491–3501 (1986).
88. U. Buck and H. Meyer, "Scattering Analysis of Ar-Cluster Beams," *Surface Sci.* **156**, 275–281 (1985).
89. A. Sinnock and B. Smith, "Refractive Indices of the Condensed Inert Gases," *Phys. Rev.* **181**, 1297–1307 (1969).
90. G. Cook, *Argon, Helium and the Rare Gases* (Interscience Publishers, 1961).
91. M. Itou, T. Harada, and T. Kita, "Soft x-ray monochromator with a varied-space plane grating for synchrotron radiation: design and evaluation," *Appl. Opt.* **28**, 146–153 (1989).
92. S. Augst, D. Strickland, D. Meyerhofer, S. Chin, and J. Eberly, "Tunneling Ionization of Noble Gases in a High-Intensity Laser Field," *Phys. Rev. Lett.* **63**, 2212–2215 (1989).
93. W. Schwanda, K. Eidmann, and M. Richardson, "Characterization of a Flat-Field Grazing-Incidence XUV Spectrometer," *J. X-ray Sci. Technol.* **4**, 8–17 (1993).
94. R. Klingelhöfer and H. Moser, "Production of large hydrogen clusters in condensed molecular beams," *J. Appl. Phys.* **43**, 4575–4579 (1972).
95. W. Kruer and K. Estabrook, " $J \times B$ heating by very intense laser light," *Phys. Fluids* **28**, 430–432 (1985).
96. F. Brunel, "Not-So-Resonant, Resonant Absorption," *Phys. Rev. Lett.* **59**, 52–55 (1987).
97. K. Kondo, A. Borisov, C. Jordan, A. McPherson, W. Schroeder, K. Boyer, and C. Rhodes, "Wavelength dependence of multiphoton-induced $\text{Xe}(\text{M})$ and $\text{Xe}(\text{L})$ emissions from Xe clusters," *J. Phys. B* **30**, 2707–2716 (1997).
98. D. Umstadter, S.-Y. Chen, A. Maksimchuk, G. Mourou, and R. Wagner, "Nonlinear Optics in Relativistic Plasmas and Laser Wake Field Acceleration of Electrons," *Science* **273**, 472–475 (1996).
99. T. Ditmire, J. Zweiback, V. Yanovsky, T. Cowan, G. Hays, and K. Wharton, "Nuclear fusion from explosions of femtosecond-laser heated deuterium clusters," *Nature (London)* **398**, 489–492 (1999).
100. G. Kubiak, L. Bernardez, K. Kernz, D. J. O'Connell, R. Gutowski, and A. Todd, "Debris-free EUVL sources based on gas jets," In *OSA TOPS on Extreme Ultraviolet Lithography*, G. Kubiak and D. Kania, eds., **4**, 66–71 (1996).

101. P. Morse and H. Feshbach, *Methods of Theoretical Physics* (McGraw-Hill Book Company, Inc., 1953).